REVIEWS OF MODERN PHYSICS, VOLUME 92, JANUARY–MARCH 2020

Evolution of shell structure in exotic nuclei

Takaharu Otsuka

*Department of Physics and Center for Nuclear Study, University of Tokyo,
Hongo, Bunkyo-ku, Tokyo 113-0033, Japan,
RIKEN Nishina Center, 2-1 Hirosawa, Wako, Saitama 351-0198, Japan,
Instituut voor Kern- en Stralingsfysica, Katholieke Universiteit Leuven,
B-3001 Leuven, Belgium,
National Superconducting Cyclotron Laboratory,
Michigan State University, East Lansing, Michigan 48824, USA,
and Department of Physics and Astronomy, Michigan State University,
East Lansing, Michigan 48824, USA*

Alexandra Gade

*National Superconducting Cyclotron Laboratory, Michigan State University,
East Lansing, Michigan 48824, USA and Department of Physics and Astronomy,
Michigan State University, East Lansing, Michigan 48824, USA*

Olivier Sorlin

*Grand Accélérateur National d'Ions Lourds (GANIL), CEA/DSM-CNRS/IN2P3,
B.P. 55027, F-14076 Caen Cedex 5, France*

Toshio Suzuki

*Department of Physics and Graduate School of Integrated Basic Sciences,
College of Humanities and Sciences, Nihon University,
Sakurajosui, Setagaya-ku, Tokyo 156-8550, Japan
and National Astronomical Observatory of Japan, Mitaka, Tokyo 181-8588, Japan*

Yutaka Utsuno

*Advanced Science Research Center, Japan Atomic Energy Agency,
Tokai, Ibaraki 319-1195, Japan
and Center for Nuclear Study, University of Tokyo,
Hongo, Bunkyo-ku, Tokyo 113-0033, Japan*

(published 27 March 2020)

The atomic nucleus is a quantum many-body system whose constituent nucleons (protons and neutrons) are subject to complex nucleon-nucleon interactions that include spin- and isospin-dependent components. For stable nuclei, several decades ago, emerging seemingly regular patterns in some observables could already be described successfully within a shell-model picture that results in particularly stable nuclei at certain magic fillings of the shells with protons and/or neutrons: N, $Z = 8$, 20, 28, 50, 82, 126. However, in short-lived, so-called exotic nuclei or rare isotopes, characterized by a large N/Z asymmetry and located far from the valley of β stability on the nuclear chart, these magic numbers, viewed through observables, were shown to change. These changes in the regime of exotic nuclei offer an unprecedented view at the roles of the various components of the nuclear force when theoretical descriptions are confronted with experimental data on exotic nuclei where certain effects are enhanced. This article reviews the driving forces behind shell evolution from a theoretical point of view and connects this to experimental signatures.

DOI: 10.1103/RevModPhys.92.015002

CONTENTS

I. INTRODUCTION

The atomic nucleus is composed of protons and neutrons (collectively called *nucleons*) bound into one entity by nuclear forces. Its properties have been studied extensively for more than a century since its discovery by Rutherford (1911), providing a rather comprehensive picture of stable nuclei, i.e., nuclei with infinite or almost infinite lifetimes that are characterized by a balanced ratio of the number of neutrons (N) and protons (Z), e.g., $N/Z \sim 1$–1.5. Matter found on Earth is essentially made up of stable nuclei, including long-lived primordial isotopes like ^{235}U. Almost all matter in the visible Universe is composed of atomic nuclei.

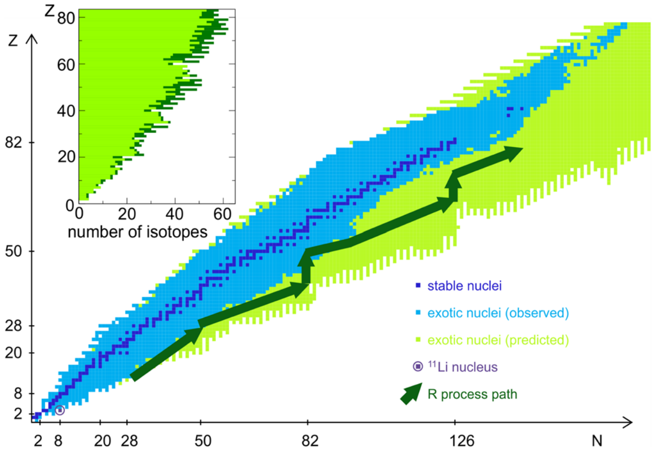

FIG. 1. The nuclear chart as a function of neutron and proton number N and Z. Each nucleus is represented by a box specified by Z and N. Dark-blue squares indicate stable nuclei. Exotic nuclei experimentally observed as of 2012 are shown by light-blue squares, while light-green squares denote those predicted by a theoretical model (Koura, 2005). The ^{11}Li nucleus is highlighted in purple. A possible path of the r process is indicated schematically by the green arrows. (Inset) Number of bound neutron-rich exotic nuclei as a function of Z based on Koura (2005). The light- and dark-green parts count nuclei with two-neutron separation energy $S_{2n} >$ and < 2 MeV, respectively. Adapted from Otsuka and Schwenk, 2012, and Otsuka, 2013.

While the overall picture had thus been conceived for stable nuclei, the landscape of atomic nuclei has been significantly expanded in recent years. This is associated with a major shift in the frontiers of nuclear physics from stable to exotic (or unstable) nuclei. Here exotic nuclei imply atomic nuclei with an unbalanced N/Z ratio as compared to stable ones, thus losing binding energy due to a large difference in Z and N (von Weizsäcker, 1935; Bethe and Bacher, 1936). Relatively small binding energies mean that β-decay channels open up, proceeding toward more N/Z balanced systems and resulting in finite (often short, subsecond) lifetimes.

Such extreme N/Z ratios impact not only lifetimes of exotic nuclei but also their quantum many-body structure relative to that of stable nuclei. This is the main subject of this review, with a particular emphasis on the variations of the nuclear shell structure.

Figure 1 shows a nuclear chart (or Segrè chart), where an individual nucleus is specified by two coordinates: Z and N. In Fig. 1, stable nuclei (dark-blue squares) stretch along a "line," called the β-stability line. Exotic nuclei are widely distributed as indicated by light-blue or light-green squares. Their existence limit on the neutron-rich (proton-rich) side is called the neutron (proton) dripline. Although a certain number of exotic nuclei have been familiar to nuclear physics since the

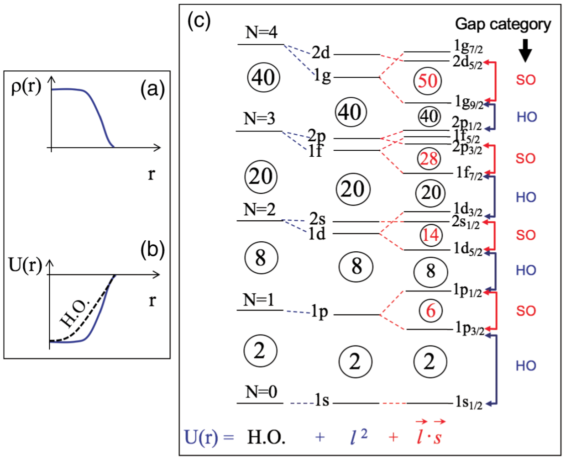

FIG. 2. (a) Nucleon density distribution $\rho(r)$ and (b) mean potential $U(r)$ are shown as a function of the distance from the center of the nucleus r. (c) Single-particle energies for a harmonic oscillator (HO) potential well, with an added ℓ^2 term and a spin-orbit (SO) interaction $\vec{\ell}\cdot\vec{s}$. Shell-gap categories are shown by HO and SO. The N label refers here to the oscillator shell $N = 2(n-1)+\ell$, with $n-1$ the number of nodes of the radial wave function and ℓ the orbital angular momentum. Adapted from Ragnarsson and Nilsson, 1995.

field's early days, systematic studies of them began in the 1980s. An example is the measurement of the matter radius of ^{11}Li (Tanihata *et al.*, 1985), marking a visible milestone in the development of experiments with radioactive ion (or rare-isotope) beams with the discovery of the neutron halo. Many other experiments have been conducted in recent decades, redrawing the nuclear landscape.

The nucleus ^{11}Li is known for its extraordinarily large matter radius due to the formation of a neutron halo, inherent to the last two loosely bound neutrons (Hansen and Jonson, 1987). The neutron halo is a characteristic phenomenon at or near the dripline that led us to change the canonical assumption that the nucleon density is almost constant inside the nucleus and that the nuclear radius is proportional to $A^{1/3}$, where $A = Z + N$ is the mass number. While ^{11}Li is located only four units away from the β-stability line on the nuclear chart, the distance between the β-stability line and the neutron dripline increases with Z (see Fig. 1). The nuclei shown in Fig. 1 are all bound. The inset of Fig. 1 counts the number of bound neutron-rich exotic nuclei. It starts with just a few for $Z \sim 1$, but it grows rapidly up to more than 50 for $Z = 82$. Weakly bound nuclei near the dripline are shown in dark green, where a neutron halo or phenomena connected to the continuum can be expected. One notices, however, that the majority of isotopes are still well bound. Partly because such well-bound exotic nuclei are so plentiful, but also because they span a remarkable range of N/Z, we can ask ourselves whether the structure of those many nuclei is just like that of the stable ones. If not, an intriguing question arises: what changes can be expected in extremely N/Z asymmetric nuclei and why?

We also note that the r process, which creates heavy elements in explosive scenarios such as neutron star mergers or supernovae in a series of neutron capture reactions and decays, actually proceeds through extremely neutron-rich exotic nuclei (as shown schematically in Fig. 1). Thus, for understanding how the elements in the Universe are formed, the study of the properties of exotic nuclei is essential.

The advent of radioactive ion beam facilities worldwide, together with constantly improved experimental techniques, has enabled a more thorough verification or discovery of the structure changes in exotic nuclei and ultimately allowed the nuclear driplines for some isotopes to be reached.

Atomic nuclei show shell structure expressed in terms of the single-particle orbits of protons and neutrons, similar to electrons in an atom. Such a shell structure was proposed originally by Haxel, Jensen, and Suess (1949) and Mayer (1949), and it has provided a firm footing for various studies on the structure of stable nuclei. It has been found in recent years that the shell structure changes as a function of Z and N in exotic nuclei, and this change is often referred to as *shell evolution*. While there has been enormous progress in the physics of exotic nuclei, we concentrate in this article rather on the shell evolution, partly because this subject alone is exhaustive and also because shell evolution is linked to a large variety of observables, phenomena, and features of current interest in the field. A primer on nuclear shell structure is presented in Sec. II.

In Sec. III, we review the definition of the monopole component of the NN interaction in a pedagogical way. Although the monopole interaction has been discussed since Bansal and French (1964), open questions remain. The effective single-particle energies (ESPEs) are then derived from the monopole interaction and are shown to be consistent with earlier derivations [see, e.g., Baranger (1970)]. The variation of the ESPEs as a function of N or Z is shown to be a robust mechanism behind shell evolution.

In Sec. IV, we discuss the major sources of the monopole interaction. In addition to the central force, the tensor force is considered, and the unique features of its monopole interaction are reviewed. The treatment of the tensor force in other theories is summarized. The monopole effects of the two-body spin-orbit force are discussed in Sec. IV.F.

Several features of nuclear forces related to the shell evolution are presented in Sec. V, starting with the renormalization property of the tensor force and followed by some properties obtained by a spin-tensor decomposition. The monopole effect of the three-nucleon force is discussed. Finally, in Sec. V, we also present a brief overview of *ab initio* approaches.

Examples of structural changes are discussed in Sec. VI before a summary is given in Sec. VII.

Some specific topics and discussions are included in the Supplemental Material (364).

II. NUCLEAR SHELL STRUCTURE: A PRIMER

Here we briefly describe the nuclear shell structure, starting with the nucleon distributions in nuclei. Extensive precision electron scattering experiments carried out on stable targets starting in the 1960s combined with other experiments showed that the nucleon density $\rho(r)$ is essentially constant well inside the nucleus, with smooth but rapid damping at the surface, as shown in Fig. 2(a): the paradigm of density saturation. The mean potential for a nucleon inside the nucleus represents the mean effects of the nucleon-nucleon (NN) interaction, or the nuclear force, as generated by the other nucleons. The NN interaction between free nucleons is strongly repulsive at short distances (below 0.7 fm), becomes attractive at medium range ($\approx$1.0 fm), and practically vanishes at large distances (beyond 2 fm). In the nuclear interior, the nuclear density is $\sim$0.17 nucleons/fm^3. For the description of nucleons confined in the nucleus, an effective NN interaction that incorporates various renormalization effects, such as in-medium effects, short-range correlation effects, *etc.*, is used. Those nucleons interact mainly with their immediate neighbors, which leads to a saturation of the binding energy. Combining those properties of the density and the nuclear force, a nucleon well inside the nucleus is subject to the same mean effect independent of its location. In other words, the mean potential has a flat bottom. The potential becomes gradually shallower toward the surface, as shown in Fig. 2(b). Such a mean potential can be further modeled by a harmonic oscillator (HO) potential that is also shown in Fig. 2(b). For that, the nucleons move on the orbits that are the eigenstates of this HO potential, and the energies are given in terms of the oscillator quanta $\mathcal{N}$, as shown in the column “H.O.” In order to resolve systematic discrepancies with experiment, Mayer and Jensen included the spin-orbit (SO) coupling $\vec{\ell} \cdot \vec{s}$, where $\vec{\ell}$ and $\vec{s}$ denote, respectively, the orbital angular momentum and the spin of nucleon (Haxel, Jensen, and Suess, 1949; Mayer, 1949). This $\vec{\ell} \cdot \vec{s}$ term with the proper strength produces the spin-orbit splitting, where the orbit with the total angular momentum $j_> = \ell + 1/2$ becomes lower than the one with $j_< = \ell - 1/2$. The resultant single-particle levels are shown in the right column in Fig. 2(c).

Without the SO coupling, the single-particle states are classified by the $\mathcal{N}$ and ℓ quantum numbers, as shown in the center column of Fig. 2(c). The single-particle states are grouped according to $\mathcal{N}$, forming *shells*. Shells are separated by *shell gaps*. The number of protons or neutrons below a certain gap defines a *magic number*. The magic number is related to the stability of the nucleus: for instance, up to 20 protons can be put into the shells formed by the $2s$, $1d$, $1p$, and $1s$ orbits, whereas the 21st protons must occupy either the $1f$ or $2p$ orbit at higher energy (i.e., leading to a smaller binding energy). Beyond the magic number 20, the SO coupling splits the $1f$ orbit into $1f_{7/2}$ and $1f_{5/2}$ sufficiently strong and creates a magic number at 28, as shown in Fig. 2(c). The $1f_{7/2}$ orbit is bordered in this figure by two magic numbers, 20 and 28: the former has a HO origin, whereas the latter has a SO origin. Other shells and magic numbers are shown in the same figure. While $N = 40$ is a subshell gap, all magic nuclei above $N = 40$ are of the SO origin. The major magic numbers, which correspond to large shell gaps, are 2, 8, 20, 28, 50, 82, and 126. This shell structure and the corresponding magic numbers turn out to be extremely successful in the description of the nuclei.

Note that the previous argument is based only on a few robust properties: density saturation, the short range of the nuclear force, and the existence of spin-orbit splitting. This independent-particle model, where nucleons are confined by a potential without interacting with each other, can formally be refined through the Hartree-Fock (HF) method, based on effective NN interactions. Figure 3(a) shows this schematically: a HF calculation for Z and N being magic numbers is supposed to produce the corresponding HF ground state, which is a closed shell. For this ground state, single-particle energies for particle (and hole) states are obtained within the HF framework, yielding Mayer-Jensen’s shell structure; see Fig. 2(c). We now add nucleons to orbits above the closed shell called valence orbits. Figure 3(b) shows, still schematically, that the single-particle energies are shifted due to those added nucleons, mediated by the monopole interaction (indicated by the green wavy line in the figure), which is a component of the nuclear force. The monopole interaction shifts single-particle energies effectively without mixing different orbits, and its effect depends only on the occupation numbers of individual orbits; see Sec. III for details. Such energy shifts represent shell evolution and manifest themselves systematically in a variety of observables measured for exotic nuclei. They also represent one of the main subjects of this review.

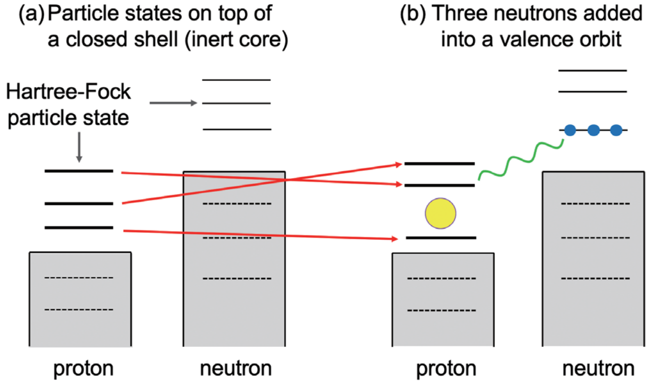

FIG. 3. Schematic illustrations of (a) closed-shell and single-particle states in a Hartree-Fock picture and (b) single-particle states with additional neutrons in a valence orbit (small blue circles). The large yellow circle indicates a subshell gap. The green wavy line denotes the monopole interaction.

Figure 3(b) shows a small energy gap between two proton orbits (yellow circle). Such energy gaps can appear as Z and/or N changes. If such gaps become large enough, they may result in new magic numbers. Alternatively, some of the conventional magic numbers may disappear. We shall see how the shell structure changes or evolves over the Segrè chart.

We stress that the single-particle orbits shown in Fig. 3 are obtained for a spherical closed shell, i.e., a spherical HF ground state. This is the picture for most of the discussions in this article. For the majority of nuclei, however, their shape is nonspherical (deformed). Nuclear deformation has been studied extensively since Rainwater (1950), Bohr (1952), and Bohr and Mottelson (1953) as one of the major subjects of nuclear physics (Bohr and Mottelson, 1975). The deformation can be described in terms of various correlations of nucleons in the single-particle orbits. Besides, the HF solution itself can be deformed in some cases, where the mean field is not isotropic and the HF ground state is not spherical. With the onset of deformation, deformed shell gaps can develop and lead to deformed magic numbers. This is related to nuclear shape coexistence, i.e., the appearance of states with different shapes at similar energies; see reviews by Heyde *et al.* (1985),

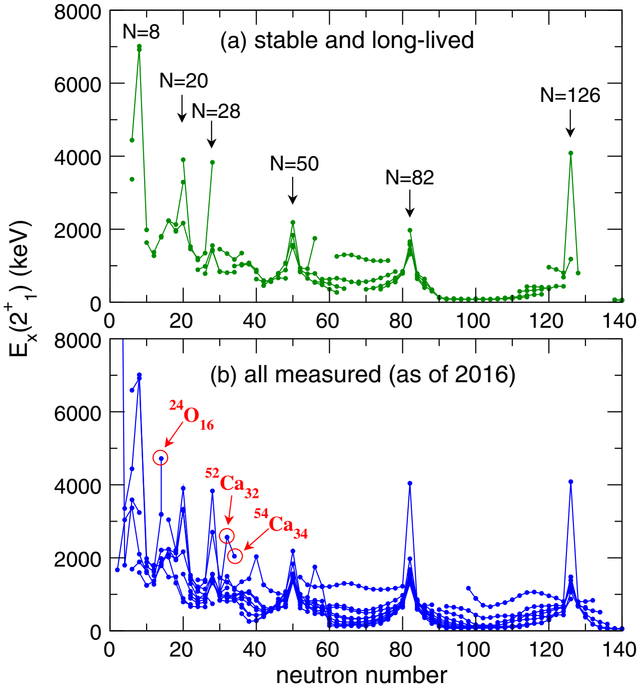

FIG. 4. Systematics of the first 2^+ levels, for (a) stable and long-lived nuclei, and (b) all nuclei included measured up to 2016 (Pritychenko *et al.*, 2016).

Wood *et al.* (1992), Heyde and Wood (2011), and Wood and Heyde (2016). Such a situation can be found in many nuclei (Heyde *et al.*, 1985; Wood *et al.*, 1992; Heyde and Wood, 2011).

Coming back to spherical magic numbers, experimental hints of their appearance or disappearance are visible, for example, in the excitation energy of the first 2^+ state. In the ground state of a magic nucleus, protons and neutrons fill single-particle orbits up to a magic number and the corresponding large energy gap, and hence nucleons must be excited across those gaps to form excited states. Thus, the excitation energy becomes large, as with the relevant energy gaps. Because the first 2^+ state is the lowest excited state in many nuclei with even numbers of Z and N, high values of the lowest 2^+ level may indicate the occurrence of magic numbers. Figure 4(a) shows the 2^+_1 energies obtained for stable and long-lived (half-life > 30 days) nuclei as a function of N for many isotopic chains. Higher 2^+_1 levels point remarkably well to Mayer-Jensen's magic numbers. Figure 4(b) plots the 2^+_1 levels for all nuclei, including exotic ones, as of 2016. As compared to the picture based on Mayer-Jensen's scheme, additional elevated 2^+_1 energies stand out at $N = 16$ (^{24}O), 32 (^{52}Ca), and 34 (^{54}Ca) as well as at $N = 40$ (^{68}Ni). We note that 2^+_1 energies are impacted by a variety of correlations, such as pairing, for example, but for the extreme values they can be attributed to magic numbers. It should be remarked, however, that, while they provide useful first indicators for magic numbers, they are not a decisive fingerprint.

Figure 5 indicates schematically how shell closures at $N = 32$ and 34 may be seen in the neutron single-particle levels for the Ca and Ni isotopes. The figure shows the relevant single-particle level scheme of the Ni isotopes, which is consistent with Fig. 2(c), representing the situation in stable nuclei. This is confronted in the single-particle levels of the Ca isotopes, where additional subshell closures at neutron numbers 32 and 34 are shown, resulting in an ordering of the neutron orbitals in ^{52,54}Ca that is different from Fig. 2(c). We discuss throughout this review why and how such shell evolution occurs.

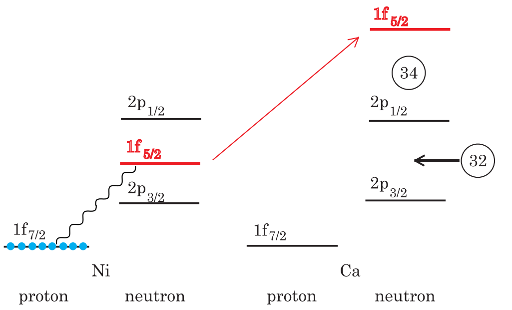

FIG. 5. Schematic illustration of shell evolution from Ni to Ca for neutron orbits. Light-blue circles represent protons. The wavy line implies the interaction between the proton $1f_{7/2}$ and the neutron $1f_{5/2}$ orbit. The numbers in circles indicate (semi)magic numbers. From Otsuka and Tsunoda, 2016.

Thus, the magic numbers and shell structure are not immutable and undergo change. As we look back several decades, the concept of rigid magic numbers was already being questioned in the 1970s upon the observation of anomalies in experimental masses, nuclear radii, and spectroscopy of nuclei far from stability, around $N = 20$, since Thibault *et al.* (1975), along with Huber *et al.* (1978), Détraz *et al.* (1979), and Guillemaud-Mueller *et al.* (1984). A much weakened effect of the $N = 20$ gap, combined with the emergence of deformed intruder states, was seen in various observables and interpreted to signal a change in the shell structure. We note that another earlier observation questioning conventional understanding was marked by the discovery of the abnormal ground state of ^{11}Be by Wilkinson and Alburger (1959), followed by a theoretical analysis by Talmi and Unna (1960).

Over the years, the local disappearance of many of the previously well-established shell gaps has been pointed out far from stability, leading to a revised picture of the magic numbers and shell structure in general. One of the goals of this review is to summarize the presently available understanding, to extract basic underlying mechanisms of the shell evolution, and to provide an overview of various nuclear phenomena related to them. Such outcomes allow us to anticipate new physics in hitherto unexplored regions of the Segrè chart.

In this review, the theoretical description of the structure of those nuclei is given mainly within the shell-model framework, which is known as configuration interaction method in other disciplines. Protons (neutrons) in valence orbits are called valence protons (neutrons). The shell-model description of atomic nuclei is made in terms of such valence orbits on top of the inert core (i.e., closed shell). Effects of states outside this scheme are expected to be included in effective NN interaction and effective operators, obtained in phenomenological, microscopic, or hybrid manners.

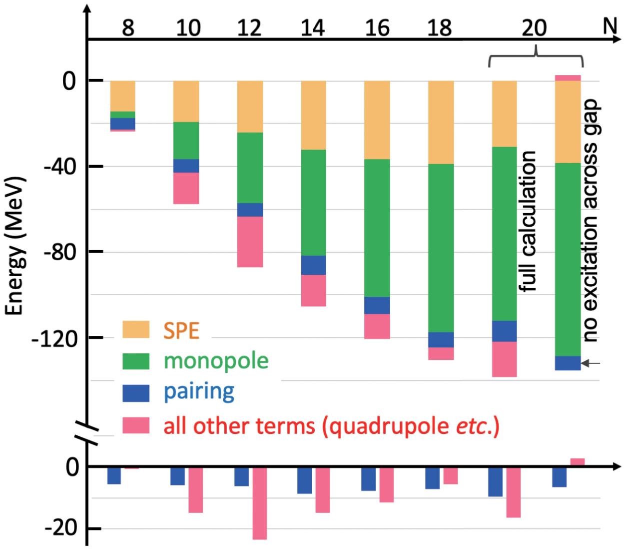

FIG. 6. Contributions of the monopole, pairing, and all other terms of the NN interaction to the ground-state energy of Mg isotopes with even N. The contribution from the single-particle energy (SPE) is included also. The other terms are dominated by a quadrupole interaction. The upper panel shows the cumulative contributions, while the lower one shows the variations of pairing and the other terms. For $N = 20$, the full calculation, including the excitations to the pf shell, is shown in comparison to the calculation without such excitations. For the latter, the small arrow indicates the ground-state energy because the "all other terms" calculation gives a repulsive contribution (a positive value). See the text for details.

The valence nucleons interact with each other through the effective NN interaction, and various configurations of valence nucleons are mixed in a shell-model eigenstate. Many-body correlations are important for the resulting eigenstates and can often be related to certain parts of the effective NN interaction. We decompose the effective NN interaction into three parts: (a) monopole as discussed previously, (b) pairing, and (c) all other terms. The pairing part corresponds to proton-proton and neutron-neutron interactions coupled to the angular momentum $J^{\pi} = 0^{+}$ (J, total angular momentum; π, parity), which is an extended version of the usual BCS-type pairing. All other terms account for the remaining parts.

Although the remaining parts include various types of interactions, dominant effects on the energy and structure of the ground and the low-lying states, which are of current interest, are due to the quadrupole interaction. Such quadrupole interactions can be modeled, to a good extent, by the coupling between quadrupole-moment operators. The quadrupole interaction has been studied extensively over decades, for instance, by Nilsson (1955), Elliott (1958), Bes and Sorensen (1969), Dufour and Zuker (1996), and Kaneko *et al.* (2011), while the SU(3) picture of the quadrupole moment (Elliott, 1958) was generalized, for instance, by Zuker *et al.* (2015).

Figure 6 shows the ground-state expectation values of these parts for the Mg isotopes with even $N = 8$–20, calculated with a shell model in the sd shell for $^{20-30}$Mg, and in the sd-pf shell for ^{32}Mg, where pf-shell configurations become important, as mentioned previously. The USD Hamiltonian interaction (Brown and Richter, 2006) is used for $^{20-30}$Mg. The SDPF-M interaction introduced in Utsuno *et al.* (1999) is taken for ^{32}Mg, while the calculation without the excitation from the sd to the pf shells is also shown for comparison. The expectation value of the single-particle-energy contribution increases in magnitude up to $N = 18$ since more neutrons occupy well-bound orbits (negative energies). The magnitude of the "monopole" contribution increases up to $N = 20$. The "pairing" contribution and that of the "other terms" are also shown separately in the bottom part of the figure. This part indicates clearly that the contribution of the pairing interaction does not change much. In contrast, the contribution of the other terms, dominated by the quadrupole interaction as previously mentioned, varies sharply with its maximum (in magnitude) at $N = 12$ (^{24}Mg). This is consistent with a large quadrupole moment of ^{24}Mg. The contribution of the other terms decreases up to $N = 18$, as the quadrupole deformation weakens. These trends resemble the ones shown in Fig. 4 of Heyde and Wood (2011) across a shell for heavy nuclei. At $N = 20$, an intruder state composed of many particle-hole excitations is energetically favored over normal configurations (i.e., no particle-hole excitations across the $N = 20$ magic gap) and becomes the ground state. To this state, the contribution of the other terms becomes large, only a little smaller than for ^{24}Mg, pointing to a strongly deformed ground state. The monopole and pairing contributions increase as well from $N = 18$ to 20, but the "SPE" contribution is reduced due to particle-hole excitations across the $N = 20$ gap. For comparison, results of a calculation are shown without cross-shell excitations, resulting in almost no quadrupole correlations and a higher energy. Thus, the Mg isotopes show varying deformation and the phenomenon of shape coexistence at $N = 20$ (Heyde and Wood, 2011). The features shown here apply to many isotopic chains across the nuclear chart. The three parts, monopole, pairing, and other terms, exhibit sizable contributions with notable variations. In this article, we highlight the important role of the monopole interaction in describing structural changes mainly from the shell-model viewpoint.

The Hartree-Fock calculation discussed in Fig. 3 corresponds to a spherical ground state. Considering the strong quadrupole and higher multipole interactions, deformed ground states may occur and can be described through deformed HF configurations. A nonspherical mean potential is obtained, and the HF ground state becomes the intrinsic state of a rotational band (Ring and Schuck, 1980). There exists an extensive literature on the deformed HF description of shape coexistence; see, e.g., Wood *et al.* (1992), Reinhard *et al.* (1999), and Heyde and Wood (2011).

We now comment on the comparisons of the shell structure of atomic nuclei to the shell structure of other many-body systems. First, as the nuclear potential is generated by its constituents, shell structure changes from nucleus to nucleus, leading to shell evolution. We mention here that shell structure appears in other mesoscopic systems such as metallic clusters, as described, for instance, by Sugano (1991), Knight *et al.* (1984), and Clemenger (1985), where the correspondence to the classical motion and geometrical symmetries is important.

It has been argued that the damping of the nucleon density in the radial direction may be more gradual in neutron-rich exotic nuclei than in stable nuclei, causing reduced spin-orbit splittings and single-particle levels that are distributed more evenly (Dobaczewski *et al.*, 1994), sometimes referred to as "shell quenching." This hypothetical phenomenon is predicted to be found at or near the dripline, confined to weakly bound systems, and remains a challenge for future experiments. This review addresses the shell evolution driven by the combination of characteristic features of nuclear forces and extreme neutron:proton ratios of the nucleus.

III. MONOPOLE INTERACTION AND EMPIRICAL ANALYSIS BASED ON IT

The shell structure can be specified by a set of single-particle energies of valence (or active) orbits on top of a closed shell (or inert core). As more neutrons or protons are added to a nucleus, the single-particle energies of those valence orbits may change due to the interaction between valence nucleons. This implies some changes of shell structure, called *shell evolution*, as introduced in Sec. I. The shell evolution is generated by the monopole part of the nucleon-nucleon (NN) interaction, which will be referred to hereafter as the *monopole interaction*. The NN interaction here represents an effective one for nucleons in nuclei. Although there can be a variety of such interactions, from fitted to microscopically derived ones including hybrid versions, we discuss their general properties. Here we first introduce the definition of the monopole interaction, and we discuss how it acts. The monopole interaction was discussed in the past, for instance, by Bansal and French (1964) and Poves and Zuker (1981). We introduce the monopole interaction in a different way, as an average of correlation energies of two nucleons in an open-shell nucleus, without referring to closed-shell energies. The final outcome of this formulation turns out to be basically consistent with those earlier works.

The effective single-particle energy will then be defined for open-shell nuclei in a close connection to the monopole interaction there, in a possibly more transparent and straightforward way than the simple interpolation between the beginning and end of a given shell.

We then move forward to the evolution of the shell structure by defining effective single-particle energies with this monopole interaction. We also present applications of the monopole interaction to some examples taken from actual nuclei. At this point, we stress that the monopole interaction is a part of the NN interaction, and that the rest of the interaction produces various dynamical correlations and must be taken into account for an actual description of the nuclear structure. Nevertheless, as the monopole interaction generates unique and crucial effects, it deserves special effort and attention.

A. Monopole interaction

We start with single-particle orbits. For each orbit, the total angular momentum is specified by $\vec{j} = \vec{\ell} + \vec{s}$, with its orbital angular momentum $\vec{\ell}$ and spin $\vec{s}$. The single-particle orbits are labeled by the magnitudes of their $\vec{j}$'s, referred to as $j, j', \ldots$ hereafter. They are combined with the corresponding magnetic quantum numbers, $m, m', \ldots$ as $(j, m), (j', m'), \ldots$. The symbols $j, j', \ldots$ are put in a fixed order and may carry implicitly such a sequential ordering, as well as other quantum numbers like the node of the radial wave function n. Having these single-particle orbits on top of the inert core (i.e., closed shell), we denote the SPEs of those orbits as $\epsilon_j^0, \epsilon_{j'}^0, \ldots$. As usual, this SPE ϵ_j^0 stands for the sum of the kinetic energy of a nucleon on this orbit j and the total effects of nuclear forces on this nucleon from all nucleons in the inert core.

We begin with the simpler case by assuming that there is only one kind of nucleons, e.g., neutrons. The Hamiltonian is expressed then as

$$\hat{H}_n = \sum_j \epsilon_j^0 \hat{n}_j + \hat{v}_{nn}, \tag{1}$$

where $\hat{n}_j$ denotes the number operator for the orbit j and $\hat{v}_{nn}$ stands for the neutron-neutron effective interaction.

The product state with the first and second neutron in the states j, m and j', m', respectively, is written as

$$|j, m \otimes j', m'). \tag{2}$$

Their antisymmetrized state is indicated by

$$|j, m; j', m'\rangle = \{|j, m \otimes j', m') - |j', m' \otimes j, m)\}/\sqrt{2}. \tag{3}$$

A two-body interaction between two neutrons can be written as

$$\hat{v}_{nn} = \sum_{(j_1,m_1;j_1',m_1'),(j_2,m_2;j_2',m_2')} \langle j_1, m_1; j_1', m_1' | \hat{v}_{nn} | j_2, m_2; j_2', m_2' \rangle \times a^\dagger_{j_1,m_1} a^\dagger_{j_1',m_1'} a_{j_2',m_2'} a_{j_2,m_2}, \tag{4}$$

where $(j, m; j', m')$ in the summation is an ordered pair of two states j, m and j', m', $\langle \cdots | \hat{v} | \cdots \rangle$ denotes an antisymmetrized two-body matrix element, and $a^\dagger_{j,m}$ ($a_{j,m}$) implies the creation (annihilation) operator of the state j, m. Regarding the ordered pair $(j_1, m_1; j_1', m_1')$, we can assume without loss of generality that $m_1 < m_1'$ if $j_1 = j_1'$ or $j_1 < j_1'$ in their prefixed ordering, as mentioned previously.

The monopole interaction is defined as a component extracted from a given interaction, $\hat{v}_{nn}$, so that it represents the effect averaged over all possible orientations of two neutrons in the orbits j and j'. Here orientations refer to various combinations of m and m' within the orbits j and j'. Figure 7 provides a general visualization of the monopole matrix element, exhibiting different orientations by differently tilted orbiting planes. In order to formulate this, the monopole matrix element for the orbits j and j' is defined as

$$V_{nn}^m(j, j') = \frac{\sum_{(m,m')} \langle j, m; j', m' | \hat{v}_{nn} | j, m; j', m' \rangle}{\sum_{(m,m')} 1}, \tag{5}$$

where the summation over m, m' is taken for all ordered pairs allowed by the Pauli principle.

As the denominator counts the number of allowed states, this is exactly the average mentioned previously. The monopole interaction as an operator is then expressed as

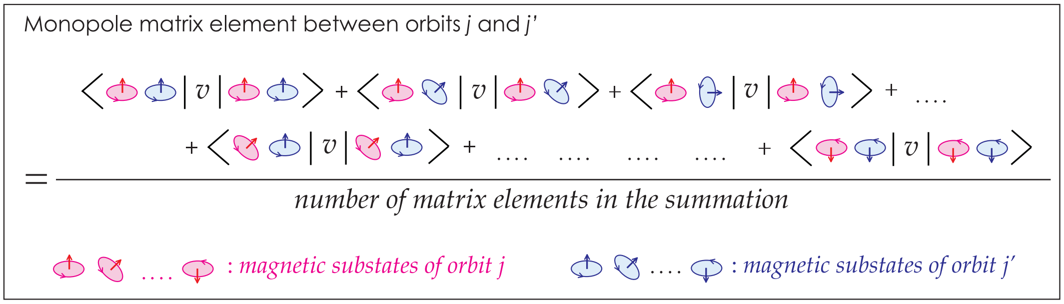

FIG. 7. A schematic visualization of monopole matrix elements for the two-body interaction v.

$$\hat{v}_{nn,\mathrm{mono}} = \sum_{j\le j'} \hat{v}^m_{nn}(j,j'), \tag{6}$$

with

$$\hat{v}^m_{nn}(j,j') = V^m_{nn}(j,j')\Sigma_{m,m'} a^\dagger_{j,m} a^\dagger_{j',m'} a_{j',m'} a_{j,m}. \tag{7}$$

After simple algebra, this turns out to be

$$\hat{v}^m_{nn}(j,j') = \begin{cases} V^m_{nn}(j,j)\frac{1}{2}\hat{n}_j(\hat{n}_j - 1), & \text{for } j = j', \\ V^m_{nn}(j,j')\hat{n}_j\hat{n}_{j'}, & \text{for } j \ne j', \end{cases} \tag{8}$$

where $\hat{n}_j$ stands for the number operator for the orbit j. The form in Eq. (8) appears to be in accordance with what can be expected intuitively, from the standpoint of average, for identical fermions. The two neutrons in the orbits j and j' can be coupled to the total angular momentum J, where $\vec{J} = \vec{j} + \vec{j}'$, and the wave function with a good J value is given by a particular superposition of the states in Eq. (3) over all possible values of m and m'. It is obvious that the effects of the monopole interaction in Eq. (8) is independent of the total angular momentum J. We emphasize again that the monopole interaction is simply an average of a given general interaction over all possible orientations, and its effect can be expressed by the orbital number operator as in Eq. (8) for the neutron-neutron interaction.

We next discuss systems composed of protons and neutrons. The total Hamiltonian is then written as

$$\hat{H} = \hat{H}_n + \hat{H}_p + \hat{v}_{pn}, \tag{9}$$

where $\hat{H}_p$ stands for the proton Hamiltonian defined as in Eq. (1) and $\hat{v}_{pn}$ represents the proton-neutron effective interaction.

The proton and neutron number operators in the orbit j are denoted as $\hat{n}^p_j$ and $\hat{n}^n_j$, respectively. We introduce the isospin operators in the orbit j: $\hat{\tau}^+_j$, $\hat{\tau}^-_j$, and $\hat{\tau}^z_j$. We adopt the convention that protons are in the state of isospin z component $\tau_z = +1/2$, whereas neutrons are in $\tau_z = -1/2$. Here $\hat{\tau}^+_j$ ($\hat{\tau}^-_j$) denotes the operator changing a neutron (proton) to a proton (neutron) in the same (j, m) state, and $\hat{\tau}^z_j$ equals $(\hat{n}^p_j - \hat{n}^n_j)/2$. In other words, $\hat{\tau}^+_j$ and $\hat{\tau}^-_j$ are the isospin raising and lowering operators restricted to the orbit j, while $\hat{\tau}^0_j$ is its z component.

The magnitude of the usual isospin, i.e., not specific to an orbit, is denoted by T, including that of two nucleons interacting through the NN interaction.

We now discuss the proton-neutron monopole interaction. Although the basic idea remains the same as the previous case for two neutrons, certain differences arise. To be precise, a proton and a neutron are coupled in a symmetric way for the $T = 0$ case, and in an antisymmetric way for the $T = 1$ case. Details of the discussions are presented in Sec. S1 of the Supplemental Material (364), and we show here only major points, referring to the corresponding parts there.

The monopole interaction due to the $T = 0$ part of $\hat{v}_{pn}$ is expressed as [see the discussions in Sec. S1 up to Eq. (S16) in the Supplemental Material (364)]

$$\begin{aligned} \hat{v}_{pn,\,\mathrm{mono},T=0} = & \sum_{j,j'} V^m_{T=0}(j,j')\frac{1}{2}\hat{n}^p_j\hat{n}^n_{j'} \\ & - \sum_{j<j'} V^m_{T=0}(j,j')\frac{1}{2}\{\hat{\tau}^+_j\hat{\tau}^-_{j'} + \hat{\tau}^-_j\hat{\tau}^+_{j'}\} \\ & - \sum_{j} V^m_{T=0}(j,j)\frac{1}{2}:\hat{\tau}^+_j\hat{\tau}^-_j:, \end{aligned} \tag{10}$$

where the symbol $:\cdots:$ denotes a normal product, and the $T = 0$ monopole matrix element is defined as an average over states with all possible orientations with the symmetric coupling of proton and neutron, as indicated by $\mathcal{S}$ [see the discussions in Sec S1 of the Supplemental Material (364) linked to Eqs. (S5) and (S15)]:

$$V^m_{T=0}(j,j') = \frac{\sum_{(m,m')}(m;m'\colon\mathcal{S}|\hat{v}_{pn}|m;m'\colon\mathcal{S})}{\sum_{m,m'}1}. \tag{11}$$

If the interaction $\hat{v}$ is isospin invariant as usual, the monopole matrix element in Eq. (5) is the $T = 1$ monopole matrix element,

$$V^m_{T=1}(j,j') = V^m_{nn}(j,j'). \tag{12}$$

Coming back to antisymmetric couplings of a proton and a neutron, we apply the procedures similar to those for $T = 0$ states, and we obtain [see the discussions in Sec. S1 of the Supplemental Material (364) linked to Eq. (S22)]

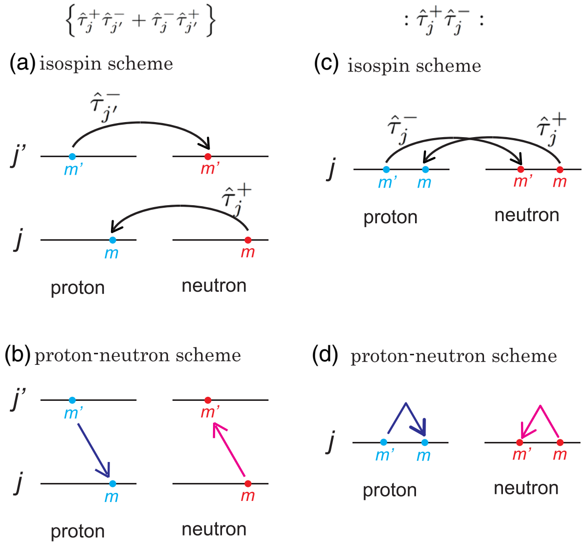

FIG. 8. Implication of $\hat{\tau}^+_j\hat{\tau}^-_{j'}$ terms. (a) and (c) are for the $\{\hat{\tau}^+_j\hat{\tau}^-_{j'}+\hat{\tau}^-_j\hat{\tau}^+_{j'}\}$ and $:\hat{\tau}^+_j\hat{\tau}^-_j:$ cases in the isospin scheme, respectively. (b) and (d) are similar to (a) and (c), respectively, in the proton-neutron scheme. The magnetic substates are indicated by m and m'.

$$\begin{aligned}\hat{v}_{pn,\,\mathrm{mono},T=1} = {} & \sum_{j,j'} V^m_{T=1}(j,j')\frac{1}{2}\hat{n}^p_j\hat{n}^n_{j'} \\ & + \sum_{j<j'} V^m_{T=1}(j,j')\frac{1}{2}\{\hat{\tau}^+_j\hat{\tau}^-_{j'}+\hat{\tau}^-_j\hat{\tau}^+_{j'}\} \\ & + \sum_{j} V^m_{T=1}(j,j)\frac{1}{2}{:}\hat{\tau}^+_j\hat{\tau}^-_j{:}. \qquad (13)\end{aligned}$$

By combining Eqs. (10) and (13), the whole expression of the proton-neutron monopole interaction becomes

$$\begin{aligned}\hat{v}_{pn,\mathrm{mono}} = {} & \sum_{j,j'}\frac{1}{2}\{V^m_{T=0}(j,j')+V^m_{T=1}(j,j')\}\hat{n}^p_j\hat{n}^n_{j'} \\ & - \sum_{j<j'}\frac{1}{2}\{V^m_{T=0}(j,j')-V^m_{T=1}(j,j')\}\{\hat{\tau}^+_j\hat{\tau}^-_{j'}+\hat{\tau}^-_j\hat{\tau}^+_{j'}\} \\ & - \sum_{j}\frac{1}{2}\{V^m_{T=0}(j,j)-V^m_{T=1}(j,j)\}{:}\hat{\tau}^+_j\hat{\tau}^-_j{:}. \qquad (14)\end{aligned}$$

Although the meaning of the first term on the right-hand side of Eq. (14) is straightforward, it needs some explanation to understand the other two terms in depth. Figure 8 may help, by showing how they work. In the case of $j \neq j'$, Figs. 8(a) and 8(b) indicate the same process in the isospin and proton-neutron schemes, respectively. Figure 8(a) indicates that the $\{\hat{\tau}^+_j\hat{\tau}^-_{j'}+\hat{\tau}^-_j\hat{\tau}^+_{j'}\}$ term produces a monopole interaction with a charge exchange process, whereas the same process may look different in Fig. 8(b). Figures 8(c) and 8(d) are for the case of one orbit j with similar implications. One thus see, from Fig. 8, how the charge exchange processes can be incorporated into the monopole interaction. We come back to this figure later. We note that the $T = 0$ and $T = 1$ monopole matrix elements contribute with opposite sign relations compared to the first term.

The neutron-neutron and proton-proton monopole interactions can be rewritten in a similar way as

$$\hat{v}_{nn,\mathrm{mono}} = \sum_{j} V^m_{T=1}(j,j)\frac{1}{2}\hat{n}^n_j(\hat{n}^n_j-1) + \sum_{j<j'} V^m_{T=1}(j,j')\hat{n}^n_j\hat{n}^n_{j'} \qquad (15)$$

and

$$\hat{v}_{pp,\mathrm{mono}} = \sum_{j} V^m_{T=1}(j,j)\frac{1}{2}\hat{n}^p_j(\hat{n}^p_j-1) + \sum_{j<j'} V^m_{T=1}(j,j')\hat{n}^p_j\hat{n}^p_{j'}. \qquad (16)$$

We thus gain the complete expression for the total monopole interaction,

$$\hat{v}_{\mathrm{mono}} = \hat{v}_{pp,\mathrm{mono}} + \hat{v}_{nn,\mathrm{mono}} + \hat{v}_{pn,\mathrm{mono}}. \qquad (17)$$

B. Multipole interaction

We have discussed the monopole interaction that is a part of the NN interaction. The remaining part of the NN interaction is called the *multipole interaction*. The multipole interaction is often expressed as $\hat{v}_M$, and it includes, in particular, the quadrupole interaction. In this review, we denote the multipole interaction as $\hat{v}_{\mathrm{multi}}$, which is defined by

$$\hat{v}_{\mathrm{multi}} = \hat{v} - \hat{v}_{\mathrm{mono}}, \qquad (18)$$

where $\hat{v}$ stands for the full interaction and $\hat{v}_{\mathrm{mono}}$ is defined in Eq. (17). The multipole interaction may have the subscript pp, nn, or pn if necessary.

We note that, although the notion of the multipole interaction has appeared, for instance, in Brown and Kuo (1967), including the importance of the quadrupole and hexadecupole forces, the multipole interaction in the present sense was introduced, as "nonmonopole," by Poves and Zuker (1981). A model of the multipole interaction was introduced and developed in a global description of collective states by Dufour and Zuker (1996).

C. Monopole matrix element in the *j-j* coupling scheme

The monopole matrix element is defined, in some cases, by an alternative but equivalent expression,

$$V^m_T(j,j') = \frac{\sum_J (2J+1)\langle j,j';J,T|\hat{v}|j,j';J,T\rangle}{\sum_J (2J+1)} \quad \text{for } T = 0 \text{ and } 1, \qquad (19)$$

where J takes only even (odd) integers for $j = j'$ with $T = 1$ ($T = 0$). Section S2 of the Supplemental Material (364) shows that this expression is indeed equivalent to the one presented here.

The closed-shell properties are derived from the expressions shown thus far. The actual derivations and results are given in Sec. S3 of the Supplemental Material (364).

D. Effective single-particle energy

We discuss here effective single-particle energy and its derivation from the monopole interaction.

As one moves on the Segrè chart, the proton number Z and the neutron number N change, and the single-particle energy (SPE) ϵ_j^0 mentioned in Sec. III.A changes also. This change has the following two aspects. One is due to the kinetic energy: as A increases, the radius of the nucleus becomes larger, and consequently the radial wave function of each orbit becomes wider. This lowers the kinetic energy. The other aspect is the variation in the effects from nucleons in the inert core. As A increases, the radial wave functions of the orbits in the inert core also become stretched out radially. This can reduce the magnitude of their effects. While these two changes can be of relevance, for instance, over a long chain of isotopes, they are considered to be rather minor within each region of current interest on the Segrè chart (Bohr and Mottelson, 1969), and we do not take them into account in this article.

The SPE has another origin: the contribution from other nucleons outside the inert core, i.e., valence nucleons. This valence contribution to the orbit j is referred to as $\hat{\epsilon}_j$ hereafter. The total single-particle energy, usually called *effective single-particle energy* (ESPE), is denoted as

$$\epsilon_j = \epsilon_j^0 + \hat{\epsilon}_j. \tag{20}$$

We discuss here the valence contribution $\hat{\epsilon}_j$ in some detail. Note that ϵ_j^0 is a constant as stated, whereas $\hat{\epsilon}_j$ is an operator by nature because of its dependence on the states of other valence nucleons.

The magnetic substates of the orbits j and j' are denoted by m ($m=j,j-1,\ldots,-j+1,-j$) and m' ($m'=j',j'-1,\ldots,-j'+1,-j'$), respectively. The matrix element $\langle m,m'|\hat{v}|m,m'\rangle$ varies for different combinations of m and m'. On the other hand, as $\hat{\epsilon}_j$ is a part of the single-particle energy of the orbit j, it should be independent of m. We therefore extract the m-independent component from these matrix elements in order to evaluate their contribution to $\hat{\epsilon}_j$. Because of the m and m' dependences, this can be done by taking the average over all possible combinations of m and m', which is the monopole interaction discussed in Sec. III.A.

In the case of two neutrons in the same orbit j, the monopole interaction is included in Eq. (15). The difference due to the addition of one neutron, $\hat{n}_j^n \to \hat{n}_j^n + 1$, gives the contribution to $\hat{\epsilon}_j$ as

$$\begin{aligned}\Delta^{(j,nn)}\epsilon_j &= V^m_{T=1}(j,j)\tfrac{1}{2}\{(\hat{n}_j^n+1)\hat{n}_j^n - \hat{n}_j^n(\hat{n}_j^n-1)\}\\ &= V^m_{T=1}(j,j)\hat{n}_j^n.\end{aligned} \tag{21}$$

The difference due to the increase, $\hat{n}_j^n \to \hat{n}_j^n + 1$, for $j \neq j'$ is written as

$$\begin{aligned}\Delta^{(j',nn)}\epsilon_j &= V^m_{T=1}(j,j')\{\hat{n}_{j'}^n(\hat{n}_j^n+1) - \hat{n}_{j'}^n\hat{n}_j^n\}\\ &= V^m_{T=1}(j,j')\hat{n}_{j'}^n.\end{aligned} \tag{22}$$

Thus, the contribution from the neutron-neutron interaction results in

$$\hat{\epsilon}_j^{n\to n} = \sum_{j'} V^m_{T=1}(j,j')\hat{n}_{j'}^n. \tag{23}$$

The contribution from the proton-proton interaction can be shown similarly,

$$\hat{\epsilon}_j^{p\to p} = \sum_{j'} V^m_{T=1}(j,j')\hat{n}_{j'}^p. \tag{24}$$

In the case of the proton-neutron interaction, the monopole interaction is shown in Eq. (14). We first discuss the effect from the first term on the right-hand side. The difference due to the increase, $\hat{n}_j^n \to \hat{n}_j^n + 1$, gives the contribution to $\hat{\epsilon}_j$ (of the neutrons) as

$$\begin{aligned}\hat{\epsilon}_j^{p\to n;0} &= \sum_{j'}\frac{1}{2}\{V^m_{T=0}(j',j) + V^m_{T=1}(j',j)\}\\ &\quad\times\{\hat{n}_{j'}^p(\hat{n}_j^n+1) - \hat{n}_{j'}^p\hat{n}_j^n\}\\ &= \sum_{j'}\frac{1}{2}\{V^m_{T=0}(j',j) + V^m_{T=1}(j',j)\}\hat{n}_{j'}^p.\end{aligned} \tag{25}$$

Likewise, the difference due to the increase, $\hat{n}_j^p \to \hat{n}_j^p + 1$, gives the contribution to $\hat{\epsilon}_j$ (of the protons) as

$$\hat{\epsilon}_j^{n\to p;0} = \sum_{j'}\frac{1}{2}\{V^m_{T=0}(j,j') + V^m_{T=1}(j,j')\}\hat{n}_{j'}^n. \tag{26}$$

We next discuss the effect from the second and third terms on the right-hand side of Eq. (14). Because the operator $\hat{\tau}_j^+\hat{\tau}_{j'}^- + \hat{\tau}_j^-\hat{\tau}_{j'}^+$ working between $j \neq j'$ shifts a proton $j' \to j$ and a neutron $j \to j'$, and vice versa [see Figs. 8(a) and 8(b)], the second term does not contribute to the ESPE. Note that effects of this term are fully included when the Hamiltonian is diagonalized.

The situation is different for the last term on the right-hand side of Eq. (14), $:\hat{\tau}_j^+\hat{\tau}_j^-:$. Note that the protons and neutrons occupy the same orbit j now. Since the term $-:\hat{\tau}_j^+\hat{\tau}_j^-:$ exchanges a proton and a neutron, a subset of its effect is relevant now if this term both annihilates a proton and a neutron both in the *same* magnetic substate m and creates them in exactly the same substate. Formally speaking, this process cannot be written like the first term on the right-hand side of Eq. (14). We, however, can introduce a practical approximation. If there are n_j^n neutrons in the orbit j, they can be assumed, in the first approximation, to be equally distributed over all possible m states. In this equal distribution approximation, a proton in the magnetic substate m can feel an interaction with a neutron in the substate m with a probability $\hat{n}_j^n/(2j+1)$. This approximation can be expressed as

$$-:\hat{\tau}_j^+\hat{\tau}_j^-: \sim \frac{\hat{n}_j^p\hat{n}_j^n}{2j+1}. \tag{27}$$

This approximation can be understood also by considering the case of $m = m'$ in Fig. 8(d). By combining Eq. (27) with the first term on the right-hand side of Eq. (14), we define the *effective* proton-neutron monopole interaction as

$$\hat{v}_{pn,\mathrm{mono-eff}} = \sum_{j\neq j'}\frac{1}{2}\{V^m_{T=0}(j,j')+V^m_{T=1}(j,j')\}\hat{n}^p_j\hat{n}^n_{j'} + \sum_{j}\frac{1}{2}\left\{V^m_{T=0}(j,j)\frac{2j+2}{2j+1}+V^m_{T=1}(j,j)\frac{2j}{2j+1}\right\}\hat{n}^p_j\hat{n}^n_j. \quad (28)$$

The ESPE is evaluated with this effective monopole interaction hereafter.

The proton-neutron interaction thus contributes to the ESPE of the neutron orbit j as

$$\hat{\epsilon}^{p\to n}_j = \sum_{j'}\frac{1}{2}\{\tilde{V}^m_{T=0}(j',j)+\tilde{V}^m_{T=1}(j',j)\}\hat{n}^p_{j'}, \quad (29)$$

and to the ESPE of the proton orbit j as

$$\hat{\epsilon}^{n\to p}_j = \sum_{j'}\frac{1}{2}\{\tilde{V}^m_{T=0}(j,j')+\tilde{V}^m_{T=1}(j,j')\}\hat{n}^n_{j'}, \quad (30)$$

where $\tilde{V}$'s are modified monopole matrix elements defined by

$$\tilde{V}^m_{T=0,1}(j,j') = V^m_{T=0,1}(j,j'), \quad \text{for } j\neq j', \quad (31)$$

$$\tilde{V}^m_{T=0}(j,j) = V^m_{T=0}(j,j)\frac{2j+2}{2j+1}, \quad (32)$$

and

$$\tilde{V}^m_{T=1}(j,j) = V^m_{T=1}(j,j)\frac{2j}{2j+1}. \quad (33)$$

We note that this substitution of $V^m_{T=1}(j,j)$ with $\tilde{V}^m_{T=1}(j,j)$ is only for the proton-neutron interaction, keeping Eqs. (23) and (24) unchanged. It is worth mentioning that the effective monopole interaction in Eq. (28) produces the exact energy for a closed shell, $\langle\hat{n}^p_j\rangle = 2j+1$ or $\langle\hat{n}^n_j\rangle = 2j+1$, because the equal distribution approximation turns out to be exact.

We express the valence contribution to the ESPE from Eqs. (23), (24), (26), and (29) by introducing

$$\tilde{V}^m_{pn}(j,j') = \tfrac{1}{2}\{\tilde{V}^m_{T=0}(j,j')+\tilde{V}^m_{T=1}(j,j')\}. \quad (34)$$

It is then, for the proton orbit j,

$$\hat{\epsilon}^p_j = \sum_{j'}V^m_{T=1}(j,j')\hat{n}^p_{j'} + \sum_{j'}\tilde{V}^m_{pn}(j,j')\hat{n}^n_{j'}, \quad (35)$$

and for the neutron orbit j,

$$\hat{\epsilon}^n_j = \sum_{j'}V^m_{T=1}(j,j')\hat{n}^n_{j'} + \sum_{j'}\tilde{V}^m_{pn}(j',j)\hat{n}^p_{j'}. \quad (36)$$

Note that one can use $V^m_x(j,j') = V^m_x(j',j)$ for any subscript x if that is more convenient.

We point out that, for the closed-shell-plus-one-nucleon systems, the results shown in Eqs. (35) and (36) produce the exact energy for a single proton state j,

$$\epsilon^p_j = \sum_{\mathrm{occ}\ j'_p}V^m_{T=1}(j,j'_p)(2j'_p+1) + \sum_{\mathrm{occ}\ j'_n}\tilde{V}^m_{pn}(j,j'_n)(2j'_n+1), \quad (37)$$

where the summation of j'_p or j'_n is taken for all fully occupied orbits in the valence space and the ESPEs are treated as c numbers. This is because the approximation in Eq. (27) becomes an equality relation due to the apparent equal distribution in the closed shell. Single-hole states can be treated in the same way. A similar expression is obtained for neutrons.

E. Short summary and relation to earlier work

We first summarize some properties relevant to subsequent discussions. The variation of ESPE is more relevant than the ESPE itself in many applications. The difference can be taken between different nuclei or between different states of the same nucleus. It can be expressed conveniently, based on Eqs. (35) and (36), as

$$\Delta\hat{\epsilon}^p_j = \sum_{j'}V^m_{T=1}(j,j')\Delta\hat{n}^p_{j'} + \sum_{j'}\tilde{V}^m_{pn}(j,j')\Delta\hat{n}^n_{j'} \quad (38)$$

and

$$\Delta\hat{\epsilon}^n_j = \sum_{j'}V^m_{T=1}(j,j')\Delta\hat{n}^n_{j'} + \sum_{j'}\tilde{V}^m_{pn}(j',j)\Delta\hat{n}^p_{j'}. \quad (39)$$

Here Δ refers to the difference like $\langle\Psi|\hat{\epsilon}^p_j|\Psi\rangle - \langle\Psi'|\hat{\epsilon}^p_j|\Psi'\rangle$ between two states Ψ and Ψ'.

While the occupation numbers $\hat{n}^p_j$ and $\hat{n}^n_j$ in Eqs. (35) and (36) are operators, their expectation values are relevant in many cases. Thus, although the ESPE (of an orbit) is an operator, its expectation value (with respect to some state, e.g., the ground state) is sometimes called ESPE also. The same is true for their differences in Eqs. (38) and (39). Likewise, in the filling scheme where nucleons are put into the possible lowest orbit one by one, these operators are c numbers for a given nucleus, and the ESPEs become c numbers also. We omit the hat symbols in those cases.

The coefficients in these equations are given by the monopole matrix elements and their slight modifications $\tilde{V}^m_{pn}(j,j')$; see Eqs. (31), (32), (33), and (34). In practical studies, the expression in Eq. (19) is more convenient than the definition with m-scheme states because the values can be taken directly from shell-model interactions.

We next comment on relations of the present approach to earlier ones. Based on some initial shell-model works, for instance, de-Shalit and Talmi (1963), Bansal and French (1964), and French (1966, 1969), introduced "the average two-body interaction energy [taken with a $(2J+1)(2T+1)$ weighting]," and also "another average, taken without the $(2T+1)$ weighting." Thus, Bansal and French regarded these approaches as two different schemes. The former is basically suitable for a closed shell where both proton and neutron shells are completely occupied. The averaging of all two-body matrix elements is carried out for all neutron-neutron, proton-proton, and proton-neutron pairs, and the weighting factor

$(2J+1)(2T+1)$ arises. As the $T=0$ and $T=1$ two-body matrix elements are very different in size, another parameter was introduced to account for it (Bansal and French, 1964; Zamick, 1965). The formulation of this work is also based on an averaging. But this is the averaging over all possible orientations of a given two-nucleon configuration $j \otimes j'$, and the idea is visualized in Fig. 7 with the definition in Eq. (5) and in other related equations. The derived monopole interaction is shown in Sec. III.A with Eqs. (14), (15), (16), and (17). These equations include the terms proportional to $\hat{n}_j^p \hat{n}_{j'}^n$, which may be related to Bansal-French's previously mentioned second scheme. This second scheme was further described by Bansal and French (1964) as follows: "This is the average which one encounters in an *n-p* formalism (one in which neutrons and protons are separately numbered) in those cases where the neutron is necessarily in one orbit, the proton in the other." Equations (14), (15), (16), and (17) include terms dependent on isospin operators, as illustrated in Fig. 8, which enables us to remove such a restriction of the orbits and allow protons and neutrons to be in the same orbit.

Poves and Zuker (1981) developed the scheme of Bansal and French, stating "H_{m} and H_{mT} can be thought of as generalization of the French-Bansal formulae." The weighting factors $(2J+1)(2T+1)$ are included in H_{mT} [see also Caurier *et al.* (2005)], while the isospin is not considered in H_{m}; see also Zuker (1994). The monopole interaction H_{mT} presented by Poves and Zuker (1981) produces the same energy for closed-shell states as the present approach. Thus, the result of Poves and Zuker (1981) and the relevant result of the present approach are obtained, most likely, by different procedures with consistent outcomes. This consistency may be supported by the fact that the monopole interaction can be composed of the number and isospin operators of individual orbits, and closed shells can give sufficient constraints on the values of their parameters. The use of the monopole Hamiltonian of Poves and Zuker (1981) has been developed and applied to properties of closed-shell nuclei and their neighbors with ± one particle, producing precisely the global systematics of nuclear masses (Zuker, 1994, 2005; Duflo and Zuker, 1995, 1999; Caurier *et al.*, 2005). A review of them was given by Caurier *et al.* (2005).

One thus sees that the two approaches mentioned by Bansal and French are basically two facets of one common monopole interaction derived from the orientation averaging in the present scheme, keeping isospin properties. In this way, we can settle a long-standing question on the definition and uniqueness of the monopole interaction, finding that basically all of those arguments are along the same lines. The additional $\tau\tau$ term of Eq. (14) is of interest.

Additional interest lies in the variational approach with monopole interaction in open-shell nuclei discussed by Yazaki (1977).

F. Equivalence to ESPE as defined by Baranger

We discuss the definition of the ESPE by Baranger (1970). The ESPE of the orbit j on top of the eigenstate $|0\rangle$ is considered by referring to the nth (Nth) eigenstate, $|n\rangle$ ($|N\rangle$), of the nucleus with one more (less) particle of interest. The ESPE is then expressed as

$$\epsilon_j = \sum_n (E_n - E_0) S_n^+ + \sum_N (E_0 - E_N) S_N^-, \tag{40}$$

where E_0 is the energy of the state $|0\rangle$, and E_n (E_N) denotes the energy of the state $|n\rangle$ ($|N\rangle$). Here S_n^+ (S_N^-) stands for spectroscopic factors $|\langle n|a_q^\dagger|0\rangle|^2$ ($|\langle N|a_q|0\rangle|^2$), with q being a magnetic substate of the orbit j. Equation (40) implies that the ESPE is composed not only of energy gains in going from $|0\rangle$ to $|n\rangle$ weighted by the spectroscopic factors but also of minus times energy losses from $|0\rangle$ to $|N\rangle$ weighted similarly. Note that the latter contributes if the orbit j is occupied in $|0\rangle$. We discuss now the relation between this definition and the one discussed previously. Note that the state $|0\rangle$ was assumed to be the ground state of a double-closed-shell nucleus by Baranger (1970), but we can generalize it to a 0^+ state. However, if its spin parity is not 0^+, Eq. (40) does not represent the ESPE.

Equation (40) can be rewritten as

$$\epsilon_j = \langle 0|a_q(H - E_0)a_q^\dagger|0\rangle + \langle 0|a_q^\dagger(H - E_0)a_q|0\rangle, \tag{41}$$

where H is the Hamiltonian. This is identical to Eq. (6) of Baranger (1970) even though they look different. After algebraic processing, we come to

$$\epsilon_j = \epsilon_j^0 + \sum_{\beta,\delta} v_{q\beta q\delta}\langle 0|a_\beta^\dagger a_\delta|0\rangle, \tag{42}$$

where ϵ_j^0 is defined in Eq. (1) and $v_{q\beta q\delta}$ denotes an antisymmetrized matrix element of the two-body interaction.

Because $|0\rangle$ is a 0^+ state, the following relations hold in Eq. (42) for the magnetic quantum number $m_\beta = m_\delta$, and for the angular momentum $j_\beta = j_\delta$ denoted by j'. We assume that the states β and δ are the same for simplicity, while a more general treatment is possible. We note that this assumption is valid with two HO major shells or in other similar cases. The matrix element $\langle 0|a_\beta^\dagger a_\delta|0\rangle$ can be replaced with $\langle 0|\hat{n}_{j'}|0\rangle/(2j'+1)$, which is independent of m_β. Here $\hat{n}_{j'}$ is the number operator of the orbit j'. Although ϵ_j in Eq. (40) is independent of q, we sum $v_{q\beta q\beta}$ over q, and the sum can be expressed as the monopole matrix element $V^m(j,j')$ multiplied by the number of relevant antisymmetrized states of j and j'. Note that the difference in this number between $j=j'$ and $j \neq j'$ cases is incorporated. We finally obtain the following unified expression:

$$\epsilon_j = \epsilon_j^0 + \sum_{j'} V_{j,j'}^m \langle 0|\hat{n}_{j'}|0\rangle. \tag{43}$$

This is the ESPE discussed so far with the substitution of $\hat{n}_{j'}^p$ and $\hat{n}_{j'}^n$ in Eqs. (35) and (36) by their expectation values with respect to the eigenstate $|0\rangle$. Namely, the ESPE formulation by Baranger (1970) is included in the present monopole formulation as a specific case, with $|0\rangle$ being a 0^+ state, while the present one is applicable to the other states as well. We mention that the present approach has a modification due to the isospin [see Eqs. (32) and (33)], and how to include this in the previous discussion is of interest.

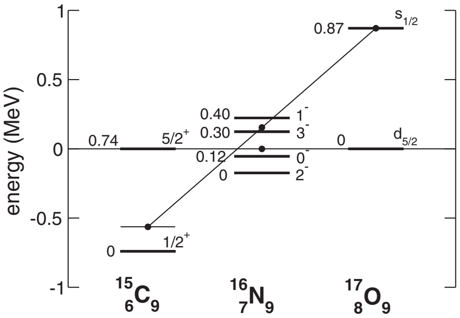

FIG. 9. Experimental energy levels of $N = 9$ isotones, some of which are regarded as neutron $2s_{1/2}$ and $1d_{5/2}$ single-particle energies. See the text. Adapted from Talmi and Unna, 1960.

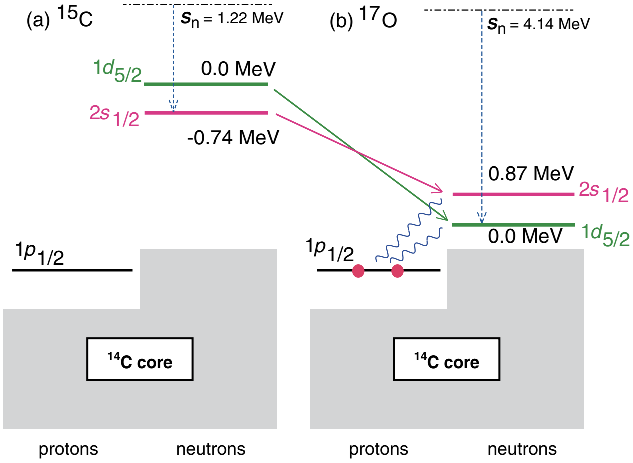

FIG. 10. (a) Schematic picture of shell structure on top of the ^{14}C core. (b) Two more protons (red solid circles) are added into the $1p_{1/2}$ orbit. Experimental levels are identified as single-particle states: green level for $1d_{5/2}$ and pink level for $2s_{1/2}$. Numbers near the levels are energies relative to $1d_{5/2}$. The wavy lines imply proton-neutron interactions. Solid arrows indicate the changes of SPEs. The dash-dotted line denotes the neutron threshold, and downward dashed arrows indicate one-neutron separation energy (S_n).

We can thus present a unified formulation on the monopole properties, starting from the natural construction of the monopole interaction. Duguet *et al.* (2015) stated in footnote 1, “In the traditional shell model, ESPE usually refers to single-particle energies obtained by averaging over the monopole part of the Hamiltonian on the basis of a naive filling…. The latter denotes an approximate version of the full Baranger-French definition….” This remark may be applicable to some earlier works using the filling scheme for defining the ESPE, but it is not relevant to the present formulation.

The ESPE, as the expectation value of the 0^+ ground state [see the texts following Eq. (39)], can be extracted from experiment if all relevant spectroscopic factors in Eq. (40) are obtained at great precision. Because one-nucleon addition and removal experiments are required, this is a difficult task in general, except for cases where the spectroscopic factors are negligible in either direction, e.g., at a closed shell. Despite this experimental challenge, the ESPE is useful for understanding and explaining phenomena and mechanisms.

G. Illustration by an example

We present an example of the change of ESPEs of the $N = 9$ isotones, as shown in Fig. 9. This figure is taken from Fig. 2 of Talmi and Unna (1960), one of the earliest related papers. We discuss here how the changes shown in Fig. 9 can be described within the framework presented in Sec. III.D. The discussions are somewhat detailed because this is the first actual example.

We assume the ^{14}C core with $Z = 6$ and $N = 8$. Figure 10 illustrates the shell structure on top of this ^{14}C core. The levels shown in Fig. 10 are taken from experimental data (ENSDF, 2017), by assuming that the observed lowest levels are of a single-particle nature, and are almost the same as the corresponding ones in Fig. 9. Figure 10(a) indicates somewhat schematically neutron $2s_{1/2}$ and $1d_{5/2}$ orbits on top of the ^{14}C core. Note that in Fig. 10(a) the $2s_{1/2}$ orbit is 0.74 MeV below $1d_{5/2}$.

We then add protons into the $1p_{1/2}$ orbit, as shown in Fig. 10(b). The proton $1p_{1/2}$ orbit is fully occupied or closed now. The ESPEs of neutron $2s_{1/2}$ and $1d_{5/2}$ orbits are both lowered, but their order is reversed due to protons in the $1p_{1/2}$ orbit, following Eq. (36), with $j' = 1p_{1/2}$ and $j = 2s_{1/2}$ or $1d_{5/2}$. The ESPEs are treated here as c numbers because the wave function of the other nucleons is fixed, as mentioned in Sec. III.D. The difference between the ESPEs can be written as

$$\begin{aligned}
&\epsilon^n_{2s_{1/2}}(^{17}\mathrm{O}) - \epsilon^n_{1d_{5/2}}(^{17}\mathrm{O}) \\
&\quad = \epsilon^n_{2s_{1/2}}(^{15}\mathrm{C}) - \epsilon^n_{1d_{5/2}}(^{15}\mathrm{C}) \\
&\qquad + \{V^m_{pn}(1p_{1/2}, 2s_{1/2}) - V^m_{pn}(1p_{1/2}, 1d_{5/2})\} \times 2. \qquad (44)
\end{aligned}$$

The proton sector of the Hamiltonian produces the common effect between the $J^\pi = 1/2^+$ and $J^\pi = 5/2^+$ states. Thus, this difference between ESPEs corresponds to the difference of experimental levels under the assumption that these states are of a single-particle nature (which is reexamined in Sec. IV.F especially in Fig. 34), and the monopole matrix elements satisfying

$$\begin{aligned}
&V^m_{pn}(1p_{1/2}, 2s_{1/2}) - V^m_{pn}(1p_{1/2}, 1d_{5/2}) \\
&\quad = (0.87 + 0.74)/2 = 0.805 \text{ MeV} \qquad (45)
\end{aligned}$$

explain the change in Fig. 10. This result indicates that $V^m_{pn}(1p_{1/2}, 1d_{5/2})$ is more attractive by ~0.8 MeV than $V^m_{pn}(1p_{1/2}, 2s_{1/2})$. Thus, what actually occurs is a more rapid lowering of the neutron $1d_{5/2}$ orbit than of the neutron $2s_{1/2}$ orbit, as protons fill the $1p_{1/2}$ orbit. This can be explained as a consequence of important and general features of the monopole interactions of nuclear forces, as discussed extensively in Sec. IV.

If the energy is measured relative to the neutron $1d_{5/2}$ orbit, the monopole-matrix-element difference in Eq. (45) pushes up the neutron $2s_{1/2}$ orbit from ^{15}C to ^{17}O. We describe the approach by Talmi and Unna (1960) with this convention such that the energy is measured from the neutron $1d_{5/2}$ ESPE with the filling scheme. The energy levels in Fig. 10 can be viewed in this convention, including ^{16}N ($Z = 7$ and $N = 9$) with one proton in the $1p_{1/2}$ orbit. This proton is coupled with a neutron in either $2s_{1/2}$ or $1d_{5/2}$. The former coupling yields $J^\pi = 0^-$ and 1^- states, while the latter yields $J^\pi = 2^-$ and 3^- states. In this simple configuration, the proton-neutron interaction $\hat{v}_{pn}$ shifts the energies of these states by

$$\frac{1}{2}\sum_{T=0,1}\langle j, j'; J, T|\hat{v}_{pn}|j, j'; J, T\rangle. \tag{46}$$

The $(2J+1)$-weighted average of the quantities in Eq. (46) is the corresponding monopole matrix element because of Eqs. (19) and (31), as well as Eq. (S2) of the Supplemental Material (364). Thus, those averages can be discussed as the ESPEs driven by the monopole interaction, and the aforementioned convention can be adopted. As the change from ^{15}C to ^{17}O is then twice the monopole-matrix-element difference due to two additional protons, the middle point of the line connecting the states of the same spin parity of ^{15}C, and ^{17}O represents the corresponding monopole quantity. Thus, if the present scheme works ideally, the $1/2^+$ levels and the relevant average quantity of ^{16}N should be on a straight line. Talmi and Unna (1960) did this analysis in a slightly different way: they took the observed energy levels of ^{17}O and the weighted averages for the observed levels of ^{16}N and extrapolated to ^{15}C. The extrapolated value appeared rather close to the observed one, implying the validity of this picture, which is revisited in Sec. IV.F.

Talmi and Unna discussed another case with ^{11}Be-^{12}B-^{13}C ($N = 7$ isotones with $Z = 4$, 5, and 6) (Talmi and Unna, 1960). Although the $1/2^+$ levels change almost linearly as a function of N, the mechanism is different from the previously discussed $N = 9$ isotone case. Since protons occupy the $1p_{3/2}$ orbit now, one has to take into account the coupling of two protons. It was taken to be $J = 0$ [see Eq. (1) in Talmi and Unna (1960)], which enables us to connect the change of the structure to the monopole interaction because multipole interactions are completely suppressed. Note that the terminology monopole interaction was not used then, but the same quantity was used. This restriction to the $J = 0$ coupling, however, may not be appropriate because the deformation of the shape is crucial and, simultaneously, configuration mixings occur even between the $1p_{3/2}$ and $1p_{1/2}$ proton orbits. The single-particle nature is broken also on the neutron side due to configuration mixing between the $2s_{1/2}$ and $1d_{5/2}$ orbits. Thus, the $N = 7$ isotones may not be a good example of the change of single-particle energies. In fact, the magnitude of the change is twice that of the $N = 9$ isotone case, which may be indicative of dominant additional effects.

An example of the ESPE change due to the $T = 1$ interaction is given in Sec. S4 of the Supplemental Material (364).

IV. SHELL EVOLUTION, MONOPOLE INTERACTION, AND NUCLEAR FORCES

The ESPE is shown to be varied according to the relations in Eqs. (38) and (39). Since it depends linearly on the proton or neutron number operators of a particular orbit j, denoted as $\hat{n}_j^p$ and $\hat{n}_j^n$, respectively, the ESPE can be changed to a large extent if the occupation number of a given orbit becomes large. Further, this can result in a substantial change of the shell structure, called shell evolution. Thus, the shell evolution can occur, for instance, as a function of N along an isotopic chain. We discuss here some basic points of the shell evolution in close relation to nuclear forces.

Note that the multipole interaction defined in Sec. III.B produces a variety of correlations, for instance, quadrupole deformation, and that the final structure is determined jointly by the monopole and multipole interactions, as is done automatically when the Hamiltonian is diagonalized. Although there is no *a priori* separation of effects of the monopole interaction from those of the multipole interaction, the monopole effects, particularly the shell evolution, can be made visible in many cases. We focus here on such effects of the monopole interactions due to various constituents of the NN interaction, such as central, tensor, and two-body spin-orbit.

A. Contributions from the central force

The central-force component of the nuclear force is the main driving force of the formation of the nuclear structure.

Let us start with an extreme case. If the effective nucleon-nucleon (NN) interaction $\hat{v}$ is a central force with infinite range and no dependence on spin, the values of the monopole matrix elements $V^m_{T=1}(j, j')$ and $V^m_{pn}(j, j')$, being constants, become independent of j and j'. If this $\hat{v}$ is attractive, $V^m_{T=1}(j, j')$ and $V^m_{pn}(j, j')$ take separate constant negative values. This implies, for instance, that if more neutrons occupy the orbit j', all proton orbits j become more bound to the same extent. In other words, the proton shell structure is conserved but becomes more deeply bound.

On the other hand, if $\hat{v}$ is given by a δ function with a certain attractive strength parameter, the values of $V^m_{T=1}(j, j')$ and $V^m_{pn}(j, j')$ become sensitive to the overlap between the wave function of the orbit j and that of the orbit j'. This implies that if more neutrons occupy the orbit j', proton ESPE for the orbit j in Eq. (38) will become more bound, but the amount of the change is not uniform. In other words, the pattern of the proton single-particle orbits may change while they all become more bound as a whole.

The actual situation is certainly somewhere in between. We show here how monopole matrix elements look for a central Gaussian interaction given by

$$v_c = \sum_{S,T} f_{S,T} P_{S,T} \exp[-(r/\mu)^2], \tag{47}$$

where $S(T)$ indicates spin (isospin), P denotes the projection operator onto the channels (S, T) with strength f, and r and μ are the internucleon distance and Gaussian parameter, respectively. We fix here all f parameters to a common value of $+166$ MeV in order to see the effects of the four terms on the right-hand side. The $\mu = 1$ fm value is used, as we also discuss in Sec. IV.C. Note that we use this v_c value extensively hereafter with realistic values of parameters such as $f_{1,0} = f_{0,0} = -166$ MeV (i.e., the same magnitude with the opposite

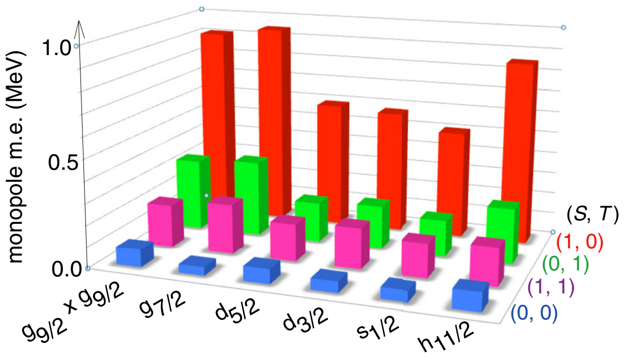

FIG. 11. Monopole matrix elements of central Gaussian interactions of Eq. (47) for all (S,T) channels with an equal strength parameter (i.e., $+166$ MeV; see the text). One of the orbits is $1g_{9/2}$, and the other is shown.

sign as the previous value), and $f_{0,1} = 0.6 f_{1,0}$ and $f_{1,1} = -0.8 f_{1,0}$. Such a v_c gives basic features of an effective NN interaction of the shell-model calculation called V_{MU} (Otsuka, Suzuki, Honma *et al.*, 2010).

Figure 11 shows monopole matrix elements thus obtained. The harmonic oscillator wave functions are used as single-particle wave functions hereafter. We take $A = 100$ in Fig. 11.

Figure 11 indicates that the $(S = 1,\ T = 0)$ channel produces major contributions apart from the actual $f_{S,T}$ values. Furthermore, as previously mentioned, the actual value of $f_{S=1,T=0}$ appears to be the largest among the four (S,T) channels [e.g., in the V_{MU} (Otsuka, Suzuki, Honma *et al.*, 2010)], and the dominance of the $(S = 1,\ T = 0)$ channel becomes enhanced after considering the actual $f_{S,T}$ values.

Within the $(S = 1,\ T = 0)$ channel, Fig. 11 demonstrates that the couplings between orbits with $n = 1$ (i.e., no node in the radial wave function), like $1g_{9/2}$-$1g_{9/2,7/2}$ or $1g_{9/2}$-$1h_{11/2}$, are stronger than the others. This can be understood in terms of the larger overlap between their radial wave functions than those in the other categories in Fig. 11.

We show similar histograms for the δ-function interaction in Fig. 12. One finds rather good overall similarity to Fig. 11. As the monopole matrix elements vanish for the $(S = 1,\ T = 1)$ or $(S = 0,\ T = 0)$ channel, they are not shown in Fig. 12. This is a consequence of the Pauli principle that forbids two nucleons at the same place for $S = 0$, $T = 0$ or $S = 1$, $T = 1$.

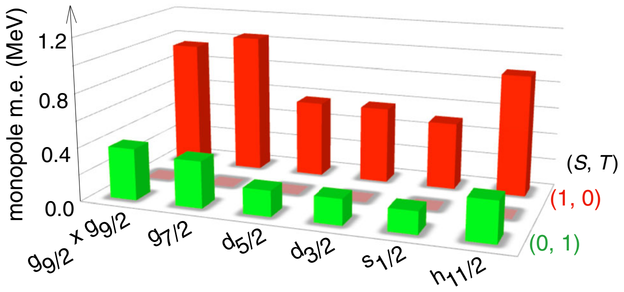

FIG. 12. Monopole matrix elements of delta interactions for (S,T) channels. See the caption of Fig. 11.

It is now of interest to survey the overall dependence of the monopole matrix element on the nodal structure of the radial wave function. Figure 13 shows monopole matrix elements in the $(S = 1,\ T = 0)$ channel for the Gaussian and δ-function interactions. In Fig. 13, various pairs of orbits are taken for the valence shells around (a) $A = 100$ and (b) $A = 70$, with their labels abbreviated as, for example, g7 for $1g_{7/2}$. The strength of the δ-function interaction is adjusted so that the monopole matrix element becomes equal to that given by the Gaussian interaction for (a) the g9-g7 pair and (b) the f7-f5 pair.

The orbital pairs are classified into categories according to the difference of the number of the nodes in their radial wave functions, as denoted by Δn in Fig. 13. The monopole matrix elements are generally large when the radial wave functions have the same number of the nodes (i.e., $\Delta n = 0$). The monopole matrix elements become smaller as Δn increases, while the difference between the two categories $\Delta n = 1$ and

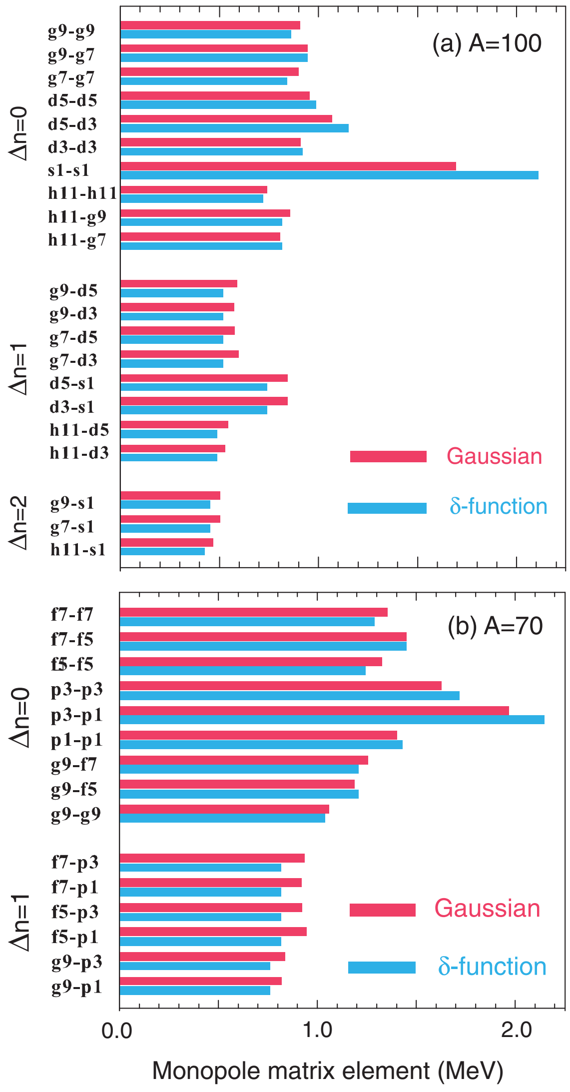

FIG. 13. Monopole matrix elements of central Gaussian and δ interactions for the $(S = 1,\ T = 0)$ channel. The opposite sign should be taken for actual values. The orbit labeling is abbreviated as g9 for $1g_{9/2}$, etc. The orbits are from the valence shell for (a) $A = 100$ and (b) $A = 70$.

$\Delta n = 2$ is much smaller. On the other hand, the monopole matrix element varies within the $\Delta n = 0$ category. The large value of the $s1$-$s1$ in Fig. 13(a) is exceptional. Among the others with $\Delta n = 0$ in Fig. 13(a), stronger coupling can be found between the following orbits:

$$j_> = \ell + 1/2 \quad \text{and} \quad j_< = \ell - 1/2, \tag{48}$$

where ℓ stands for the orbital angular momentum and $1/2$ represents the spin. In other words, $j_>$ and $j_<$ are spin-orbit partners having the same radial wave functions in the harmonic oscillator scheme, and therefore the central force, both the Gaussian and the δ-function interactions, produces stronger monopole interactions between them. This feature is seen in the cases of (i) g9 and g7, (ii) d5 and d3, (iii) f7 and f5, and (iv) p3 and p1 in Fig. 13. This type of enhanced coupling becomes weaker with the Gaussian interaction than with the δ-function interaction.

We emphasize that the monopole matrix elements of the central force, as modeled by the Gaussian interaction in Eq. (47), vary considerably, and they can produce a sizable shell evolution depending on the occupation pattern over relevant single-particle orbits. Concrete examples are shown in Secs. IV.C and IV.D.

Regarding the dependence on the mass number A, the monopole matrix elements of $A = 100$ in Fig. 13(a) is, as a whole, about $2/3$ of those of $A = 70$ in Fig. 13(b). This feature can be expressed by a $1/A$ dependence in a rough approximation if wished. This approximate scaling law appears to be reasonable because the probability of finding the partner of a pair of interacting nucleons inside the interaction range is inversely proportional to the nuclear volume, as long as the density saturation holds. Note that this overall trend is seen in experimentally extracted data, while other A dependences can be found locally in certain groups; see Fig. 8 in Sorlin and Porquet (2008).

Stronger couplings between particular orbits are a natural idea and were, in fact, discussed in earlier works, for instance, by Federman and Pittel, (1977, 1979), Federman, Pittel, and Campos (1979), Federman, Pittel, and Etchegoyen (1984), and Pittel *et al.* (1993). It has been argued by Federman and Pittel (1977) that the proton-neutron central force in the ${}^3S_1$ channel, where S stands for the s wave ($L = 0$) with the spin triplet and the relative orbital (total) angular momentum $L = 0$ ($J = 1$), gives rise to a strong attraction between two orbitals (n_P, l_P, j_P) and (n_N, l_N, j_N) when the relations $n_P = n_N$ and $l_P \approx l_N$ are satisfied because of a large spatial overlap (de-Shalit and Goldhaber, 1953). It certainly contributes to the present ($S = 1$, $T = 0$) channel. Figure 13(a) suggests that the monopole matrix element $V^m_{T=0}(1g_{7/2}, 1g_{9/2})$ is about 0.3 MeV more attractive than $V^m_{T=0}(2d_{5/2}, 1g_{9/2})$ with the previously mentioned realistic sign of the parameter. Equation (39) combined with Eqs. (31) and (34) indicates that the present Gaussian central force lowers the ESPE of the neutron $1g_{7/2}$ orbit relative to the $2d_{5/2}$ orbit by $\sim 1/2 \times 0.3 \times 10 = 1.5$ MeV, in going from $Z = 40$ to $Z = 50$. Here we assume that the $Z = 40$ and $N = 50$ closed shells are kept, that the neutron $1g_{7/2}$ and $2d_{5/2}$ orbits are on top of this closed shell, and that an additional ten protons occupy the $1g_{9/2}$ orbit. This lowering is quite sizable but will be shown to be about half of what has been known experimentally, which hints that the central force is responsible for only part of the story. Smirnova *et al.* (2004) compared δ-function and G-matrix interactions. The former is a central force, but the latter contains other components. The reported difference is therefore consistent with the present observation on the deficiency of the central force. Relevant further studies were reported by Umeya and Muto (2004, 2006).

We come back here to the limit of the long-range interaction but include dependences on the spin and isospin (Otsuka *et al.*, 2001). If there is no spin dependence, an infinite-range interaction gives a constant shift, as previously discussed. Now take a spin-isospin interaction such as

$$v_{\tau\tau\sigma\sigma} = \vec{\tau} \cdot \vec{\tau}\, \vec{\sigma} \cdot \vec{\sigma} f(r), \tag{49}$$

where $f(r)$ represents the dependence on the relative distance r, the dots imply scalar products, and $\vec{\sigma}$ ($\vec{\tau}$) refers to spin (isospin) operators.

The matrix element of the term $\vec{\tau} \cdot \vec{\tau}$ is trivial, being $-3/4$ and $1/4$ for $T = 0$ and 1, respectively. The monopole matrix elements of this interaction with $f(r) \equiv 1$ show an interesting analytic property, and we discuss it now. We consider antisymmetric states in Eq. (3) [or Eq. (S17) of the Supplemental Material (364)], and we consider symmetric states in Eq. (S3) or (S4) of the Supplemental Material (364). The monopole matrix element consists of direct and exchange contributions. The direct contribution from the $\vec{\sigma} \cdot \vec{\sigma}$ term is

$$\sum_{m,m'} (j, m|\sigma_z|j, m)(j', m'|\sigma_z|j', m') = 0, \tag{50}$$

where σ_z stands for the z component of $\vec{\sigma}$ and $\sum_m (j, m|\sigma_z|j, m) = 0$ is used. On the other hand, the exchange contribution is expressed as

$$\begin{aligned} \mp \sum_{m,m'} \{ &(1/2)\{(j, m|\sigma_+|j', m')(j', m'|\sigma_-|j, m) \\ &+ (j, m|\sigma_-|j', m')(j', m'|\sigma_+|j, m)\} \\ &+ (j, m|\sigma_z|j', m')(j', m'|\sigma_z|j, m)\}, \end{aligned} \tag{51}$$

where σ_+ and σ_- stand for the raising or lowering operator of $\vec{\sigma}$, and the overall sign $\mp$ corresponds to the antisymmetric and symmetric states, respectively. Thus, direct terms do not contribute, and only exchange contributions remain. We point out that for interactions without the $\vec{\sigma} \cdot \vec{\sigma}$ term, the situation is very different as the direct term is the major source of the monopole interaction. In order to have finite values in Eq. (51), j and j' must have the same ℓ, implying that j and j' are either $j_>$ or $j_<$ for the same ℓ. After some algebra of angular momentum, the final results are tabulated in Table I. The $j_>$-$j_<$ coupling appears to be about 2 times stronger than the $j_>$-$j_>$ or $j_<$-$j_<$ couplings. This is precisely due to larger matrix elements of spin-flip transitions, like $(j_>|\vec{\sigma}|j_<)$ or $(j_<|\vec{\sigma}|j_>)$, than spin-nonflip transitions like $(j_>|\vec{\sigma}|j_>)$ or $(j_<|\vec{\sigma}|j_<)$ (Otsuka *et al.*, 2001). The same mathematical feature applies to the isospin matrix elements, enhancing charge exchange processes like the one shown in Fig. 14(d).

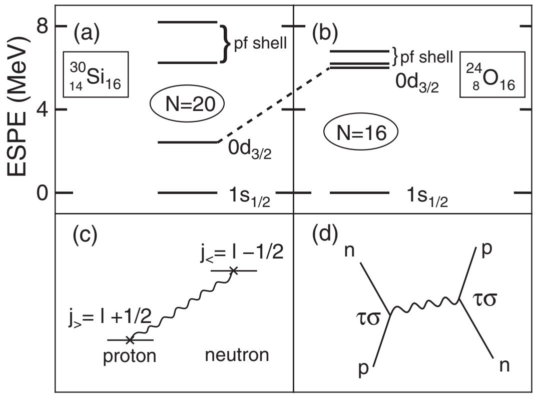

FIG. 14. Neutron ESPEs for (a) ^{30}Si and (b) ^{24}O, relative to the $2s_{1/2}$ (shown as $1s_{1/2}$) orbit. The dotted line connecting (a) and (b) is drawn to indicate the change of the $1d_{3/2}$ (shown as $0d_{3/2}$) level. (c) The major interaction producing the basic change between (a) and (b). (d) The process relevant to the interaction in (c). From Otsuka *et al.*, 2001.

The most important outcome of these features is the strong proton-neutron coupling between $j_>$ or $j_<$ with the same ℓ, or between $\ell + 1/2$ and $\ell - 1/2$; see Fig. 14(c).

A concrete example is shown in Figs. 14(a) and 14(b). We assume here the simple filling configuration that the last six protons in ^{30}Si are in the $1d_{5/2}$ (shown as $0d_{5/2}$) orbit in Fig. 14(a). On the other hand, ^{24}O has no proton in the $1d_{5/2}$ orbit and shows a large gap between neutron $1d_{3/2}$ and $2s_{1/2}$ orbits, consistent with experiment (Hoffman *et al.*, 2008; Kanungo *et al.*, 2009).

The monopole matrix element of the $\tau\tau\sigma\sigma$ interaction with $f(r) \equiv 1$ vanishes for any pair involving an $s_{1/2}$ orbit. Thus, these last six protons in ^{30}Si lower the ESPE of the neutron $1d_{3/2}$ orbit relative to the $2s_{1/2}$ orbit through the monopole matrix element

$$V^m_{pn}(1d_{5/2}, 1d_{3/2}) = -1/\{4(2 \times 2 + 1)\}, \tag{52}$$

obtained from Table I, following Eq. (34). Although not shown in Fig. 14, the ESPE of the neutron $1d_{5/2}$ orbit is lowered by about half of the change of the neutron $1d_{3/2}$ ESPE, as can be seen in Table I with $\ell \gg 1$. Thus, while the $\tau\tau\sigma\sigma$ interaction can change the spin-orbit splitting, both spin-orbit partners are shifted in the same direction but in different amounts.

This argument on a more attractive monopole matrix element between $\ell + 1/2$ and $\ell - 1/2$ orbits can be extended, with certain modifications, to finite-range and zero-range central interactions, as we have seen numerically in Fig. 13. We note that in the case of the zero-range δ-function central interaction, the total spin of two interacting nucleons is restricted to $S = 0$ for $T = 1$ and $S = 1$ for $T = 0$, and this induces some spin-spin effects even for a simple δ-function interaction without explicit spin dependence. We also point out that, within a HO major shell, the coupling between orbits with ℓ and ℓ' with $\ell \neq \ell'$ is not enhanced by central forces, as can be understood from Fig. 14(d) and as can be confirmed numerically from Fig. 13. We will return to these features after discussing the tensor-force effect.

TABLE I. Monopole matrix elements of the $\tau\tau\sigma\sigma$ interaction with $f(r) \equiv 1$. Adapted from Table 1 of Otsuka, 2002.

j_1	j_2	$T = 0$	$T = 1$
$\ell + \frac{1}{2}$	$\ell + \frac{1}{2}$	$-3/16(2\ell + 1)$	$-(2\ell + 3)/16(2\ell + 1)^2$
$\ell + \frac{1}{2}$	$\ell - \frac{1}{2}$	$-3/8(2\ell + 1)$	$-1/8(2\ell + 1)$
$\ell - \frac{1}{2}$	$\ell - \frac{1}{2}$	$-3(2\ell - 1)/16(2\ell + 1)^2$	$-1/16(2\ell + 1)$

B. Shell evolution due to the tensor force

1. Tensor force

We now study the shell evolution due to another major component of the nuclear force, the tensor force. Yukawa proposed the meson-exchange process as the origin of the nuclear forces (Yukawa, 1935). Although this was on the exchange of a scalar meson and is not directly related to the tensor force, the meson-exchange theory was developed further, and Bethe demonstrated that the tensor force is formulated with the coupling due to another kind of meson [i.e., referred to as the π meson (or pion) presently], with explicit reference to the tensor force and its effect on the deuteron property (Bethe, 1940a, 1940b). We can thus identify the tensor force with its unique features as one of the most important and visible manifestations of the meson-exchange process initiated by Yukawa.

We start our discussion with the one-π exchange potential between the ith and jth nucleons,

$$V_\pi = f(\vec{\tau}_i \cdot \vec{\tau}_j)(\vec{\sigma}_i \cdot \nabla)(\vec{\sigma}_j \cdot \nabla)\frac{e^{-m_\pi r}}{r}, \tag{53}$$

where $\vec{\tau}_i$ and $\vec{\sigma}_i$ indicate, respectively, the isospin and spin operators of the ith nucleon, $\vec{r}$ denotes the relative displacement between these two nucleons with $r = |\vec{r}|$, and ∇ stands for the derivative by $\vec{r}$. Here f and m_π are the coupling constant and the π-meson mass, respectively. Equation (53) is rewritten as

$$V_\pi = \frac{f m_\pi^2}{3}(\vec{\tau}_i \cdot \vec{\tau}_j)\left\{(\vec{\sigma}_i \cdot \vec{\sigma}_j) + S_{ij}\left\{1 + \frac{3}{m_\pi r} + \frac{3}{(m_\pi r)^2}\right\}\right\}\frac{e^{-m_\pi r}}{r}, \tag{54}$$

with

$$S_{ij} = 3(\vec{\sigma}_i \cdot \vec{r})(\vec{\sigma}_j \cdot \vec{r})/r^2 - (\vec{\sigma}_i \cdot \vec{\sigma}_j). \tag{55}$$

Here an additional δ-function term is omitted in Eq. (54) as usual (because there are other processes at short distances). The first term within the outer curly brackets on the right-hand side of Eq. (54) produces a central force and is not considered hereafter. The second term within this set of brackets generates the tensor force from the one-π exchange process.

As an example of the radial dependence of actual tensor potentials, Fig. 15 shows the triplet-even (TE) potential due to the tensor potentials in some approaches; see (Otsuka *et al.* (2005) for details. Except for the π-meson-exchange case (no ρ meson), the TE potentials exhibit rather similar behavior

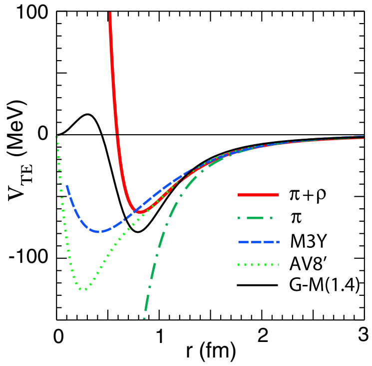

FIG. 15. Triplet-even potential due to the tensor force for various interaction models. Adapted from Otsuka *et al.*, 2005.

outside ∼0.6 fm. While differences arise inside, the relative-motion wave functions of two interacting nucleons are suppressed there because of forbidden coupling between S-wave bra and ket states.

The tensor force has been known for a long time in connection to the one-π exchange potential stated here, and its effects were studied extensively from many angles. Early studies in connection to the nuclear structure include an extraction of the tensor-force component in the empirical NN interaction by Schiffer and True (1976), a derivation of microscopic effective NN interaction (i.e., so-called G-matrix interaction) including second-order effects of the tensor force by Kuo and Brown (1966), a calculation of magnetic moments that also includes second-order tensor-force contributions by Shimizu, Ichimura, and Arima (1974) and Towner (1987), a review on its effects on light nuclei (Fayache, Zamick, and Castel, 1997).

Besides such effects, the tensor force produces another effect on the shell structure in its lowest order or by the one-π exchange process. This effect must be contained in the numerical results, but its simple, robust, and general features had not been mentioned or discussed until the work done by Otsuka *et al.* (2005), where the change of the shell structure, i.e., the shell evolution, due to the tensor force was presented for the first time.

We present the monopole interaction of the tensor force first, in order to clarify such tensor-force-driven shell evolution. Because the S operator in Eq. (55) between nucleons 1 and 2 can be rewritten as

$$S_{12} = \sqrt{24\pi}[[\vec{\sigma}_1 \times \vec{\sigma}_2]^{(2)} \times Y^{(2)}(\theta, \phi)]^{(0)}, \tag{56}$$

where $[\times]^{(K)}$ indicates the coupling of two operators in the brackets to an angular momentum (or rank) K, and where Y denotes the spherical harmonics of the given rank for the Euler angles θ and ϕ of the relative coordinate. The tensor force can then be rewritten in general as

$$V^{\text{ten}} = (\vec{\tau}_1 \cdot \vec{\tau}_2)([\vec{\sigma}_1 \times \vec{\sigma}_2]^{(2)} \cdot Y^{(2)}(\theta, \phi))f^{\text{ten}}(r), \tag{57}$$

where $f^{\text{ten}}(r)$ is an appropriate function of the relative distance r. Note that the scalar product is taken instead of $[\times]^{(K)}$. Equation (57) is equivalent to the usual expression containing the S_{12} function. Because the spins $\vec{\sigma}_1$ and $\vec{\sigma}_2$ are dipole operators and are coupled to rank 2, the total spin S (magnitude of $\vec{S} = \vec{s}_1 + \vec{s}_2$) of two interacting nucleons must be $S = 1$. If both of the bra and ket states of V^{ten} have $L = 0$, with L being the relative orbital angular momentum, their matrix element vanishes because of the $Y^{(2)}$ coupling. The crucial roles of these properties are shown in the following.

Besides the π-meson exchange, the ρ meson contributes to the tensor force. In the following, we use the $\pi + \rho$ meson-exchange potential with the coupling constants taken from Osterfeld (1992). The function $f^{\text{ten}}(r)$ therefore corresponds to the sum of these exchange processes. The magnitude of the tensor-force effects to be discussed becomes about 3/4 of the results by the one-π exchange only. The basic physics will not be changed. We will compare the $\pi + \rho$ meson results with those by modern theories of nuclear forces.

2. Tensor force and two-nucleon system

Having these setups, we first recall the basic properties of the tensor force by taking a two-nucleon system. From Sec. IV.B.1, we know $S = 1$ for two nucleons interacting through the tensor force. We therefore assign $s_z = 1/2$ for each nucleon, taking the z axis in the direction of the spin.

Figure 16 displays this system schematically in two different situations. The spins are shown by arrows pointing upward and are placed where two nucleons are placed at rest. In other words, two nucleons are displaced (a) in the direction of the spin or (b) in the perpendicular direction. This is certainly a modeling of the actual situation, of which the wave function of the relative motion is shown schematically by the yellow shaded areas in Fig. 16.

We now consider the effect of the tensor force in these two cases by denoting the value of the operator in Eq. (55) by $\mathcal{S}_{ij}$. In the case of Fig. 16(a), we obtain

$$(\vec{\sigma}_i \cdot \vec{r})/r \times (\vec{\sigma}_j \cdot \vec{r})/r = \tfrac{1}{2} \times \tfrac{1}{2}, \tag{58}$$

while this quantity vanishes for Fig. 16(b) because of the orthogonality between $\vec{\sigma}$ and $\vec{r}$. Because of $S = 1$,

$$(\vec{\sigma}_i \cdot \vec{\sigma}_j) = \tfrac{1}{4} \tag{59}$$

holds. Combining these, we obtain

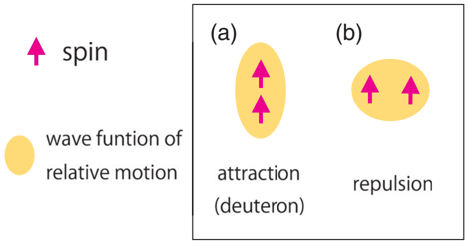

FIG. 16. Intuitive picture of the tensor force acting on two nucleons.

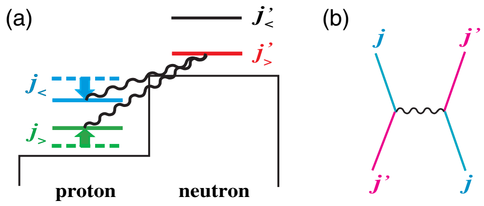

FIG. 17. (a) Schematic picture of the monopole interaction produced by the tensor force between a proton in $j_{>,<} = l \pm 1/2$ and a neutron in $j'_{>,<} = l' \pm 1/2$. (b) Exchange processes contributing to the monopole interaction of the tensor force. From Otsuka *et al.*, 2005.

$$\mathcal{S}_{ij} = \begin{cases} \frac{3}{4} \; -\frac{1}{4} \; = \; \frac{1}{2}, & \text{for (a)}, \\ 0 \; -\frac{1}{4} \; = \; -\frac{1}{4}, & \text{for (b)}. \end{cases} \tag{60}$$

The tensor force works for the two cases in Figs. 16(a) and 16(b) with opposite signs. The actual sign of f in Eq. (54) is positive, while the $\vec{\tau}_i \cdot \vec{\tau}_j$ term becomes $-3/4$ for $T = 0$, where T stands for the coupled isospin of the nucleons. The case in Fig. 16(a) gains the binding energy from the tensor force and indeed corresponds to the deuteron. The other case is actually unbound. In the case of $T = 1$, the attractive effect from the tensor force is 3 times weaker than in the $T = 0$ case in a naive approximation.

3. Tensor-force effect and orbital motion: Intuitive picture

We next consider tensor-force effects on the ESPEs in nuclei: the reduction of the spin-orbit splitting. As shown in this and subsequent sections, the monopole interaction of the tensor force is always attractive between $j_>$ and $j'_<$ orbits, whereas it is always repulsive between $j_>$ and $j'_>$ as well as between $j_<$ and $j'_<$. Figure 17 shows a typical case in which the occupation of the neutron $j'_>$ orbit changes the splitting between the proton $j_>$ and $j_<$ orbits, as expected by applying these monopole matrix elements to Eq. (38). Such changes lead us to the significant variation of the shell structure, i.e., shell evolution, in association with sizable occupations of a particular orbit. This basic feature was presented by Otsuka *et al.* (2005), followed by further developments. We discuss here the mechanism and consequence of such tensor-force-driven shell evolution in some detail, including those developments.

Figure 18 shows, in an intuitive way, the phenomena we are looking into. Spins are shown by arrows, and they are both set to be up because of $S = 1$ for the tensor force. We compare two cases: (a) the tensor-force coupling between $j_>$ and $j'_<$ orbits, and (b) the one between $j_>$ and $j'_>$ (and also $j_<$ and $j'_<$) orbits.

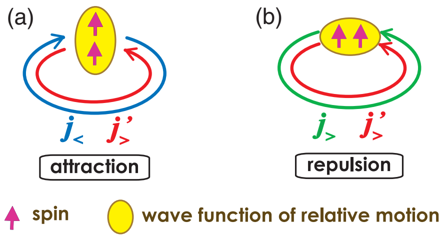

FIG. 18. Intuitive picture of the tensor force acting on two nucleons on orbits j and j'. From Otsuka *et al.*, 2005.

Before evaluating these couplings quantitatively, we present a simplified picture. This is based on the argument first shown briefly by Otsuka *et al.* (2005), followed by an elaborate description by Otsuka (2013), and by a further extended version with a figure by Otsuka (2014). As the last one is the most extensive but is in Japanese, we provide a slightly revised text and figure here.

We begin with the case shown in Fig. 18(a), where a nucleon in $j_<$ is interacting with another in $j'_>$ through the tensor force. Since the spin of each nucleon is fixed to be up, two nucleons must rotate on their orbits in opposite ways. We shall look into the relative motion of the two interacting nucleons, as the interaction between them is relevant only to their relative motion and not to their center-of-mass motion. We model the relative motion by a linear motion on the x axis. When two nucleons are close to each other within the interaction range, which is shorter than the scale of the orbital motion, the motion of two nucleons can be approximated by a linear motion, and the interaction works only within this region. It is also assumed that the two nucleons continue to move on the x axis, which is fulfilled in the present case. As the tensor-force potential becomes quite damped at the distance $\gtrsim 2$ fm, this is a reasonable modeling for nuclei with larger radii.

In this linear-motion model, the wave functions of the two nucleons are approximated by plane waves. The case shown in Fig. 18(a) corresponds to the "head-on collision" in the linear-motion model. The case shown in Fig. 18(b) corresponds, on the other hand, to the parallel linear motion of the two nucleons. We assign indices 1 and 2 to the two nucleons. Their wave numbers on the x axis are denoted by k_1 and k_2, while their coordinates are denoted by x_1 and x_2. The wave function Ψ consists of products of two plane waves. We now take a system of a proton and a neutron in the total isospin $T = 0$, which is antisymmetric with respect to the exchange of the nucleons 1 and 2. The spin part is $S = 1$, which is symmetric. As the total wave function must be antisymmetric, the coordinate wave function has to be symmetric, taking a form such as

$$\begin{aligned} \Psi \propto e^{ik_1x_1} e^{ik_2x_2} + e^{ik_2x_1} e^{ik_1x_2} &= e^{iKX}\{e^{ikx} + e^{-ikx}\} \\ &= 2e^{iKX}\cos(kx), \end{aligned} \tag{61}$$

where center-of-mass and relative momenta are defined as

$$K = k_1 + k_2, \qquad k = k_1 - k_2, \tag{62}$$

respectively, and center-of-mass and relative coordinates are defined likewise as

$$X = (x_1 + x_2)/2, \qquad x = (x_1 - x_2)/2. \tag{63}$$

With these definitions, the relative motion is expressed by the wave function

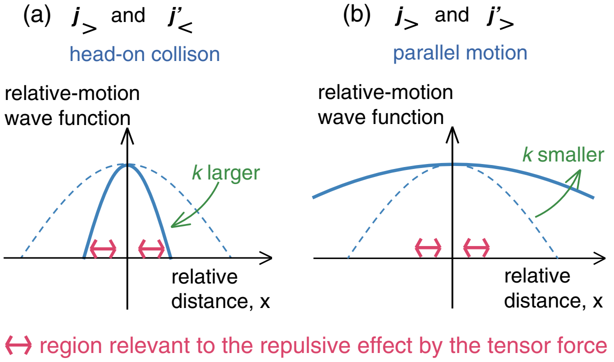

FIG. 19. Intuitive picture of the tensor force acting between two nucleons in a one-dimensional model. The relative-motion wave function is shown for (a) head-on collision and (b) parallel motion cases. In (a) [(b)], the change is shown as the relative momentum k becomes larger (smaller). See the text for explanation. Adapted from Otsuka, 2014.

$$\phi(x) \propto \cos(kx), \tag{64}$$

and the center-of-mass motion has a wave number K for e^{iKX}.

In the present case [i.e., Fig. 18(a)], $k_1 \sim -k_2$ can be assumed. The relative motion then has a large momentum, $k \sim 2k_1$. Its wave function $\phi(x)$ is shown in Fig. 19(a), with the trend of increasing k. We note that $K \sim 0$ with $k_1 \sim -k_2$, implying the center of mass being almost at rest or a nearly uniform wave function of the center-of-mass motion.

Based on Fermi momentum in nuclei, k is considered to be of the order of magnitude 1 fm^{-1}, not to exceed $\sim$1.5 fm^{-1}. From the range of the force, the area inside $x \sim 1$ fm is relevant, as the tensor-force potential becomes weak beyond 2 fm. Thus, the relevant range of kx in Eq. (64) is $|kx| \lesssim \pi/2$. Because of this, Fig. 19(a) displays up to the first zeros in both directions. The wave function $\phi(x)$ in Eq. (64) is damped more quickly for k larger within this range; see Fig. 19(a). Figure 16 shows that two nucleons attract each other if they are displaced in the direction of spin, but they repel each other if they are displaced in the direction perpendicular to the spin, i.e., the x axis now. We point out that if two nucleons are at a very short distance without high momenta, the tensor force does not work because its angular dependence comes from the spherical harmonics $Y^{(2)}$, prohibiting a finite probability at zero distance. The two nucleons should be at a certain distance in order to experience some effects, attractive or repulsive, from the tensor force. If the distance is too large, the effect is diminished. Thus, schematically, the region shown by bidirectional arrows in Fig. 19 is relevant to the tensor force, which is repulsive presently. With larger relative momentum k, Fig. 19(a) suggests that the wave function is damped faster or the region of sizable probability amplitude is more compressed along the x axis. This occurs in the region where the tensor force works repulsively. Thus, the reduction of the repulsion takes place more strongly with larger k. This means that as k becomes larger, the repulsion becomes weaker. On the other hand, the attraction due to the z (spin)-axis wave function remains basically unchanged. This is merely the net effect becoming more attractive.

We now come back from one-dimensional modeling to the three-dimensional orbital motion. The relative-motion wave function is discussed in a similar manner. The yellow shaded area in Fig. 18(a) indicates, schematically, the region with a sizable probability amplitude of the relative-motion wave function, as previously discussed. Its vertically stretched shape implies the attractive net effect, which is consistent with the deuteron case.

We now move on to the case of Fig. 18(b). The corresponding case in the linear-motion model is shown in Fig. 19(b). The parallel motion of the two nucleons occurs, and $k_1 \sim k_2$ can be assumed. The relative motion then has a small momentum, $k \sim 0$, implying a stretched wave function of the relative motion along the x axis, as shown in Fig. 19(b). The probability amplitude then turns out to be large in the region of the repulsive effect of the tensor force, yielding a net repulsive effect assuming that the net effect vanishes before this repulsive enhancement. This case corresponds to Fig. 18(b), where the two nucleons are apart from each other in the direction perpendicular to the total spin. The region of larger probability amplitude of the relative wave function (indicated by the yellow area) is stretched horizontally, which is consistent with the case other than the bound deuteron shown in Fig. 16(b).

In the previous linear-motion model, the wave functions in the y and z directions are not discussed. The probability amplitude in the z direction contributes to the attraction, whereas those in the y direction contribute to the repulsion. Those amplitudes are not constant, unlike the ideal plane-wave modeling. But they are not affected by the mechanism based on the relative momentum discussed so far, and hence they do not differ between the two cases represented by Figs. 16(a) and 16(b). In short, by having k high enough for the Fig. 16(a) case, the linear-motion wave function is pushed into the region with no sensitivity to the tensor force, but only the attractive effect remains. On the contrary, k becomes $\sim$0 for the Fig. 16(b) case, and the full repulsion works out.

Thus, we obtain a robust picture that $j_<$ and $j'_>$ (or vice versa) orbits attract each other, whereas $j_>$ and $j'_>$ (or $j_<$ and $j'_<$) orbits repel each other. As the monopole interaction represents average effects, it is natural that they follow the same trend. We soon discuss analytically and numerically how the monopole matrix elements behave. Note that the essence of the previous one-dimensional explanation can also be considered Heisenberg's uncertainty principle.

We now make some remarks on the findings made so far. The coordinate wave function is symmetric in the previous cases, corresponding to the coupling between the S and D waves of the relative motion. If the total isospin is $T = 1$, the antisymmetric coordinate wave function is taken, corresponding to P waves. In this case, the wave function in Eq. (64) is replaced by $\sin(kx)$. This wave function produces a horizontally stretched wave function, reversing the previous argument for the case in Fig. 18(a). However, because of the isospin dependence [see $(\vec{\tau}_1 \cdot \vec{\tau}_2)$ in Eq. (57)], there is another sign change, producing an attractive effect in total. Thus, $j_>$-$j'_<$ and $j_<$-$j'_>$ couplings always give us an attractive effect, whereas $j_>$-$j'_>$ and $j_<$-$j'_<$ couplings are repulsive.

The radial wave functions of the two orbits must be similar in order to have sizable monopole matrix elements. In addition, a narrow distribution in the radial direction is favored in order to have a "deuteronlike" shape for the relative-motion wave function. This is fulfilled if the two orbits are both near the Fermi energy because their radial wave functions have rather sharp peaks around the surface. If the radial distributions of the two orbits differ, not only does their overlap becomes smaller, but the relative spatial wave function is stretched in the radial direction, which weakens the deuteron-like shape, making the effect less pronounced. Note that for the same radial condition larger ℓ and ℓ' enhance the tensor monopole effect in general, as their relative momentum increases; see Fig. 18.

4. Tensor-force effect and orbital motion: Analytic relations

We now move on to the analytic expression on the monopole matrix element. An identity on the monopole matrix element of the tensor force was derived by Otsuka *et al.* (2005), showing properties consistent with the previous discussions. For the orbits j and j', the following identity was derived for the tensor force by Otsuka *et al.* (2005),

$$(2j_> + 1)V_T^{\text{ten};m}(j_>, j') + (2j_< + 1)V_T^{\text{ten};m}(j_<, j') = 0, \quad (65)$$

where j' is either $j'_>$ or $j'_<$. The identity in Eq. (65) can be proved, for instance, with angular-momentum algebra by summing all spin and orbital magnetic substates for the given ℓ, where $j_{>,<} = \ell \pm 1/2$. The quickest but a somewhat more mathematical proof is described here: the left-hand side of Eq. (65) is equivalent to the total effect of the $T = 0$ or 1 tensor force from the fully occupied $j_>$ and $j_<$ orbits coupled with a nucleon in the orbit j'. In the state composed of fully occupied $j_>$ and $j_<$ orbits, all magnetic substates of ℓ and those of spin $1/2$ are fully occupied. This means that the total spin should be zero. The sole nucleon in the j' orbit has a spin $1/2$, which then constitutes the total spin $0 + 1/2 = 1/2$. The spin sector of the tensor force in Eq. (57) is $[\vec{\sigma}_1\,\vec{\sigma}_2]^{(2)}$, which has a rank 2 angular momentum carried by the operator. If this operator is sandwiched by the states of spin $1/2$, the angular momentum cannot be matched, and the outcome is zero. Thus, one can prove the identity. The proof can also be made through the recoupling of angular momenta in the monopole matrix elements and the explicit form of the tensor force. In all of these proofs, it is assumed that the radial wave function is the same for $j_>$ and $j_<$ orbits, which is exactly fulfilled in the harmonic oscillator, and practically so in other models if the orbits are well bound.

We make some remarks on this identity.

- By moving the second term to the right-hand side of Eq. (65), one sees that the $j_>$-j' and $j_<$-j' couplings always have opposite signs, which is perfectly consistent with the intuitive explanation in Sec. IV.B.3. There are no exceptions. On the other hand, the identity in Eq. (65) does not suggest which sign is positive, or vice versa. The intuition explained in Sec. IV.B.3 plays a crucial role for the general argument.
- Although this identity is not applicable to the cases with $j_>$ or $j_< = j'$ in Eq. (65) with a good isospin ($T = 0$ or 1), quite similar behavior is found numerically. We note that, despite this feature, this identity holds exactly for the proton-neutron interaction in the proton-neutron formalism. Thus, the opposite sign is a really universal feature of the monopole matrix elements of the tensor force, and it can be used in all cases.
- One can prove that $V_T^{\text{ten};m}(j_>, j') = 0$ for j or $j' = s_{1/2}$. This is reasonable, as one cannot define $j_>$ or $j_<$ for an s orbit.
- As already mentioned, Eq. (65) suggests that, if both $j_>$ and $j_<$ orbits are fully occupied, there is no monopole effect from the tensor force on any orbit. Consequently, LS closed shells produce no monopole effect from the tensor force.
- The previous derivation also indicates that only those exchange processes shown in Fig. 17(b) contribute to the monopole matrix elements of the tensor force, while the contribution of direct processes vanishes. The same property holds for the spin-isospin central interaction discussed in Sec. IV.A. This can be understood from the point of view that the vertex $(\vec{\sigma} \cdot \nabla)$ in Eq. (53) does not allow a monopole direct process. If only exchange terms remain, the spin-coordinate contributions of $T = 0$ and 1 are just the opposite. Combining this property with $(\vec{\tau}_1 \cdot \vec{\tau}_2)$ in Eq. (57), one obtains

  $$V_{T=0}^{\text{ten};m}(j, j') = 3V_{T=1}^{\text{ten};m}(j, j'), \quad \text{for } j \neq j'. \quad (66)$$

  Thus, the proton-neutron tensor monopole interaction is twice as strong as the $T = 1$ monopole interaction. This implies also that the monopole effect from the tensor force has the same sign between $T = 0$ and 1, provided that $(\vec{\tau}_1 \cdot \vec{\tau}_2)$ is included in the potential.

Figures 20 and 21 display some examples of the monopole matrix elements of the π-meson + ρ-meson exchange tensor force with the parameters of Osterfeld (1992). The same set of

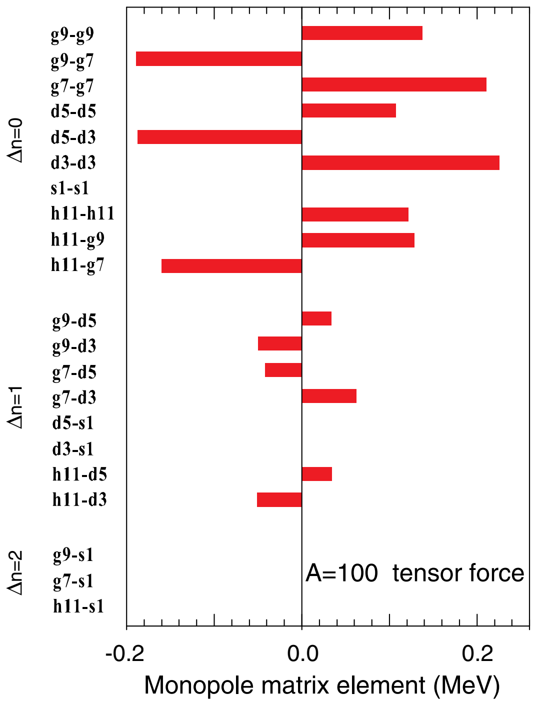

FIG. 20. Monopole matrix elements of the tensor force in the $T = 0$ channel. The orbit labeling is abbreviated as g9 for $1g_{9/2}$, etc. The orbits are from the valence shell for $A = 100$.

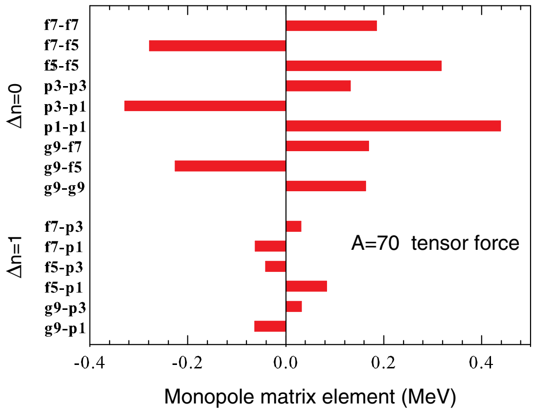

FIG. 21. Monopole matrix elements of the tensor force in the $T=0$ channel. The orbit labeling is abbreviated as f7 for $1f_{7/2}$, etc. The orbits are from the valence shell for $A=70$.

single-particle orbits are taken as in Fig. 13. The identity in Eq. (65) is exactly fulfilled. The magnitude of the monopole matrix elements is generally larger for the central force, while the variations, for instance, within the spin-orbit partners, are of the same order of magnitude between the central and tensor forces. Their competition produces intriguing phenomena in many cases.

C. Combination of the central and tensor forces

The previous two sections, Secs. IV.A and IV.B, presented the monopole interactions from the central and tensor forces. We combine them here.

The central and tensor forces are major components in the effective NN interaction used for nuclear-structure studies. As typical examples of such effective NN interactions, we take the interactions SDPF-M, GXPF1A, and G matrix, described by Utsuno *et al.* (1999), Honma *et al.* (2005), and Hjorth-Jensen, Kuo, and Osnes (1995), respectively. The first two were obtained by fitting some two-body matrix elements to experimental energy levels using microscopically derived interactions as the initial input. In addition, the *sd*-shell part of SDPF-M was obtained by modifying the USD interaction (Brown and Wildenthal, 1988). The G-matrix interaction refers to G-matrix plus in-medium corrections by the Q-box formalism (Hjorth-Jensen, Kuo, and Osnes, 1995) and is referred to in this way hereafter for brevity.

The monopole matrix elements of these interactions are shown in Fig. 22, where Figs. 22(a)–22(d) are for the pf shell, while Figs. 22(e)–22(h) are for the *sd* shell. The $T=0$ matrix elements are shown in Figs. 22(a), 22(b), 22(e), and 22(f), while the $T=1$ matrix elements are shown in Figs. 22(c), 22(d), 22(g), and 22(h).

In Fig. 22(a), the monopole matrix elements from the GXPF1A and G-matrix interactions are shown as well as those obtained from the π-meson $+$ ρ-meson exchange tensor force with the parameters of Osterfeld (1992).

Otsuka, Suzuki, Honma *et al.* (2010) pointed out that the kink pattern is quite similar among the GXPF1A, G-matrix, and tensor-force monopole matrix elements. This similarity is indeed remarkable and is indicative of the tensor-force origin of the kinks of the other two. We can subtract this tensor-force contribution from the GXPF1A or G-matrix results, as shown in Fig. 22(b). It was also noted by Otsuka, Suzuki, Honma *et al.* (2010) that the remaining monopole matrix elements are flat. In order to reproduce such monopole matrix elements, a Gaussian central force was introduced by Otsuka, Suzuki, Honma *et al.* (2010). The monopole-based universal interaction, called $V_{\rm MU}$, was then introduced, being composed of this central force and the π-meson $+$ ρ-meson exchange tensor force. The parameters of the central force [see Eq. (47)] were selected by Otsuka, Suzuki, Honma *et al.* (2010) as $f_{1,0} = f_{0,0} = -166$ MeV, $f_{0,1} = 0.6 f_{1,0}$ and $f_{1,1} = -0.8 f_{1,0}$, and $\mu = 1$ fm. The $V_{\rm MU}$ interaction was described by Otsuka, Suzuki, Honma *et al.* (2010): "[W]e can describe the monopole component by two simple terms: the tensor force generates 'local' variations, while the Gaussian central force produces a flat 'global' contribution." This is illustrated graphically in Fig. 23. Here "local" refers to the strong dependences on the single-particle orbits up to the sign changes, whereas "global" refers to the weak dependences with large magnitudes.

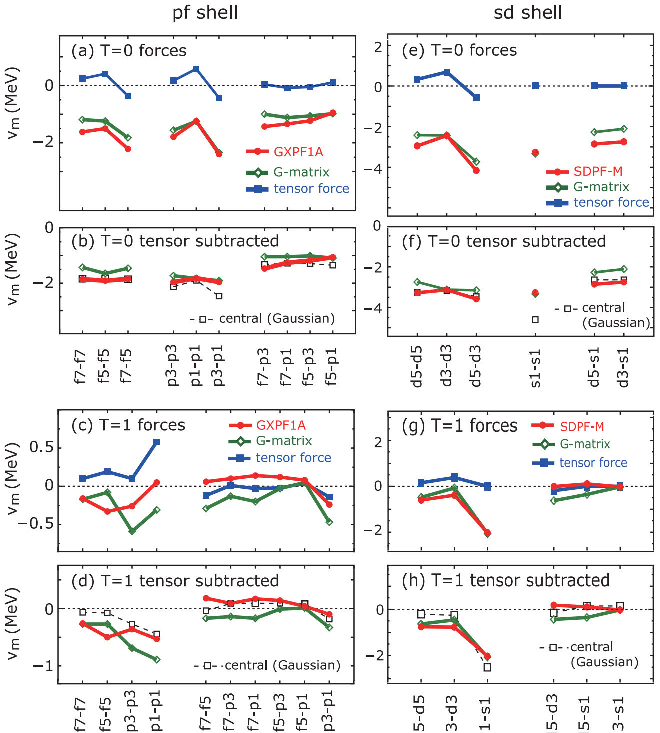

FIG. 22. Monopole matrix elements of various forces for (a)–(d) pf and (e)–(h) *sd* shells. In (b), (d), (f), and (h), the tensor-force effect is subtracted from the others, and results from a Gaussian central force are shown. Adapted from Otsuka, Suzuki, Honma *et al.*, 2010.

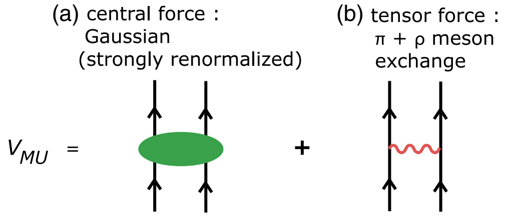

FIG. 23. Diagrams for the $V_{\rm MU}$ interaction. From Otsuka, Suzuki, Honma *et al.*, 2010.

The $T = 1$ monopole matrix elements are shown in Fig. 22(c). One notices that they are much weaker than the $T = 0$ monopole matrix elements, by a factor of about $1/10$. This large difference reflects a general trend. Within such small monopole matrix elements, the pattern is not so simple. Figure 22(d) shows that some of the $T = 1$ monopole matrix elements of the central Gaussian potential are repulsive.

Moving from the pf shell to the sd shell, quite similar properties can be found in Figs. 22(e)–22(h). Note that the parameters of the $V_{\rm MU}$ potential are independent of the orbits and the shells. The good description is remarkable in this respect. The reason for this with respect to the tensor force is presented in Sec. V.A.

D. Shell evolution driven by the central and tensor forces in actual nuclei

Here we demonstrate how the shell evolution actually occurs due to the central and tensor forces. The tensor force is taken from the π-meson + ρ-meson exchange potential in all cases (as in the $V_{\rm MU}$ interaction) in order to clarify the underlying mechanism. Likewise, the central force is taken also from the $V_{\rm MU}$ interaction for all cases, exhibiting different roles of these interactions in a consistent manner.

1. Inversion of proton $1f_{5/2}$ and $2p_{3/2}$ in Cu isotopes

One of the most visible examples of the shell evolution driven by the tensor force is the change of the proton $1f_{7/2}$-$1f_{5/2}$ splitting due to neutron occupations of the $1g_{9/2}$ orbit from the theoretical viewpoint. We describe this case in some detail, as it is one of the early examples regarding the tensor force. The underlying mechanism can be understood by reviewing Fig. 18 in a straightforward way. Namely, in this case, the neutron $j'_>$ orbit is $1g_{9/2}$, and it is occupied by more neutrons as we move on the Segrè chart from ^{69}Cu to heavier Cu isotopes. The changes of the ESPEs of the proton $j_> = 1f_{7/2}$ and $j_< = 1f_{5/2}$ orbits are given by following Eq. (38) as

$$\Delta\epsilon^p_{f_{5/2}} = V^m_{pn}(f_{5/2}, g_{9/2})\Delta n^n_{g_{9/2}} \tag{67}$$

and

$$\Delta\epsilon^p_{f_{7/2}} = V^m_{pn}(f_{7/2}, g_{9/2})\Delta n^n_{g_{9/2}}, \tag{68}$$

where the hat symbol is omitted because the occupation number of the neutron $1g_{9/2}$ orbit is treated as a c number here. Note that just such a simple treatment was mentioned as a possible option in Sec. III.D. From the $V_{\rm MU}$ interaction, the monopole matrix elements have two sources: one from the central force and the other from the tensor force. Table II shows their corresponding values. One sees that, between the two couplings $1f_{5/2}$-$1g_{9/2}$ and $1f_{7/2}$-$1g_{9/2}$, the central force gives a somewhat stronger attraction to the latter, as can be expected from Fig. 13(b). On the other hand, the tensor force pushes the $1f_{5/2}$ orbit down with more neutrons in the $1g_{9/2}$ orbit while pulling the $1f_{7/2}$ orbit up at the same time.

TABLE II. Monopole matrix elements from the central and tensor forces. The unit is the MeV. The mass number $A = 70$ is taken for the harmonic oscillator wave function of the single-particle orbit.

Proton orbit	Neutron orbit	Central	Tensor
$1f_{5/2}$	$1g_{9/2}$	−0.63	−0.15
$1f_{7/2}$	$1g_{9/2}$	−0.70	+0.11
Difference between $1f_{5/2}$ and $1f_{7/2}$		+0.07	−0.26
$2p_{3/2}$	$1g_{9/2}$	−0.46	+0.02
Difference between $1f_{5/2}$ and $2p_{3/2}$		−0.17	−0.17

The ESPEs provided by Eqs. (67) and (68) are shown in the left panel of Fig. 24, where the number of neutrons in the $1g_{9/2}$ orbit is given by $N - 40$ as the filling scheme is taken. The ESPEs at $N = 40$ are obtained from empirical values (Grawe *et al.*, 2005; Otsuka, Suzuki, Honma *et al.*, 2010). The full V_{MU} interaction is taken for the ESPEs displayed with solid lines in the left panel of Fig. 24, while the dashed lines depict results only with the central force. One confirms the same trends as discussed previously: the central force (with neutrons in the $1g_{9/2}$ orbit) slightly repels the $1f_{5/2}$ and $1f_{7/2}$ orbits from each other, while the tensor force brings them distinctly closer. The $1f_{5/2}$-$1f_{7/2}$ splitting is ~8 MeV at $N = 40$, but it is decreased to ~6 MeV at $N = 50$. The $Z = 28$ gap is between the $2p_{3/2}$ and $1f_{7/2}$ orbits at $N = 40$ with a gap of ~6 MeV, whereas it is between the $1f_{5/2}$ and $1f_{7/2}$ orbits at $N = 50$ with a gap of ~6 MeV.

The lowering of the proton $1f_{5/2}$ orbit produces another significant consequence. The left panel of Fig. 24 shows that the proton $2p_{3/2}$ orbit comes down, as a function of N, more slowly than the $1f_{5/2}$ orbit, and their order is inverted around $N = 45$. In fact, Table II suggests that the central-force contribution to the lowering of the proton $2p_{3/2}$ orbit is ~2/3 of the one for $1f_{7/2}$ or $1f_{5/2}$, and the tensor-force contribution is almost negligible. These properties are quite natural due to differences in the radial wave functions. Table II shows also how the $1f_{5/2}$-$2p_{3/2}$ gap is changed by the central and tensor forces. The two forces contribute to the inversion almost equally, and the total effect is large enough.

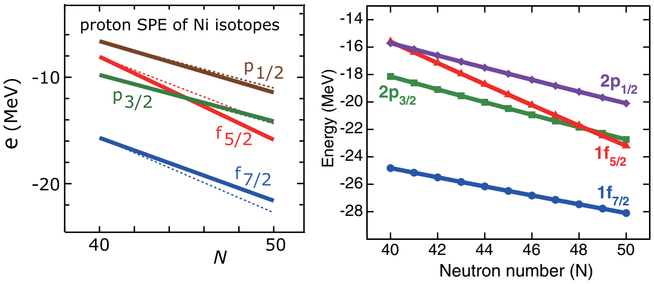

FIG. 24. (Left panel) Proton ESPEs of Cu isotopes predicted by the V_{MU} interaction (solid lines). Dashed lines are obtained only with the central-force part. The neutron number in the $1g_{9/2}$ orbit is equal to $N - 40$, as the filling scheme is assumed. From Otsuka, Suzuki, Honma *et al.*, 2010. (Right panel) Same quantities by the A3DA-m Hamiltonian used by Sahin *et al.* (2017). From Sahin *et al.*, 2017.

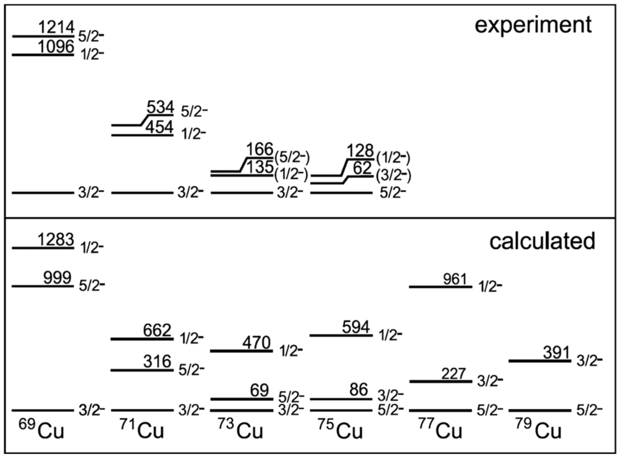

FIG. 25. Energy of the lowest levels from experiment and shell-model calculations. From Flanagan *et al.*, 2009.

The change of the ESPE of the proton $1f_{5/2}$ orbit has been investigated experimentally. Earlier investigations (Franchoo *et al.*, 1998, 2001) were made for ^{69,71,73}Cu prior to the previously presented theoretical studies. The experimental findings were compared to shell-model calculations (Ji and Wildenthal, 1989; Sinatkas *et al.*, 1992). The main message may be found in the quoted statements "unexpected and sharp lowering of the $\pi f_{5/2}$ orbital" and "the energy shift originates from the residual proton-neutron interaction, while its magnitude is proportional to the overlap of the proton and neutron wave function" (Franchoo *et al.*, 2001). There was no mention of the tensor force, and the lowering of the proton $1f_{5/2}$ orbit seems to have been attributed to the central force. We can see from Table II that the central force accounts for half of the effect. Note that spectroscopic factors have been deduced for ^{69,71}Cu (Morfouace *et al.*, 2015). We point out that the interplay of collective and single-particle behavior was discussed for $^{67-73}$Cu by Stefanescu *et al.* (2008).

The experimental studies were further extended by Flanagan *et al.* (2009) up to ^{75}Cu, as shown in Fig. 25. The inversion between the lowest $5/2^-$ and $3/2^-$ levels was observed for the first time in the Cu isotopic chain. The role of the tensor force was known then, and the work was recognized as "a crucial step in the study of the shell evolution" (Flanagan *et al.*, 2009). The observed levels were compared to shell-model calculations by Brown and Lisetskiy (2009) with a reasonable agreement. It is very likely that a proper amount of tensor force was included in the shell-model interaction as a result of the fit well done (Lisetskiy *et al.*, 2004, 2005). The single-particle nature of the lowest $5/2^-$ being the $1f_{5/2}$ single-particle state in ^{75}Cu was confirmed by the measured magnetic moment and by the shell-model calculation, as was the lowest $3/2^-$ being the $2p_{3/2}$ single-particle state in ^{69}Cu. On the other hand, the ground state (i.e., the $3/2^-$ state) of ^{71,73}Cu was shown to have a mixed nature. Besides such intermediate situations, an inversion between the $1f_{5/2}$ and $2p_{3/2}$ states has thus been suggested (Flanagan *et al.*, 2009), and the trend was extended to heavier Cu isotopes (Daugas *et al.*, 2010; Köster *et al.*, 2011). This series of experiments showing a clear signal of the lowering of the $1f_{5/2}$ orbit can be considered a major milestone in establishing the shell evolution.

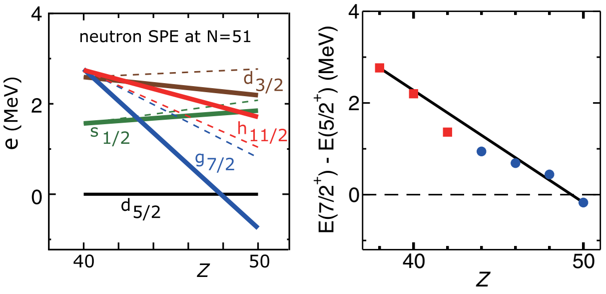

FIG. 26. (Left panel) Neutron ESPEs relative to the $2d_{5/2}$ orbit as a function of Z. Dashed and full lines have the same meaning as in Fig. 24. Adapted from Otsuka, Suzuki, Honma *et al.*, 2010. (Right panel) Measured energies of the $7/2^+$ level relative to the $5/2^+_1$ states for $N = 51$ isotones. The squares show states with large $1g_{7/2}$ single-neutron strength, as quoted by Federman and Pittel (1977). The circles stand for the lowest observed $7/2^+$ level (ENSDF, 2017). The present assignment for ^{101}Sn is by Darby *et al.* (2010). The straight line connects the points at $Z = 38$ and 50.

The effects of various correlations, including collective ones, have been investigated both theoretically and experimentally, but the main conclusion remains unchanged, apart from minor changes. For instance, the precise point of the inversion is sensitive theoretically to the adopted values of ESPEs at $N = 40$, which are not known to be so accurately constrained to date; see Fig. 24.

The structures of neutron-rich ^{77}Cu and ^{79}Cu isotopes have recently been studied experimentally by Sahin *et al.* (2017) and Olivier *et al.* (2017), respectively, and experimental data compared well to the results of the shell-model calculation with the A3DA-m Hamiltonian introduced in Tsunoda, Otsuka *et al.* (2014). The right panel of Fig. 24 indicates the ESPEs obtained from this Hamiltonian including the $1f_{5/2}$-$2p_{3/2}$ crossing, and it also shows that the $Z = 28$ gap becomes smaller but still remains greater than 4 MeV up to $N = 50$. As the shell-model calculations contain correlations in the configuration space, the $5/2^-$ and $3/2^-$ levels are inverted at $N = 46$, in agreement with experiment. Because the A3DA-m interaction contains empirical corrections (for the given model space) compared to the V_{MU} interaction, they produce a somewhat different reduction of the $1f_{7/2}$-$1f_{5/2}$ splitting, but the substantial reduction is common, which is consistent with the tensor-force-driven shell evolution.

2. Shell evolution from ^{90}Zr to ^{100}Sn

Another typical case of the tensor-force-driven shell evolution is discussed in Fig. 26, in the filling scheme on top of the $Z = 40$ and $N = 50$ closed shell. In the left panel of Fig. 26, the ESPEs of neutrons are displayed relative to the one for the $2d_{5/2}$ orbit, where the number of protons in the $1g_{9/2}$ orbit is increased from 0 to 10. This represents the change from ^{90}Zr to ^{100}Sn. The neutron ESPEs for $Z = 40$ were adjusted to experimental data including the fragmentation of single-particle strengths (ENSDF, 2017), and their evolution for larger Z's follows Eq. (39) with the V_{MU}

interaction. The corresponding experimental data, including those mentioned by Federman and Pittel (1977), are shown in the right panel of Fig. 26.

One finds, in the left panel of Fig. 26, two sets of calculated results: one (solid lines) is obtained with the full $V_{\rm MU}$ interaction, while the other (dashed lines) is only with the central-force part of $V_{\rm MU}$. A sharp drop of the $1g_{7/2}$ ESPE with the full $V_{\rm MU}$ interaction is remarkable, ending up with an ESPE below $2d_{5/2}$. A similar behavior is seen in the experimental data (see the right panel of Fig. 26). This drop is largely due to a strong proton-neutron monopole interaction on a proton in the $1g_{7/2}$ orbit generated by neutrons in the $1g_{9/2}$ orbit. The actual values of the relevant central-force monopole matrix elements are -0.51 MeV for the proton-neutron $1g_{9/2}$-$1g_{7/2}$ coupling and -0.32 MeV for the $1g_{9/2}$-$2d_{5/2}$ coupling (see Fig. 13 for the $T=0$ contribution), while the tensor-force contribution is -0.13 MeV for the former and $+0.02$ MeV for the latter (see Fig. 20 for the $T=0$ contribution). Thus, the difference between the two couplings is -0.19 MeV from central force, and -0.15 MeV from tensor force. The notable central-force contribution was suggested by Federman and Pittel (1977), as stated in Sec. IV.A.

The left panel of Fig. 26 also shows also that if only the central-force part is taken, the $1g_{7/2}$ and $1h_{11/2}$ ESPEs come down together (dashed lines). These two ESPEs, however, repel each other toward $Z=50$ if the tensor force is included (solid lines). This is because a repulsive monopole interaction works on the $h_{11/2}$ orbit due to the $j_>$-$j'_>$ coupling, whereas the tensor interaction is attractive on the $1g_{7/2}$, as discussed previously. This attraction produces an additional lowering of $1g_{7/2}$, letting it reach below $2d_{5/2}$ at $Z=50$. We note that a similar trend in the $1g_{7/2}$-$1h_{11/2}$ splitting was shown with a monopole-corrected G-matrix interaction by Sieja *et al.* (2009). The energy levels of ^{101}Sn have been investigated experimentally by Seweryniak *et al.* (2007) and Darby *et al.* (2010), whose results show different ground-state spins but are consistent with the lowering of the $1g_{7/2}$ orbit.

As a second point, we mention that the bunching of three orbits, $1h_{11/2}$, $2d_{3/2}$, and $3s_{1/2}$, seems to be consistent with the shell structure of the Sn isotopes. The left panel of Fig. 26 demonstrates that the tensor force plays a crucial role for obtaining it. The tensor-force contribution is thus essential for the shell structure of ^{100}Sn, which has further relevance to various issues of exotic nuclei.

Another feature is the relation to the Skyrme Hartree-Fock calculation shown in Fig. 27. With the SIII interaction, the $1g_{7/2}$-$2d_{5/2}$ gap is decreased by about 1.2 MeV. This change is comparable to the corresponding shift by the central force of the V_{MU} interaction. Note that the ESPE of the $1g_{7/2}$ ($2d_{5/2}$) orbit is predicted to be lower (higher) than the empirical value, and thereby the change of their splitting is smaller than that shown in Fig. 26. Thus, the tensor force is needed to account for a larger relative change between the $2d_{5/2}$ and $1g_{7/2}$ orbits, eventually leading to their crossing in Sn. Furthermore, the right panel of Fig. 27 indicates that the gap between the $1g_{7/2}$ and $2d_{5/2}$ orbits is even increased with the SLy4 interaction.

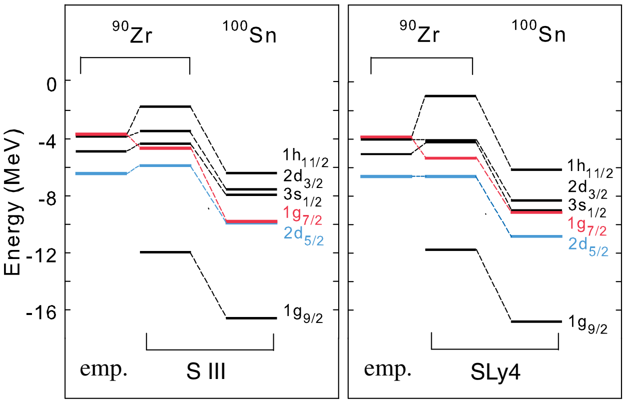

FIG. 27. Single-particle energies of ^{90}Zr and ^{100}Sn calculated by (left panel) SIII and (right panel) SLy4 Skyrme interactions.

3. Appearance of $N=16$ magic number and disappearance of $N=20$

The change of the neutron $1d_{3/2}$ ESPE is discussed in Sec. IV.A. Figure 14 shows that the neutron $1d_{3/2}$ ESPE is about 6 MeV above the $2s_{1/2}$ ESPE in ^{24}O, but it comes down by about 4 MeV in ^{30}Si.

This change is discussed in Sec. IV.A as a consequence of the strong attractive monopole matrix element between the $\ell+1/2$ and $\ell-1/2$ orbits. This strong coupling is included in shell-model effective interactions, e.g., SDPF-M (Utsuno *et al.*, 1999) and in the G matrix (Kuo and Brown, 1966), whereas it is weakened in some others, e.g., USD (Brown and Wildenthal, 1988). It is indicated in Sec. IV.A that the $\tau\tau\sigma\sigma$ interaction in Eq. (47) can lower, in principle, the neutron $1d_{3/2}$ orbit as protons occupy the $1d_{5/2}$ orbit. Although this coupling is strongest in Table I, if the $\tau\tau\sigma\sigma$ interaction is taken, the neutron $1d_{5/2}$ orbit is lowered by about half, implying some difficulty. On the other hand, the strong attraction between the $\ell+1/2$ and $\ell-1/2$ orbits was suggested, leading us to a sizable spin-isospin coupling (Otsuka *et al.*, 2001).

Four years later, Otsuka *et al.* (2005) proposed another origin in nuclear forces for this spin-isospin coupling, the tensor force. In fact, the tensor force provides the relevant monopole matrix elements $V_{pn}^{{\rm ten};m}(1d_{5/2},1d_{3/2})=-0.37$ MeV and $V_{pn}^{{\rm ten};m}(1d_{5/2},2s_{1/2})=0$ MeV. By having six protons in the $1d_{5/2}$ orbit, the $1d_{3/2}$ orbit is then lowered by 2.2 MeV relative to the $2s_{1/2}$ orbit. This implies that half of the lowering of the $1d_{3/2}$ orbit is due to the tensor force. We also stress that the neutron $1d_{5/2}$ orbit is pushed up by the tensor force with six protons in $1d_{5/2}$, in contrast to the $\tau\tau\sigma\sigma$ interaction.

The neutron $1d_{3/2}$ orbit needs to be shifted down by another 2 MeV relative to the $2s_{1/2}$ orbit by the central force because the tensor-force effect is robust (not that tunable), as we discuss in Sec. V.A. In fact, the central force should produce a weaker monopole matrix element for the $1d_{5/2}$-$2s_{1/2}$ coupling, and this is the case.

We mention here that some features of the $\tau\tau\sigma\sigma$ interaction are shared by the tensor force; for instance, the spin-isospin operator $\tau\sigma$ acts on the vertex in favor of spin-isospin-flip process, and only the exchange process contributes to the monopole matrix element (see Figs. 14 and 17). These properties produce stronger couplings between $j_>$ and $j_<$ orbits with a common ℓ for both the central and tensor forces, but only the tensor force also does it for $j_>$ and $j'_<$, i.e., $\ell \neq \ell'$. In this sense, the special importance of the spin-isospin interaction in the shell evolution in exotic nuclei was pointed out as an initial study by Otsuka *et al.* (2001), a precursor to more comprehensive studies including the tensor force.

The relative raising of the neutron $1d_{3/2}$ orbit from Fig. 14(a) to Fig. 14(b) occurs as Z is reduced from 14 to 8 while N is kept at 16. This isotonic change from a stable to an exotic nucleus creates an $N = 16$ gap and diminishes the $N = 20$ conventional gap. Thus, the present shell evolution can change the magic numbers. We mention here that the large $N = 16$ gap was recognized in an earlier shell-model study within the systematics of the oxygen isotopes (Brown, 1993). The gap was pointed out based on experimental data on the masses and radii (Ozawa *et al.*, 2000).

We come back to the $N = 20$ magic number in Secs. V.D and VI.A.

4. Appearance of $N = 34$ magic number in the isotonic chain

Another case of new magic numbers has been found in the Ca isotopes, with $N = 32$ and 34. A remarkable proton-neutron $j_>$-$j_<$ coupling within a major shell is seen in the shell evolution between Ca and Ni. Figure 28 displays this shell evolution concretely in terms of the V_{MU} interaction. We take the filling scheme, where no proton occupies the $1f_{7/2}$ orbit in ^{48}Ca. In ^{56}Ni, on the other side, eight protons occupy the $1f_{7/2}$ orbit, changing the ESPEs of the neutron orbits $1f_{5/2}$, $2p_{3/2}$, and $2p_{1/2}$. Figure 28 then indicates how much each orbit is moved with the decomposition into the tensor- and central-force monopole contributions. It is found that, in going from ^{56}Ni to ^{48}Ca, both forces contribute additively to the sharp rise of the $1f_{5/2}$ orbit relative to the $2p_{3/2}$ and $2p_{1/2}$ orbits. The splitting between the $2p_{3/2}$ and $2p_{1/2}$ orbits is slightly increased and becomes a (sub)magic gap, as the $1f_{5/2}$ orbit is not in between any longer.

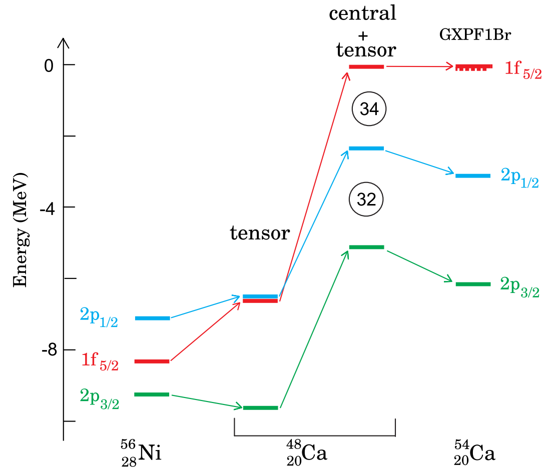

FIG. 28. Change of ESPEs from ^{56}Ni to ^{48}Ca, and to ^{54}Ca. The arrows indicate the change of the ESPE of each orbit. The arising magic numbers, $N = 32$ and 34, are shown in black circles. The dashed line just beneath the $1f_{5/2}$ ESPE (red bar) in the right column means the $1f_{5/2}$ ESPE calculated with one neutron hole in the $2p_{1/2}$ orbit.

Figure 28 exhibits the changes of the ESPEs with the decomposition into the tensor- and central-force monopole contributions. We point out that the monopole components of the tensor and central forces contribute to the evolution of the $1f_{5/2}$ ESPE, showing its sharp rise. The splitting between the $2p_{3/2}$ and $2p_{1/2}$ orbits remains almost unchanged and becomes a (sub)magic gap after the $1f_{5/2}$ orbit is shifted above $2p_{1/2}$. Thus, the $N = 32$ gap corresponds to the $2p_{3/2}$-$2p_{1/2}$ spin-orbit gap, but its effect is hidden if the $1f_{5/2}$ is lying between the $2p_{3/2}$ and $2p_{1/2}$ orbits. Thus, the evolution of the $1f_{5/2}$ orbit crucially affects the appearance of the $N = 32$ magic number. It is noted that the tensor force enlarges the gap between the $2p_{3/2}$ and the $2p_{1/2}$. The magic numbers 32 and 34 thus appear in going from Ni to Ca, as indicated in Fig. 28, as the eight protons in ^{56}Ni are taken away. We emphasize that the $N = 34$ gap basically vanishes when the tensor-force effect is taken away, and that is, since the present shell-evolution effect is linearly dependent on the number of proton holes in the $1f_{7/2}$ orbit, as Z decreases, the $N = 34$ (sub)magic structure fades away first and the $N = 32$ structure also disappears eventually.

The far-right part of Fig. 28 shows the shell evolution from ^{48}Ca to ^{54}Ca due to the neutron-neutron interaction, adding six more neutrons still in the filling scheme. The GXPF1Br shell-model interaction introduced in Steppenbeck *et al.* (2013) is used, as more fine details are relevant now. The neutron-neutron effective interaction produces the shell evolution with patterns very different from those of the proton-neutron interaction. Four and two neutrons occupy the $2p_{3/2}$ and $2p_{1/2}$ orbits, respectively, in ^{54}Ca. The ESPE is shown for the $1f_{5/2}$ orbit on top of the ^{54}Ca core, with a very small change from ^{48}Ca. As the $2p_{3/2}$ and $2p_{1/2}$ orbits are occupied in the ^{54}Ca core, we show the ESPE for the last neutron to occupy these orbits. The $2p_{3/2}$ ESPE is calculated for ^{54}Ca by assuming a fully occupied $2p_{1/2}$ orbit. In order to assess the energy needed for particle-hole excitation, in the far-right part of Fig. 28, the dashed line beneath the $1f_{5/2}$ level shows the ESPE calculated with one neutron hole in the $2p_{1/2}$ orbit, which is very close to the solid line. Thus, the effects of the neutron-neutron monopole interaction is minor and can be repulsive. The $2p_{3/2}$ and $2p_{1/2}$ ESPEs are somewhat lowered due to the pairing component between the same orbit, when they are occupied.

We can thus see the basic mechanism of the appearance of the $N = 32$ and 34 gaps. This was the prediction by Otsuka *et al.* (2001), a consequence of the strong attractive coupling between the $\ell + 1/2$ and $\ell - 1/2$ orbits with $\ell = 3$, analogous to a similar coupling with $\ell = 2$ leading to the $N = 16$ new magic number. The corresponding text of Otsuka *et al.* (2001) is as follows: "we can predict other magic numbers, for instance, $N = 34$ associated with the $0f_{7/2} - 0f_{5/2}$ interaction." Here $0f_{7/2,5/2}$ corresponds to $1f_{7/2,5/2}$ in the present notation. The experimental investigation of the $N = 34$ magic number in the Ca isotopes had not been feasible for over a

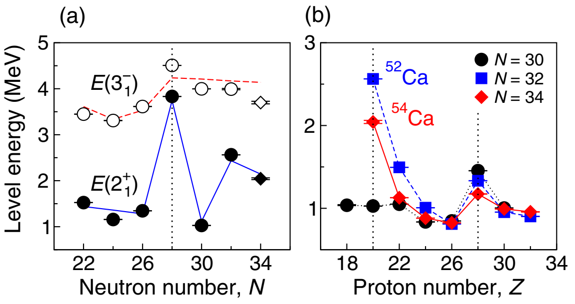

FIG. 29. First observed 2^+ levels as a function of (a) N and (b) Z. First observed 3^- levels are shown in (a). Adapted from Steppenbeck *et al.*, 2013.

decade, casting doubt over this magic number (Janssens, 2005). In 2013, finally, the 2^+ excitation energy was measured at the RIBF (Steppenbeck *et al.*, 2013) to be significantly higher than in heavier isotones consistent with an $N = 34$ gap, as shown in Fig. 29. A sharp rise of the 2^+ excitation energy as a function of Z was thus confirmed experimentally for ^{54}Ca, as shown in Fig. 29(b), in accordance with the rise of the $1f_{5/2}$ orbit from ^{56}Ni to ^{48}Ca; see Fig. 28. The intermediate situation between the Ca and Ni isotopes was discussed by Steppenbeck *et al.* (2013). The $N = 32$ gap in the Ca isotopes was investigated experimentally at ISOLDE in 1985 in terms of the 2^+ excitation energy (Huck *et al.*, 1985). The magic structures of Ca isotopes have attracted much attention in recent years (Prisciandaro *et al.*, 2001; Janssens *et al.*, 2002; Liddick *et al.*, 2004; Bürger *et al.*, 2005; Dinca *et al.*, 2005; Gade *et al.*, 2006; Perrot *et al.*, 2006; Rejmund *et al.*, 2007; Rodríguez and Egido, 2007; Honma, Otsuka, and Mizusaki, 2008; Coraggio *et al.*, 2009; Crawford *et al.*, 2010; Kaneko *et al.*, 2011; Hagen *et al.*, 2012a; Holt *et al.*, 2012; Utsuno *et al.*, 2012b; Wienholtz *et al.*, 2013; Steppenbeck *et al.*, 2015; Ruiz, Garcia *et al.*, 2016).

Figure 29(b) exhibits that raising pattern toward $Z = 20$ of the 2_1^+ level differs between $N = 32$ and 34 isotonic chains. Significant experimental efforts were made, particularly for Ti ($Z = 22$), for instance, by Janssens *et al.* (2002), Fornal *et al.* (2004, 2005), Dinca *et al.* (2005), and Liddick *et al.* (2004), partly because Ti is only $\Delta Z = 2$ away from Ca. As three quarters of the shift from Ni to Ca occurs in Ti in Fig. 28, the $1f_{5/2}$ level is located near the $2p_{1/2}$ level, making the $N = 32$ gap rather visible but not the $N = 34$ gap, which is consistent with these experiments. Thus, studies on Ti and Sc isotopes (Steppenbeck *et al.*, 2017) support the appearance mechanism of $N = 32$ and 34 magic numbers in Ca isotopes.

The levels of single-particle-like states on top of the $N(Z) = 28$ and $N(Z) = 50$ closure were discussed systematically by Grawe (2004), with sharp decreases of (a) neutron $1f_{5/2}$ with proton $1f_{7/2}$ filled, (b) proton $1f_{5/2}$ with neutron $1g_{9/2}$ filled, (c) proton $1g_{7/2}$ with neutron $1h_{11/2}$ filled, and (d) neutron $1g_{7/2}$ with proton $1g_{9/2}$ filled. Case (a) is simply the change from ^{48}Ca to ^{56}Ni depicted in Fig. 28. All cases are of the $j_>$-$j'_<$ coupling with large j and j'; hence, the sharp decreases can be understood in terms of the coherent effects of the central and tensor forces discussed thus far. Related systematic trends of the monopole matrix elements were obtained empirically by Sorlin (2014), indicating that the proton-neutron $1d_{5/2}$-$1d_{3/2}$ monopole matrix element is more attractive than the $1d_{5/2}$-$1f_{7/2}$ one, which is more attractive than the $1d_{5/2}$-$2p_{3/2}$ one. This is consistent with the monopole properties discussed, and it supports them.

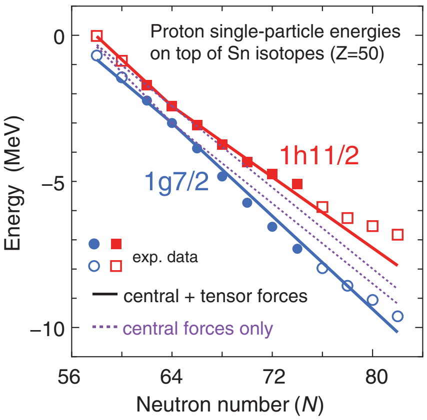

FIG. 30. ESPEs of proton $1h_{11/2}$ and $1g_{7/2}$ orbits in Sb isotopes as functions of N. Assuming a Sn-isotope core, the solid lines are calculated with the tensor-force effect, whereas the dotted lines are without it. Symbols are based on experimental values from Schiffer *et al.* (2004). Fragmentation of single-particle strength is considered for filled circles, while bare energies are used for open symbols. See the text for relevant arguments on those values. From Otsuka, 2013.

5. Repulsion between proton $1h_{11/2}$ and $1g_{7/2}$ orbits in the Sb isotopes

Figure 30 shows the ESPEs of the proton $1h_{11/2}$ and $1g_{7/2}$ orbits in Sb isotopes as a function of N. There are 51 protons in the Sb isotopes: one proton atop the $Z = 50$ magic core in the filling scheme. This last proton can be in either the $1h_{11/2}$ orbit or the $1g_{7/2}$ orbit. The experimental values are taken from Schiffer *et al.* (2004), who reported that the centroid of fragmented single-particle strengths were evaluated as much as possible. Some questions on the validity of this analysis have been raised, for instance, by Sorlin and Porquet (2008), in connection to the couplings to various collective modes, including the octupole one. While this remains an open problem both experimentally and theoretically, we discuss it here from the viewpoint of the monopole effect to explore what can be presented with such a simple argument. We expect more developments to lead to further clarifications.

Around the middle ($N \sim 66$) of the major shell between $N = 50$ and 82, the $1h_{11/2}$ and $1g_{7/2}$ orbits (or two corresponding experimental states) are close to each other with a gap of less than 1 MeV. The gap increases with N, as seen in Fig. 30. It was quite difficult to reproduce this enlargement of the gap within mean-field models when the experimental values were published (Schiffer *et al.*, 2004). In those Sb isotopes, the neutron $1h_{11/2}$ orbit is filled more and more as N increases. The monopole interaction from the tensor force is repulsive between the proton $1h_{11/2}$ orbit and the neutron $1h_{11/2}$ orbit; see Fig. 18. Its effect is, on the other hand, attractive between the proton $1g_{7/2}$ orbit and the neutron

$1h_{11/2}$ orbit; see also Fig. 18. In fact, the theoretical ESPEs in Fig. 30 are calculated from the monopole matrix elements [see Eq. (38)] of the V_{MU} interaction, which consists of the $\pi+\rho$ meson-exchange tensor force and the Gaussian central force, as discussed in Sec. IV.C.

The ESPEs in Fig. 30 are calculated with the monotonic increase of the uniform occupation probabilities of the neutron $1h_{11/2}$, $2d_{3/2}$, and $3s_{1/2}$ orbits starting from $N=64$ for simplicity. Figure 30 shows the ESPEs calculated without the tensor force (dashed lines), indicating that the two ESPEs come down together with the gap even slightly narrowing. Once the tensor force is included (solid lines in Fig. 30), however, it moves the two orbits farther apart from each other as N increases. A similar but simpler figure was shown in Fig. 4(d) of Otsuka *et al.* (2005), which was published immediately after Schiffer *et al.* (2004), demonstrating the explanation of the anomalous gap widening in terms of the tensor force for the first time. The gap increase can be explained almost perfectly once the tensor force is incorporated without an adjustment of the tensor-force strength. This point has to be clarified with more precise calculations including other correlations. We also point out the upbending curvature toward $N=82$ shown in Fig. 30 may suggest some effects beyond the monopole effect.

It is thus important and essential to examine to what extent other effects, for instance, couplings to collective excitations, affect the observed energy levels, while the tensor-force effects seem to remain a major mechanism.

E. Mean-field approaches to the tensor-force-driven shell evolution

The effect of the tensor force has been included in various recent studies based on mean-field models (Brown *et al.*, 2006; Long, Giai, and Meng, 2006; Otsuka, Matsuo, and Abe, 2006; Brink and Stancu, 2007; Colò *et al.*, 2007; Lesinski *et al.*, 2007; Bender *et al.*, 2009; Lalazissis *et al.*, 2009). Regarding the inclusion of the tensor force into Skyrme-based mean-field approaches, relatively few studies were done before these works, probably in consideration of some issues pointed out, for instance, in Bender, Heenen, and Reinhard (2003).

The importance of the tensor force was anticipated by Skyrme (1958) when the original form of the Skyrme interaction was proposed. The tensor force was, however, not studied much within the Skyrme-model calculations for a while, probably with the exception only of the work of Stancu, Brink, and Flocard (1977), who adopted the zero-range approximate form for the tensor force with terms mixing S and D waves of the relative motion as well as P waves (Skyrme, 1958; Vautherin and Brink, 1970). This form can be written as

$$\begin{aligned} v_T = {} & \tfrac{1}{2}T\{[(\vec{\sigma}_1\cdot\vec{k}')(\vec{\sigma}_2\cdot\vec{k}') - \tfrac{1}{3}(\vec{\sigma}_1\cdot\vec{\sigma}_2)k'^2]\delta(\vec{r}_1-\vec{r}_2) \\ & + \delta(\vec{r}_1-\vec{r}_2)((\vec{\sigma}_1\cdot\vec{k})(\vec{\sigma}_2\cdot\vec{k}) - \tfrac{1}{3}(\vec{\sigma}_1\cdot\vec{\sigma}_2)k^2]\} \\ & + U\{(\vec{\sigma}_1\cdot\vec{k}')\delta(\vec{r}_1-\vec{r}_2)(\vec{\sigma}_1\cdot\vec{k}) \\ & - \tfrac{1}{3}(\vec{\sigma}_1\cdot\vec{\sigma}_2)[\vec{k}'\delta(\vec{r}_1-\vec{r}_2)\vec{k}]\}, \end{aligned} \tag{69}$$

where $\vec{k}=(\vec{\nabla}_1-\vec{\nabla}_2)/2i$ acts on the right and $\vec{k}'=-(\vec{\nabla}_1-\vec{\nabla}_2)/2i$ acts on the left.

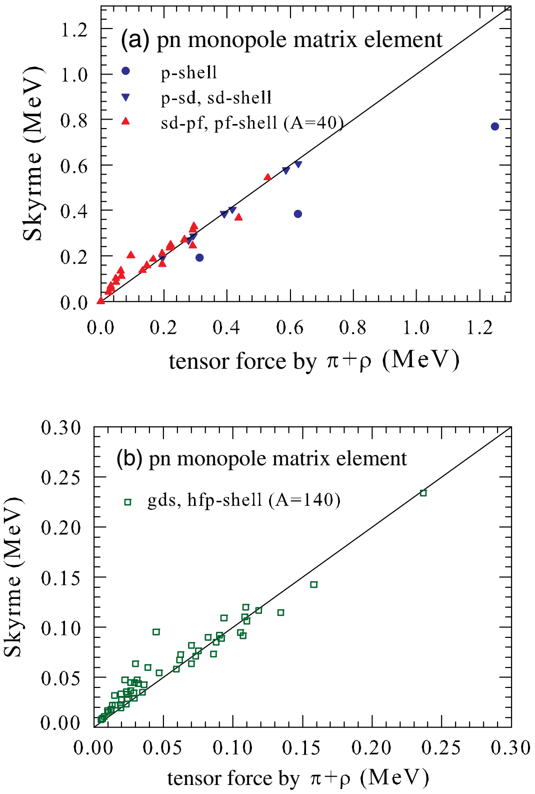

FIG. 31. Comparison of monopole matrix elements of the zero-range tensor force of Stancu, Brink, and Flocard (1977) to those of the $\pi+\rho$ meson-exchange tensor force. The p, sd, and pf shells are covered in (a), while the valence shell relevant to $A\sim 140$ is considered in (b). The parameter $\beta_T = 128.75\ \mathrm{MeV\,fm^5}$ is used.

The tensor term gives rise to additional spin-orbit strengths written as

$$\begin{aligned} \Delta W_n &= \alpha_T J_n + \beta_T J_p, \\ \Delta W_p &= \alpha_T J_p + \beta_T J_n, \end{aligned} \tag{70}$$

where J_ρ $(\rho = p, n)$ are the spin densities given by

$$J_\rho(r) = \frac{1}{4\pi r^3}\sum_a (2j_a+1)\left(j_a(j_a+1) - \ell_a(\ell_a+1) - \frac{3}{4}\right)R_a^2(r) \tag{71}$$

with occupied orbitals $\{a\}$. Since the spin-orbit potential for $\rho = p, n$ is $W_\rho \vec{\ell}\cdot\vec{\sigma}/r$, a large negative W_ρ gives a strong spin-orbit splitting. From the sign of $j_a(j_a+1) - \ell_a(\ell_a+1) - 3/4$, one can see that J_ρ increases and decreases with the occupation of the $\alpha = j_>$ and $j_<$ orbitals, respectively, and that changing J_ρ causes the evolution of the spin-orbit coupling as previously discussed. α_T and β_T correspond to like-particle and proton-neutron tensor forces. The equality $\beta_T = 2\alpha_T$ holds if the tensor force has the same isospin structure, $\tau_1\tau_2$, as the $\pi+\rho$ meson-exchange potential. Monopole terms of the tensor forces given by the two parameters are compared with those of the tensor forces by $\pi+\rho$ meson exchanges to study the validity of the use of the approximate zero-range form.

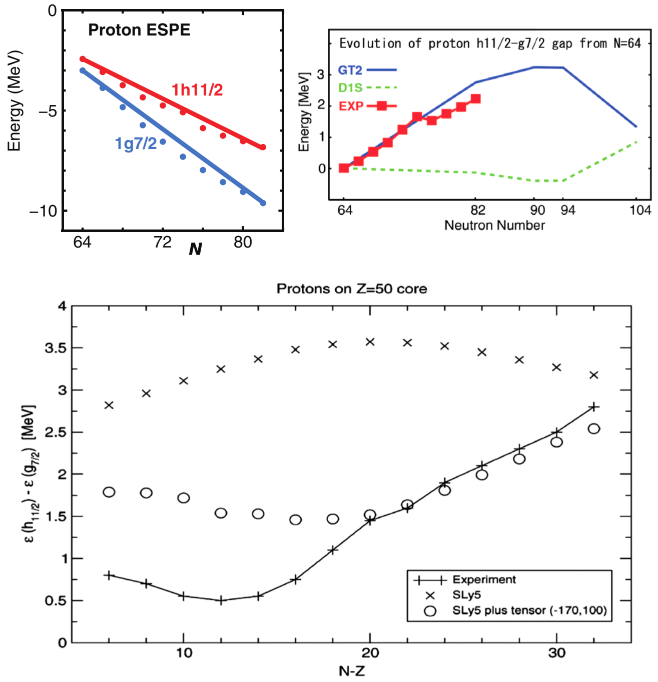

FIG. 32. Evolution of the proton $h_{11/2}$-$g_{7/2}$ gap in the Sb isotopes with and without the tensor term. (Upper left panel) $\pi+\rho$ meson-exchange tensor force on top of the usual Woods-Saxon potential. From Otsuka *et al.*, 2005. (Upper right panel) A Gogny-type calculation with the tensor force (GT2) and without it (D1S). From Otsuka, Matsuo, and Abe, 2006. (Lower panel) A zero-range tensor force calculation added to the SLy5 force. From Colò *et al.*, 2007.

Figure 31 depicts a comparison between monopole matrix elements of the zero-range tensor force of Stancu, Brink, and Flocard (1977) to those of the $\pi+\rho$ meson-exchange tensor force. For the former, the parameters obtained by a χ-square fitting to the monopole matrix elements of the $\pi+\rho$ tensor forces for the $A \approx 40$ mass region are used with actual values $(\alpha_T, \beta_T) = (64.38, 128.75)$ MeV fm^5. As shown in Fig. 31, the zero-range form for the tensor force can simulate the monopole interaction of the $\pi+\rho$ tensor force to a certain extent, but there are rather large fluctuations and deviations, especially in the case of light nuclei. We note that the present (α_T, β_T) values are close to the G-matrix ones $(\alpha_T, \beta_T) = (60, 110)$ MeV fm^5 (Brown *et al.*, 2006). For lighter nuclei, larger parameters become necessary to reproduce the monopole matrix elements of the $\pi+\rho$ tensor force, whereas the deviation is the opposite in heavy nuclei. This variation of parameters is not in accordance with the Skyrme phenomenology, where constant parameters for all nuclei are a major advantage.

Although the effect of the tensor force on the spin-orbit potential was recognized in the 1970s, the tensor term was dropped in most of the Skyrme parametrizations until recently. One of the probable reasons for this is that the inclusion of the tensor term does not lead to significant improvement in the single-particle spectra for doubly magic nuclei (Stancu, Brink, and Flocard, 1977). In addition, as pointed out by Sagawa and Colò (2014), not much attention was paid to the *evolution* of shells with successive mass numbers, likely due to the missing expectation of the shell evolution. We point out also that the meaning of the zero-range approximation of the tensor force remains to be investigated.

Following the work of Otsuka *et al.* (2005), the tensor term in the Skyrme forces was revisited in terms of the shell evolution. For instance, Brown *et al.* (2006) reported the first investigation of the effects of the inclusion of tensor forces into the shell evolution based on the Skyrme density functionals, employing empirical values $(\alpha_T, \beta_T) = (-118, 110)$ MeV fm^5. Brink and Stancu (2007) reinvestigated, after their work in Stancu, Brink, and Flocard (1977), the ESPE gaps between the proton $1h_{11/2}$ and $1g_{9/2}$ single-particle levels in Sb ($Z = 51$) isotopes as well as those between the neutron $1i_{13/2}$ and $1h_{9/2}$ single-particle levels in $N = 83$ isotones. Figures 32 and 33 depict results of various calculations on the proton $1h_{11/2}$-$1g_{9/2}$ gap in Sb isotopes. While this gap is discussed in case (5) in Sec. IV.D with Fig. 30 from the viewpoint of the V_{MU} interaction, we now survey other

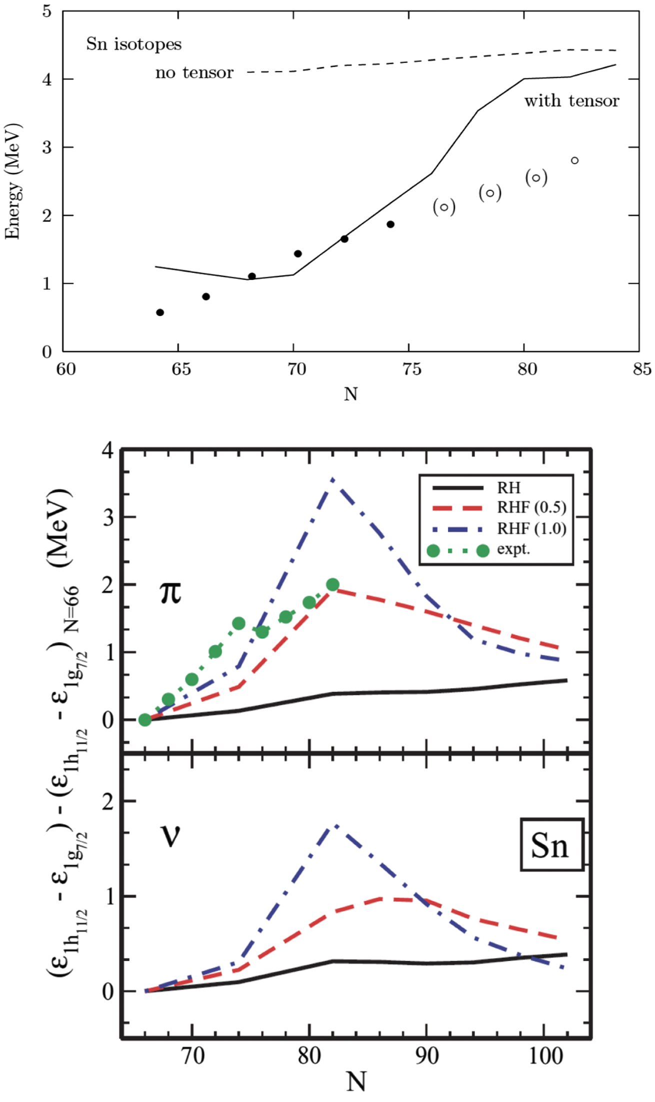

FIG. 33. The same as Fig. 32. (Upper panel) A zero-range tensor force calculation. (Lower panel) A relativistic mean-field calculation. From Brink and Stancu, 2007, and Lalazissis *et al.*, 2009.

approaches, in some of which other correlation effects are investigated. The upper panels of Fig. 32 show, as a reference, the monopole effect by the $\pi + \rho$ meson-exchange tensor force on top of the usual mean potential effect, like a Woods-Saxon potential (Otsuka *et al.*, 2005) or a Gogny-type potential (Otsuka, Matsuo, and Abe, 2006). Colò *et al.* (2007) examined this shell evolution, as shown in the lower panel of Fig. 32, confirming that the inclusion of the tensor term clearly improves the agreement with experimental data with the adopted values $(\alpha_T, \beta_T) = (-170, 100)$ MeV fm^5. The upper panel of Fig. 33 displays a similar calculation by Brink and Stancu (2007) with $(\alpha_T, \beta_T) = (-118.75, 120)$ MeV fm^5. To the present shell evolution, the proton-neutron monopole interaction, which is controlled by the β_T parameter, matters. We notice that three works (Brown *et al.*, 2006; Brink and Stancu, 2007; Colò *et al.*, 2007) use rather close values, $\beta_T = 110$, 100, and 120 MeV fm^5, respectively.

Besides the extension of Skyrme phenomenology, there was another early attempt based on the Gogny force plus Gaussian-type finite-range tensor force (Otsuka, Matsuo, and Abe, 2006) like the AV8′ interaction (Pudliner *et al.*, 1997). The result for the previously discussed shell evolution is shown in upper right panel of Fig. 32, exhibiting a good reproduction of the observed systematics. A relevant systematic study with the M3Y-type interactions was reported by Nakada (2008). Combining these works with Skyrme-based calculations, the tensor-force-driven shell evolution has been confirmed (Dobaczewski, 2006; Bartel, Bencheikh, and Meyer, 2008; Tarpanov *et al.*, 2008; Zalewski *et al.*, 2008; Zou *et al.*, 2008; Zalewski, Olbratowski *et al.*, 2009; Zalewski, Satuła *et al.*, 2009; Moreno-Torres *et al.*, 2010; Anguiano *et al.*, 2011, 2012; Dong *et al.*, 2011; Wang, Dong, and Long, 2013; Shi, 2017).

We comment on α_T values empirically determined. They cause the opposite direction of the evolution of the ones for the $\pi + \rho$ meson-exchange potential and the G-matrix results. The justification of using such negative α_T values is not clear in connection to the nucleon-nucleon forces. Regarding open problems with Skyrme-based approaches, we quote the comment "the currently used central and spin-orbit parts of the Skyrme energy density functional are not flexible enough to allow for the presence of large tensor terms" from Lesinski *et al.* (2007), and another remark, "studies of tensor terms are extended to the case with deformations for future construction of improved density functionals" from Bender *et al.* (2009). It is another open question as to what extent observed states are of a single-particle nature.

In relativistic mean-field models, π-meson degrees of freedom were taken into account in relativistic Hartree-Fock (RHF) method by its exchange contributions (Bouyssy *et al.*, 1987; Long, Giai, and Meng, 2006; Lalazissis *et al.*, 2009). The lower panel of Fig. 33 depicts an example of such calculations for the proton $1h_{11/2}$-$1g_{9/2}$ gap in Sb isotopes, presenting the tensor-force effect within the relativistic framework and the more explicit treatment of a π meson in contrast to Skyrme zero-range tensor force. Contributions from the ρ meson were found to cure the pseudoshell closures at N or $Z = 58$ and 92, leading to realistic subshell closure at 64 (Long *et al.*, 2007). In recent RHF models, density-dependent meson-nucleon couplings (Long, Giai, and Meng, 2006; Long *et al.*, 2007) or softened parametrized couplings (Lalazissis *et al.*, 2009) are adopted, which results in smaller effects of tensor forces from π or $\pi + \rho$ meson exchanges compared to nonrelativistic models (Liang, Van Giai, and Meng, 2008; Lalazissis *et al.*, 2009). Inclusion of many-body correlations beyond RHF + RPA is still in progress (Litvinova and Ring, 2006; Litvinova, 2016) and left to future investigations.

F. Contributions from the two-body *LS* force

The two-body *LS* (2b-*LS*) force is another substantial source of the monopole interaction. Although it was proposed by Elliott and Lane (1954) based on an earlier work (Blanchard and Avery, 1951), its monopole component has never appeared explicitly in the literature. We sketch its major monopole features here with more detailed discussions presented in Sec. S5 of the Supplemental Material (364).

The monopole matrix elements of the 2b-*LS* force contribute, in many cases, to the spin-orbit splitting in the usual sense. Schematic explanations on their basic properties are shown in Sec. S5 of the Supplemental Material (364), and the obtained characteristic features are listed here.

(1) The monopole interaction from the 2b-*LS* force turns out to be consistent with the usual one-body spin-orbit splitting [see, e.g., Bohr and Mottelson (1969)] in many cases, as discussed soon.

(2) A schematic semiclassical picture can be drawn for the intuitive understanding of the general and basic properties of the 2b-*LS* monopole interaction; see Fig. S2 in the Supplemental Material (364). The usual one-body spin-orbit interaction [see Bohr and Mottelson (1969)] includes the radial derivative of the density $\partial\rho/\partial r$, with ρ and r being the nucleon density and the distance from the center of the nucleus, respectively. The present picture leads us to an explanation of this dependence in terms of the difference between the monopole contributions from nucleons inside r and those from nucleons outside r.

(3) Based on this feature, a standard value for each 2b-*LS* monopole matrix element can be introduced; see the text with Eq. (S49) in the Supplemental Material (364). The actual values of the 2b-*LS* monopole matrix elements are not far from the corresponding standard values in many cases. This property may be related to the empirical systematics suggested by Mairle (1993).

(4) Sizable deviations are found in some cases, however. Among them, the coupling between an s and a p orbit can be quite strong with a large magnitude of the monopole matrix element; see Fig. S3 in the Supplemental Material (364), for example. This anomaly can be explained in a simple quantum mechanical manner based on the range of the 2b-*LS* force and the relative motion of two interacting nucleons, a robust effect.

Although this effect has been presented orally since 2004, the first publication of one of its outcomes was as recent as Suzuki and Otsuka (2008), where a notable enlargement of the proton $1p_{3/2}$-$1p_{1/2}$ splitting due to neutrons in the $2s_{1/2}$ orbit was shown as a consequence of the 2b-*LS* force; see Fig. 1 of Suzuki and Otsuka (2008) and the relevant text. Another example was presented by Burgunder *et al.* (2014) for the effect of the proton $2s_{1/2}$ occupation on the neutron $2p_{3/2}$-$2p_{1/2}$ splitting in comparison to experiment, as is discussed in Secs. VI.A.7 and VI.A.8. A trend consistent with the present effect can be seen in, for instance, the spin-tensor decomposition in Sec. V.B.

(5) In some other cases, the sign of the monopole interaction can be the opposite of the standard one mentioned previously due to the radial wave functions; see Fig. S5 of the Supplemental Material (364).

(6) If two nucleons are in the same orbit, the semiclassical picture is inapplicable, and another type of large deviation occurs, for instance, between two nucleons in the same $2p_{1/2}$ orbit; see Fig. S6 of the Supplemental Material (364). This case is interesting and important. In fact, the monopole matrix element represents the whole interaction for two neutrons in the $2p_{1/2}$ orbit, and the tensor and 2b-*LS* forces produce strong repulsion [see Figs. 22(c) and 35(b), and Fig. S6 of the Supplemental Material (364)]. This feature lowers the 2^+ level of ^{54}Ca discussed in Sec. IV.D.4 by reducing the pairing gap and thereby shifting the ground-state energy upward. Thus, the actual $N = 34$ shell gap is likely larger than what is expected from the actual 2^+ level. The present repulsive effect also gives a natural explanation to the unusually weak or even repulsive value of the $2p^2_{1/2}$ pairing matrix element mentioned by Brown (2013). While the tensor-force effect was suggested earlier (Otsuka, Suzuki, Honma *et al.*, 2010), another argument was given by Brown (2013).

We now look into the shell structure of ^{15}C and ^{17}O as an example of notable contributions of the 2b-*LS* monopole interaction. Although this case was discussed in Sec. III.G, we revisit it. Figure 9 depicts the inversion between neutron $2s_{1/2}$ and $1d_{5/2}$ orbits between ^{15}C and ^{17}O, and Fig. 34(a) shows how the monopole matrix elements work for this inversion. We now illustrate the origins of those monopole matrix elements in Fig. 34 in terms of the tensor, 2b-*LS*, and central forces between protons and neutrons. Here it is assumed that from ^{15}C to ^{17}O, the proton $1p_{1/2}$ orbit is fully occupied, and the last neutron is in either the $2s_{1/2}$ or $1d_{5/2}$ orbit. Figure 34(a) displays how the neutron $2s_{1/2}$ orbit is shifted relative to the $1d_{5/2}$ orbit in going from ^{15}C to ^{17}O in this genuine single-particle limit.

Figure 34(b) shows a related analysis. This is similar to Fig. 34(a), but the contributions of the tensor and 2b-*LS* forces and the rest of Hamiltonian are shown with respect to the shell-model eigenstates obtained by the diagonalization of the Hamiltonian. These energy levels can be calculated by recently developed shell-model Hamiltonians, SFO-tls introduced in Suzuki and Otsuka (2008) and YSOX introduced in Yuan *et al.* (2012). The latter is taken in Fig. 34(b), while the former gives a similar result. The contributions here refer to the expectation values. The tensor and 2b-*LS* values are about 80% of the corresponding values in Fig. 34(a), which appear to be very similar to the probability of the lowest configuration in the shell-model full wave functions of ^{17}O. Thus, the discussions in terms of the monopole matrix elements and ESPEs are further proven to be sensible. On the other hand, the contributions from the central force in Fig. 34(a) is reduced significantly in the rest of Fig. 34(b). Here the rest includes not only effects of the central force but also effects of the (bare) single-particle energies due to excitations from lower to higher orbits. It is clear that various correlations due to the remainder decrease the raising of the $1/2^+_1$ level. The general aspect of this feature is of interest. The importance of noncentral forces is thus confirmed in the case shown in Fig. 34, which is consistent with earlier remarks (Millener and Kurath, 1975).

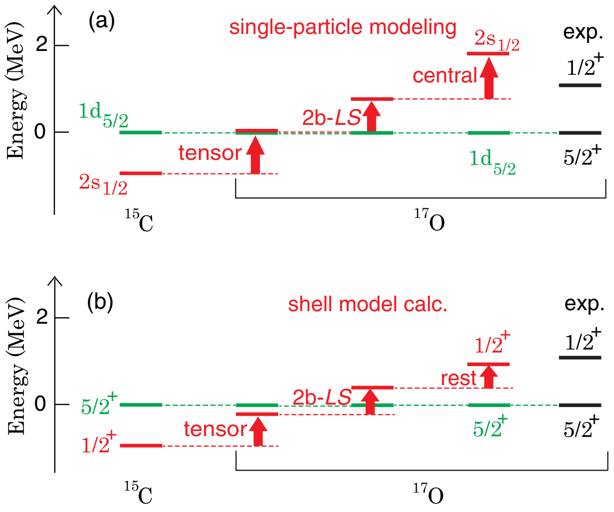

FIG. 34. (a) Energy of the neutron $2s_{1/2}$ orbit relative to the $1d_{5/2}$ orbit in ^{15}C and ^{17}O, calculated within the single-particle scheme using the $V_{\rm MU}$ interaction plus the M3Y 2b-*LS* force (see the text). Contributions from the tensor, 2b-*LS*, and central forces are decomposed. The changes are added to the experimental $1/2^+_1$ level placed relative to the experimental $5/2^+_1$ level. The experimentally observed level of ^{17}O is shown at the far right. (b) Analysis similar to (a) in terms of the shell-model calculation with the YSOX (Yuan *et al.*, 2012) interaction. Some expectation values obtained by the YSOX calculation corresponding to (a) are shown with respect to the shell-model eigenstates. See the caption for (a).

V. RELATED FEATURES OF NUCLEAR FORCES

Here we discuss some features of nuclear forces related to the shell evolution.

A. Renormalization persistency of the tensor force

The effects of the tensor force have been discussed already in terms of the $\pi + \rho$-meson-exchange potential. This potential is derived in the free space, and one has to investigate the changes due to various renormalization procedures for the short-range repulsion and the in-medium corrections. This study was done by Otsuka, Suzuki, Honma *et al.* (2010) and Tsunoda *et al.* (2011), who suggest that the changes are quite small for the tensor force, referred to as *renormalization persistency*.

An example is shown in Fig. 35 (Otsuka, Suzuki, Honma *et al.*, 2010), where the AV8′ interaction (Pudliner *et al.*, 1997) was used as the starting nuclear force in the free space. A low-momentum interaction $V_{\mathrm{low}\,k}$ (Bogner, Kuo, and Schwenk, 2003) was derived in order to treat short-range

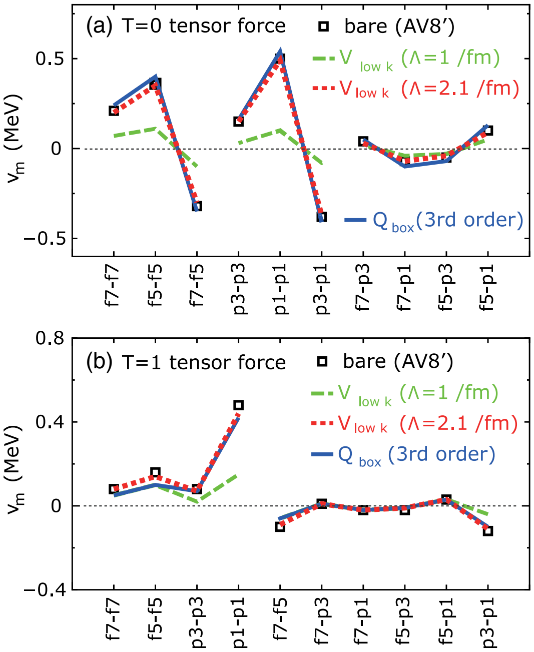

FIG. 35. Monopole matrix elements from tensor forces in the AV8′ interaction (Pudliner *et al.*, 1997), in low-momentum interactions obtained from the AV8′, and in the third-order Q-box interaction for (a) $T = 0$ and (b) $T = 1$. From Otsuka, Suzuki, Honma *et al.*, 2010.

correlations, and the third-order Q-box calculation with folded diagram corrections (Hjorth-Jensen, Kuo, and Osnes, 1995) was performed in order to include medium effects like core polarization.

The spin-tensor decomposition has been carried out for decades (Elliott *et al.*, 1968; Kirson, 1973; Klingenbeck *et al.*, 1977; Yoro, 1980; Brown *et al.*, 1988; Osnes and Strottman, 1992) in order to extract the tensor-force component. Here the spin-tensor decomposition serves as a useful classification technique of a given two-body interaction into several pieces, such as the scalar-coupled (central force), axial-vector-coupled [two-body LS (spin-orbit) force], and tensor-coupled spin components.

We outline this now. A given two-body interaction can be rewritten in general as

$$V = \sum_{k=0,1,2} V_k = \sum_{k=0,1,2} U^k \cdot X^k, \tag{72}$$

where U^k and X^k are tensor operators of rank k in the coordinate and spin spaces, respectively. One can thus uniquely extract the LS-coupled matrix elements of each k component:

$$\begin{aligned}
&\langle n_a \ell_a n_b \ell_b LSJT | V_k | n_c \ell_c n_d \ell_d L'S'JT \rangle \\
&\quad = (-1)^J (2k+1) \begin{Bmatrix} L & S & J \\ S' & L' & k \end{Bmatrix} \\
&\qquad \times \sum_{J'} (-1)^{J'} (2J'+1) \begin{Bmatrix} L & S & J' \\ S' & L' & k \end{Bmatrix} \\
&\qquad \times \langle n_a \ell_a n_b \ell_b LSJ'T | V | n_c \ell_c n_d \ell_d L'S'J'T \rangle .
\end{aligned} \tag{73}$$

The $k = 0$, 1, 2 matrix elements correspond, as mentioned previously, to the central force, spin-orbit (plus antisymmetric spin-orbit) force(s), and tensor force, respectively.

These are all possible components for interactions with the dependence on relative coordinates. If dependence on the center-of-mass coordinate is allowed for some reason, other terms like antisymmetric LS appear. Since the shells being considered are full harmonic oscillator shells containing all spin-orbit partners, this spin-tensor decomposition is possible. We note that the tensor component here is obtained from a given interaction and can differ from the one from the $\pi + \rho$-meson-exchange potential. We will see that this turns out to be a minor difference in the present discussion with realistic interactions.

Figure 35 displays monopole matrix elements thus calculated for $T = 0$ and 1 in the pf shell, starting with the AV8′ interaction (Pudliner *et al.*, 1997) and varying the cutoff parameter in the $V_{\mathrm{low}\,k}$ process. For the usual value 2.1 fm^{-1}, the result is very close to those obtained directly from the bare AV8′ tensor force.

The feature in which a nuclear-force component remains unchanged to a good extent by the renormalization processes has been referred to as *renormalization persistency* (Tsunoda *et al.*, 2011). Renormalization persistency was particularly well studied for the monopole interaction of the tensor force with a combination of the shell, the original interaction, and the renormalization methods. Such studies, not only the earliest one (Tsunoda *et al.*, 2011) but also more recent ones with χEFT forces (Yoshida, 2017), indicate that the tensor force fulfills the renormalization persistency at least at the level of the monopole interaction. The renormalization persistency therefore provides us with a good rationale to discuss general features of the monopole effects of the tensor force in terms of the $\pi + \rho$-meson-exchange potential, as has been done so far.

B. Spin-tensor decomposition of shell-model interaction

The spin-tensor decomposition discussed previously is a useful tool to analyze the amount of the tensor and other components contained in the shell-model interaction. Smirnova *et al.* (2010, 2012) applied the spin-tensor decomposition technique (Elliott *et al.*, 1968; Kirson, 1973; Klingenbeck *et al.*, 1977; Yoro, 1980; Brown *et al.*, 1988; Osnes and Strottman, 1992) to a realistic interaction for the sd-pf shell (Nowacki and Poves, 2009) and examined $k = 0$, 1, 2 contributions to the ESPEs in Eq. (72). Figure 36 shows the evolution of the neutron effective single-particle energies with protons occupying $d_{5/2}$ ($Z = 8$–14), $s_{1/2}$ ($Z = 14$–16), and $d_{3/2}$ ($Z = 16$–20). It is demonstrated that the spin-orbit splittings, especially those of $f_{7/2}$-$f_{5/2}$ and $d_{5/2}$-$d_{3/2}$, are changed notably by the tensor component, and that their increase from $Z = 16$ to 20 and their decrease from $Z = 8$ to 14 follow the path we have presented already, which can be regarded as a confirmation of the appropriateness of the empirically fitted shell-model interaction used by Smirnova *et al.* (2010, 2012). The tensor component also accounts for nearly half the reduction of the $N = 20$ shell gap (i.e., the $d_{3/2}$-$f_{7/2}$ gap) when going from $Z = 14$ to 8. These behaviors are in accordance with what the V_{MU} interaction gives (Otsuka, Suzuki, Honma *et al.*, 2010); see the left panel of Fig. 47.

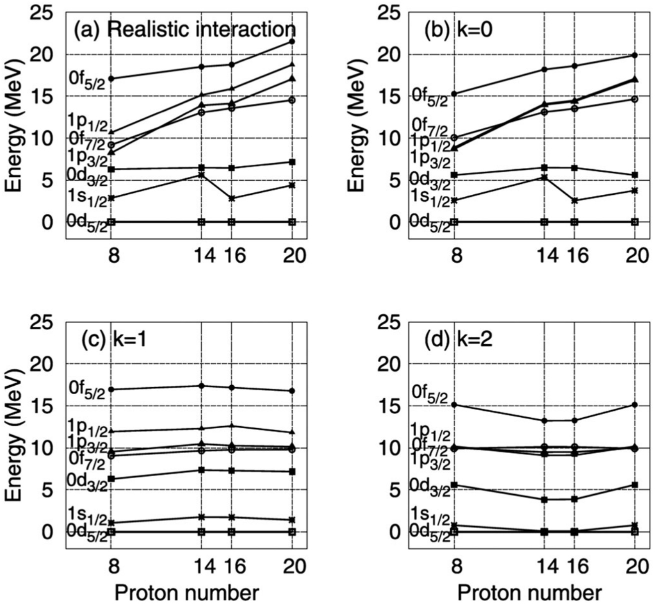

FIG. 36. (a) Neutron effective single-particle energies of the SDPF-U interaction (Nowacki and Poves, 2009) and their (b) $k = 0$, (c) $k = 1$, and (d) $k = 2$ contributions with increasing proton number. From Smirnova *et al.*, 2010.

C. Fujita-Miyazawa three-body force and the shell evolution

We now turn to three-nucleon forces (3NF), shedding light on their contributions to the shell evolution. Three-nucleon forces were introduced in the pioneering work of Fujita and Miyazawa (1957) (FM). One of the main sources of 3NF is the fact that nucleons are composite particles. In fact, the FM 3N mechanism is due to one nucleon virtually exciting a second nucleon to the Δ(1232 MeV) resonance, which is deexcited by scattering off a third nucleon; see Fig. 37(e).

The quantitative role of FM 3N interactions was pointed out in *ab initio* calculations for $A \leq 12$ by the Green's function Monte Carlo (GFMC) method (Pudliner *et al.*, 1997; Pieper and Wiringa, 2001; Pieper, 2005) and by the no-core shell-model (NCSM) method (Navrátil, Vary, and Barrett, 2000a, 2000b; Navrátil *et al.*, 2007). These works were reviewed by Barrett, Navrátil, and Vary (2013) and Carlson *et al.* (2015), respectively. Three-nucleon interactions arise naturally also in the chiral effective field theory (χEFT) [see the review by Hammer, Nogga, and Schwenk (2013)] as we discuss in Sec. V.D.

We focus here on the monopole effect from the FM 3NF with the actual example of the oxygen anomaly (Otsuka, Suzuki, Holt *et al.*, 2010). We first sketch the mechanism for the monopole effect presented by Otsuka, Suzuki, Holt *et al.* (2010). Figure 37(a) depicts the leading contribution to NN forces due to Δ-resonance excitation, induced by the exchange of π mesons between nucleons. Because this is a second-order perturbation approach, its contribution to the monopole interaction is attractive. The same process changes the SPE of the state j, m, as illustrated in Fig. 37(b), by the Δ–nucleon-hole loop where the initial nucleon in the state j, m is virtually excited to another state j', m'. This lowers the energy of the state j, m. However, if another nucleon of the same kind occupies the state j', m' as shown in Fig. 37(c), this process is forbidden by the Pauli exclusion principle. The corresponding contribution must be subtracted from the SPE change. This is taken into account by the inclusion of the exchange diagram shown in Fig. 37(d), where the nucleons in the intermediate state are exchanged, and this leads to the exchange of the final (or initial) labels j, m and j', m'. Because this process reflects a cancellation of the lowering of the SPE, the contribution from Fig. 37(d) has to be repulsive. Finally, we can rewrite Fig. 37(d) as the FM 3N force of Fig. 37(e), where the middle nucleon is summed over all nucleons in the core. We thus obtain robustly repulsive monopole interactions between the valence nucleons originating in the FM 3NF. It is clear that only the monopole component is produced by this particular process, without touching on multipole components.

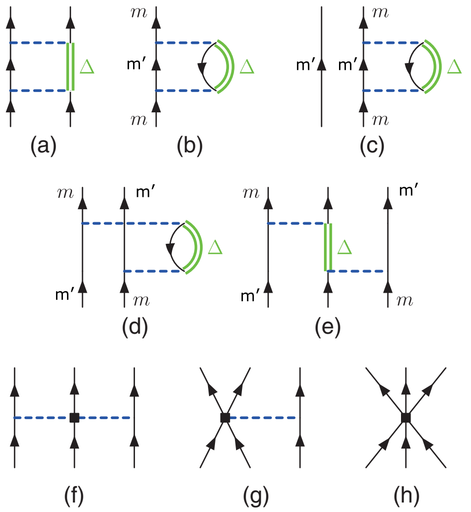

FIG. 37. Processes involved in the discussion of 3N forces and their contributions to the monopole components of the effective interactions between two valence neutrons. The solid lines denote nucleons, the dashed lines denote π mesons, and the thick lines denote Δ excitations. Nucleon-hole lines are indicated by downward arrows. (a) The leading contribution to NN forces due to Δ-resonance excitation, and (b) the change of SPE of the state j, m by the process (a). The process (b) is forbidden with another nucleon with the same j', m', as shown (c), which requires the inclusion of the exchange diagram (d), which is equivalent to the FM 3N force (e). The leading χEFT 3N forces include (f) the long-range two-π-exchange parts, which take into account the excitation to a Δ and other resonances, plus shorter-range (g) one-π-exchange and (h) 3N contact interactions. From Otsuka, Suzuki, Holt *et al.*, 2010.

Figure 38 shows, as an example, neutron ESPEs of the oxygen isotopes starting from the stable ^{16}O to heavier ones with more neutrons. The ESPEs calculated (Otsuka, Suzuki, Holt *et al.*, 2010) with NN interactions in the G-matrix formalism (Hjorth-Jensen, Kuo, and Osnes, 1995). A similar result with χEFT forces is discussed in Sec. V.D. The $d_{3/2}$ ESPE decreases rapidly as neutrons occupy the $d_{5/2}$ orbit and remains well bound from $N = 14$ on. This leads to bound oxygen isotopes out to $N = 20$ and puts the neutron dripline incorrectly beyond ^{28}O.

The changes in the ESPE evolution due to the addition of FM 3NF are included in the left panel of Fig. 38. The repulsive

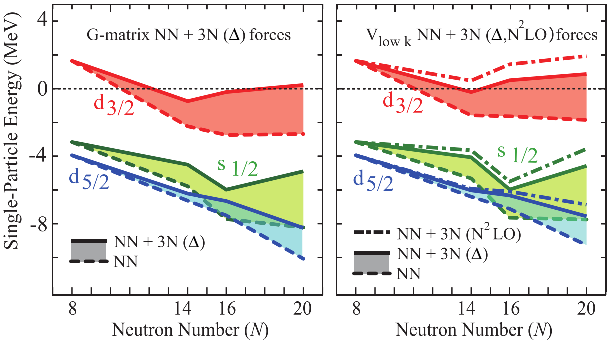

FIG. 38. ESPE of neutron $1d_{5/2}$, $2s_{1/2}$, and $1d_{3/2}$ orbitals measured from the energy of ^{16}O as a function of N. The ESPEs calculated (left panel) from a G matrix and (right panel) from low-momentum interactions $V_{\mathrm{low}\,k}$ are shown. The changes due to 3N forces based on Δ excitations are highlighted by the shaded areas. Adapted from Otsuka, Suzuki, Holt et al., 2010.

FM 3N contributions become significant with increasing N. Figures 22(g) and 22(h) indicate that monopole components are modified to be more repulsive from G matrix to SDPF-M in the sd shell, except for the case with $j = j' = d_{3/2}$. Since SDPF-M reproduces the experimental data rather well, this general trend seems to suggest that a good fraction of the effects of the FM 3NF, and perhaps other 3NFs in general, is included empirically in shell-model interactions. It was argued by Zuker (2003, 2005) that an effective NN interaction was nearly perfect and that any deviation suggested by experiment should be due to some three-body force.

The ground-state energies of oxygen isotopes are shown in Fig. 39, where the 3NF changes them to be very close to experimental values and places the dripline correctly. Figure 38 shows the key role of the FM 3NF for new magic numbers $N = 14$ between the $1d_{5/2}$ and $2s_{1/2}$ orbits (Stanoiu et al., 2004), and $N = 16$ between the $2s_{1/2}$ and $1d_{3/2}$ orbits (Ozawa et al., 2000; Hoffman et al., 2008; Kanungo et al., 2009).

D. *Ab initio* approaches to nuclear structure

We discuss *ab initio* approaches to the nuclear structure here. As there have been many activities regarding this topic recently, a devoted review is needed, and we mainly discuss certain recent outcomes related to the shell and structure evolutions in exotic nuclei. Naturally, few-body systems have been studied in *ab initio* ways, as reviewed by Leidemann and Orlandini (2013). The GFMC (Pudliner et al., 1997; Pieper and Wiringa, 2001; Pieper, 2005; Carlson et al., 2015) and NCSM (Navrátil, Vary, and Barrett, 2000a, 2000b; Navrátil et al., 2007; Barrett, Navrátil, and Vary, 2013) calculations were started around 2000, showing that the structure of light nuclei (up to $A \sim 10$) can be described well from the nucleon-nucleon forces (2NF) determined by the nucleon-nucleon scattering combined with the 3NF appropriately determined. In the meantime, the χEFT (van Kolck, 1994; Epelbaum et al., 2002) was developed to construct nuclear forces in a systematic expansion from leading to successively higher orders (Entem and Machleidt, 2003; Epelbaum, 2006; Epelbaum, Hammer, and Meißner, 2009), which are visualized by diagrams showing nucleons interacting via π exchanges and shorter-range contact terms; see the review by Machleidt and Entem (2011). The interactions from the χEFT are modified to be applicable to low-momentum phenomena by using the low-momentum interactions $V_{\mathrm{low}\,k}$ (Bogner, Kuo, and Schwenk, 2003) or by the similarity renormalization method (SRG) (Bogner, Furnstahl, and Perry, 2007).

The right panel of Fig. 38 displays the ESPE calculated from chiral low-momentum interactions $V_{\mathrm{low}\,k}$, including the changes due to the leading [next-to-next-to-leading order (N^{2}LO)] 3N forces in χEFT (van Kolck, 1994; Epelbaum et al., 2002) [see Figs. 37(f)–37(h)], as well as changes due to Δ excitations (Bogner et al., 2009). The second from left panel of Fig. 39 shows the ground-state energy of oxygen isotopes calculated with these interactions, depicting good agreement with experiment (Otsuka, Suzuki, Holt et al., 2010).

A similar shell evolution is seen in exotic Ca isotopes, where the inclusion of 3NF effects raises ESPE's of the pf-shell neutron orbits (Holt et al., 2012; Otsuka and Suzuki, 2013).

The coupled-cluster (CC) calculations (Hagen et al., 2008, 2009, 2010) started with the 2NF obtained as the next-to-next-to-next-to-leading order (N^{3}LO) χEFT interaction. The N^{2}LO 3NF was included in the CC calculation (Hagen et al., 2012a, 2012b) for O and Ca isotopes, with results consistent with those just mentioned. Figure 40 shows the 2_1^+ level of Ca isotopes calculated by the CC method (Hagen et al., 2012b),

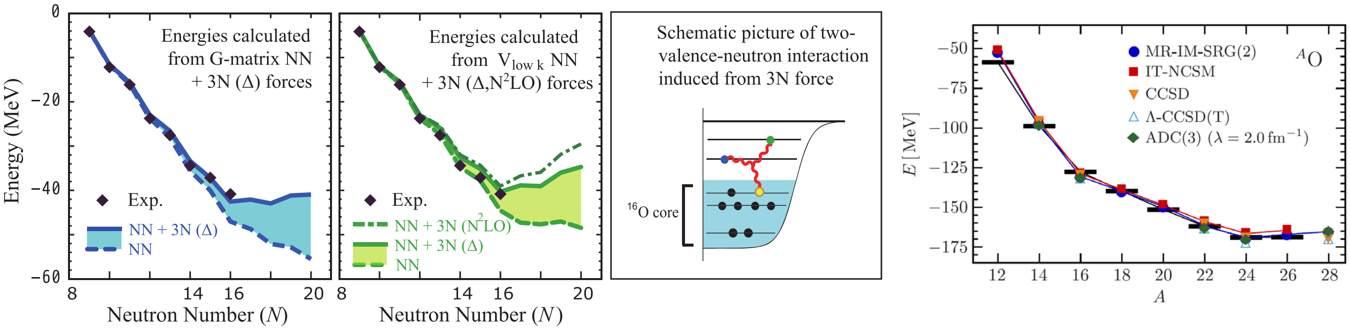

FIG. 39. (Left and second from left panels) Ground-state energies of oxygen isotopes including processes shown in the second from right panel. Adapted from Otsuka, Suzuki, Holt et al., 2010. (Right panel) The ground-state energies calculated in several χEFT approaches (Hergert et al., 2016). From Hergert et al., 2016.

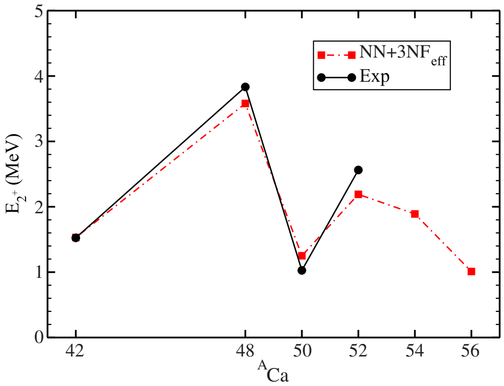

FIG. 40. 2_1^+ level of Ca isotopes calculated by the CC method. From Hagen *et al.*, 2012b.

showing results consistent with the shell evolution in Ca isotopes discussed in Sec. IV.D.4, including the ^{54}Ca 2^+ level; see Fig. 29.

The 3NF is converted into an effective 2NF by the normal ordering combined with a reference state, which is a Fermi gas or Hartree-Fock state. The in-medium SRG (IM-SRG) was introduced and developed by Tsukiyama, Bogner, and Schwenk (2011, 2012), Hergert, Binder *et al.* (2013), Hergert, Bogner *et al.* (2013), and Hergert *et al.* (2014) [see the review by Hergert *et al.* (2016)] to renormalize in-medium effects into effective interactions.

A frequently used interaction (called *A* for brevity) was introduced by Hebeler *et al.* (2011) using the SRG transformation of the N^{3}LO 2NF of Entem and Machleidt (2003) with the cutoff parameter 500 MeV$/c$ combined with the N^{2}LO 3NF where the parameters c_D and c_E [shown in Figs. 37(g) and 37(h), respectively] are fitted to the triton binding energy and the ^{4}He charge radius. This set *A* interaction was shown to produce larger radii of proton distribution by the CC calculations (Hagen *et al.*, 2016). Since then, this interaction has been used in many works: for magic nuclei (Hagen, Jansen, and Papenbrock, 2016), for *sd*-shell nuclei (Simonis *et al.*, 2016), and for density saturation in finite nuclei (Simonis *et al.*, 2017). The CC calculations show larger charge radii of heavy Ca isotopes, which is consistent with recent measurements made up to ^{52}Ca (Ruiz, Garcia *et al.*, 2016).

There is another frequently used interaction (called *B* for brevity) introduced by Roth *et al.* (2012), where the 3NF is different from the set *A* in a local form with the cutoff parameter 400 MeV$/c$. This set *B* interaction was used by Binder *et al.* (2013, 2014), Hergert *et al.* (2014), and Tichal *et al.* (2014) for ground-state properties of Ca, Ni, Sn, etc. The self-consistent Green's function theory also provided ground-state energies (Soma, Duguet, and Barbieri, 2011; Soma *et al.*, 2014) and, furthermore, the ESPEs (Cipollone, Barbieri, and Navrátil, 2013, 2015), as shown in Fig. 41, which indicates results consistent with those shown in Sec. V.C. We point out that the ESPE in Cipollone, Barbieri, and Navrátil (2013, 2015), based on the formulation by Baranger (1970), is consistent with the ESPE discussed in this article, as illustrated in Sec. III.F.

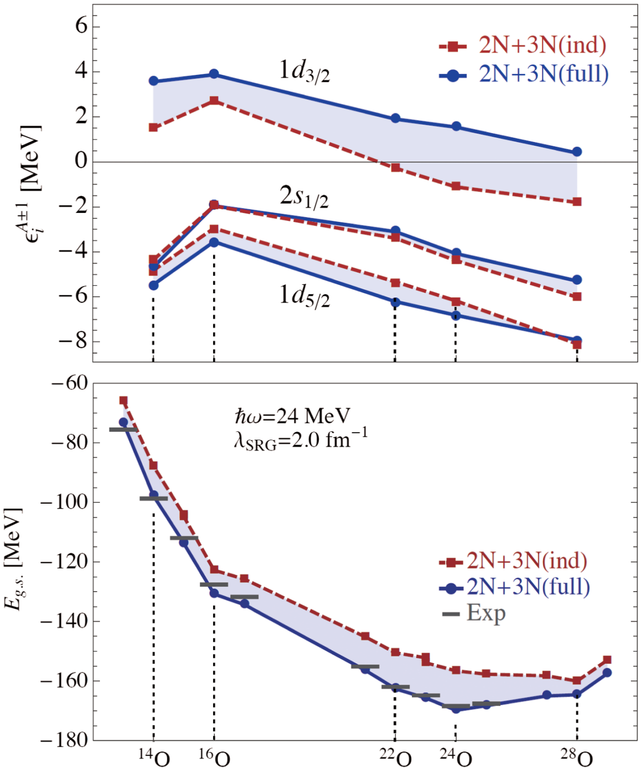

FIG. 41. (Upper panel) ESPEs of neutrons calculated by Cipollone, Barbieri, and Navrátil (2013) at subshell closures of oxygen isotopes. (Lower panel) Similarly calculated ground-state energies compared to experiment (bars). From Cipollone, Barbieri, and Navrátil, 2013.

The procedures with the sets *A* and *B* can be summarized as follows.

1. The Hamiltonian consisting of N^{3}LO 2NF and N^{2}LO 3NF is obtained from the χEFT. For set *B*, the values of the parameters c_D and c_E are fitted to the triton and ^{4}He properties by performing a few-body calculation.
2. Short-range correlations are processed by the SRG, truncated up to three-nucleon terms. These are 2NF and 3NF for set *A*, with c_D and c_E fitted in the same way at this stage.
3. A HF calculation is carried out with 2NF and 3NF thus derived or fitted as the reference state(s).
4. The Hamiltonian is truncated up to two-nucleon terms by the normal ordering with the reference state(s).
5. With such two-nucleon interactions, the CC, IM-SRG, MBPT, etc. are carried out.

The right panel of Fig. 39 shows that *ab initio* calculations based on the χEFT reproduce the ground-state energies of oxygen isotopes well (Hergert *et al.*, 2016), which is consistent with other work in the left panels. In going to proton-neutron open-shell nuclei, further developments are made to obtain the shell-model interactions so that their eigenvalues are calculated. A shell-model interaction was calculated by Lisetskiy *et al.* (2008) based on the NCSM. With the IM-SRG (Stroberg *et al.*, 2016, 2017; Simonis *et al.*, 2017), the reference state was improved so that two reference states are considered with the ensemble normal ordering (ENO) in going through an open shell taking a weighted average.

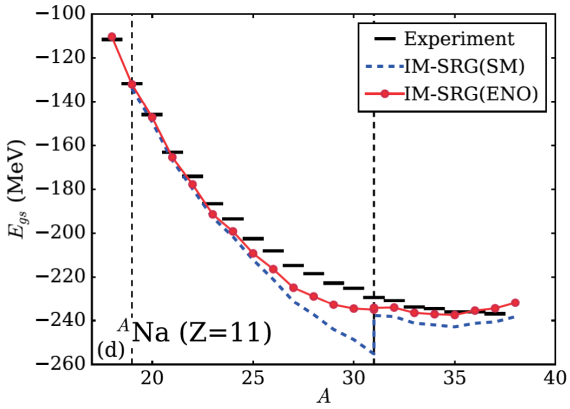

FIG. 42. Ground-state energies of Na isotopes calculated with IM-SRG (SM). The IM-SRG (SM) curves use a core reference, while the curves labeled IM-SRG (ENO) use an ensemble reference. From Stroberg *et al.*, 2017.

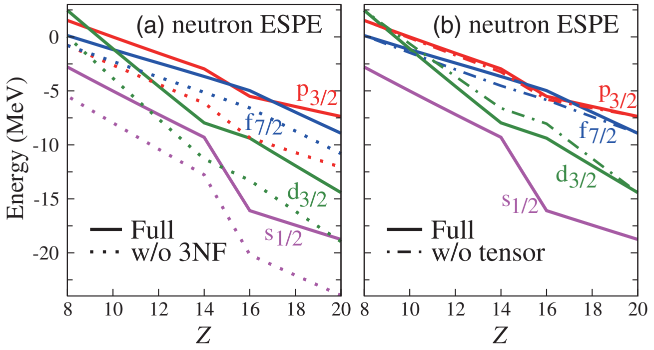

FIG. 44. ESPEs of $N = 20$ isotones for neutrons obtained in the normal filling scheme. The solid (dotted) lines in (a) show the case with (without) three-nucleon forces, while the solid (dot-dashed) lines in (b) represent the case with (without) the tensor component. From Tsunoda *et al.*, 2017.

Figures 42 and 43 display, respectively, the ground-state energies (Stroberg *et al.*, 2017) and the two-neutron separation energies (Simonis *et al.*, 2017) of Na isotopes. The agreement with experiment was improved, with certain differences between the two calculations. The difference is mainly due to the different interactions sets A and B. In the latter, the experimental values are reproduced up to $N \sim 16$, but some deviations arise over the neutron magic number 20, probably because of substantial mixings of intruder configurations.

It is worth mentioning that the radius is often predicted to be too small in *ab initio* calculations, but this problem was avoided by the so-called $\mathrm{N^2LO_{sat}}$ interaction, where the parameters are taken only up to the $\mathrm{N^2LO}$ being fitted to properties of heavier nuclei such as ^{14}C and ^{16,23,24,25}O (Ekström *et al.*, 2015).

Despite these significant improvements in *ab initio* approaches, in general, the discrepancy with experiment remains at present. For instance, the extra binding due to intruder configurations may not be reproduced well, as discussed for Figs. 42 and 43. On the other hand, this is one of the most crucial features of exotic nuclei, as emphasized also in Sec. VI.A. As a possible breakthrough, the extended Kuo-Krenciglowa (EKK) method was proposed and developed (Takayanagi, 2011a, 2011b; Tsunoda, Takayanagi *et al.*, 2014). The EKK method is one of the many-body perturbation theories (MBPTs). The other MBPT calculations have a possibility of divergence when applied to two or more major shells, but the EKK method is free from this difficulty. As two major shells merge or the shell gap becomes smaller in exotic nuclei rather often, it is crucial to include two or more shells properly.

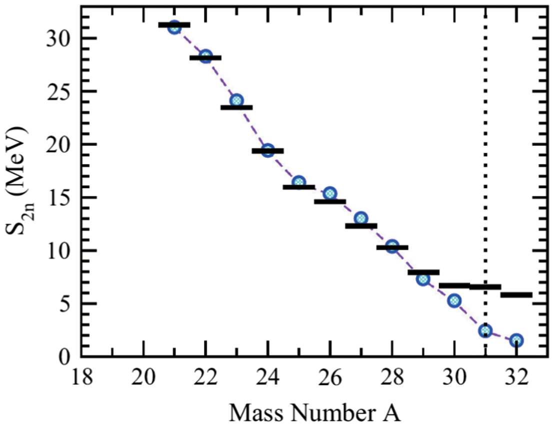

FIG. 43. The two-neutron separation energies of Na isotopes calculated with IM-SRG. From Simonis *et al.*, 2017.

The EEdf1 interaction was obtained for the *sd*-*pf* shell from a χEFT NN interaction at $\mathrm{N^3LO}$ with the EKK treatment of in-medium effects and from the FM 3NF; see Sec. V.C and Tsunoda, Takayanagi *et al.* (2014). Figure 44 shows ESPE calculated from the EEdf1 interaction for $N = 20$ isotones as a function of Z. Figure 44(a) shows the ESPEs obtained by the full calculation and those obtained after removing the FM 3NF. One finds that this 3NF shifts the SPEs upward, and that the shifts become larger as Z increases. Figure 44(b) depicts the ESPEs obtained by the full calculation and those obtained after removing the tensor component from the EEdf1 interaction. Although the magnitude of the tensor-force effects is smaller than that of the 3NF as a whole, the tensor-force effects are not monotonic and produce more rapid changes in the shell structure in contrast to the 3NF effects. We note that the tensor component is quite minor in the effective NN interaction originating in the FM 3NF. In those calculations, although the one-body SPEs are fitted at certain nuclei, the evolution of the ESPEs is given by the interaction thus derived, and the resulting changes as a function of Z or N have nothing to do with the fit. In this sense, Figs. 44(a) and 44(b) confirms the shell evolution at $N = 20$, which appears to be consistent with earlier results discussed in Sec. VI.A.4. Some results of the EEdf1 interaction will be presented in Sec. VI.A.

VI. EXAMPLES OF STRUCTURAL CHANGE MANIFESTED IN EXPERIMENTAL OBSERVABLES

We discuss here how theoretical results are confronted with a variety of experimental measurements. In such cases, both shell-evolution effects and other many-body correlations arise and can mutually affect each other. For our examples, we explain the mechanisms of shell evolution at play.

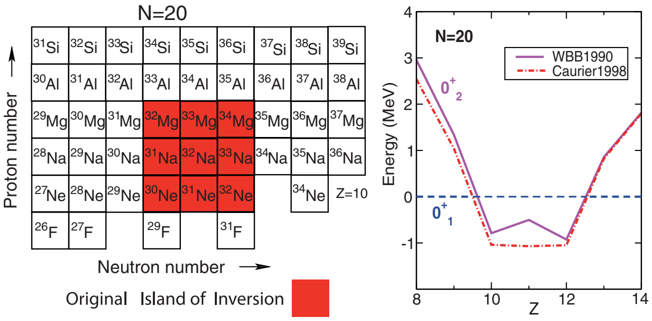

FIG. 45. (Left panel) Part of the Segrè chart around the IoI. The red area indicates its original picture as of Warburton, Becker, and Brown (1990). Now the IoI has extended much further (see the text). (Right panel) Relative energy of the lowest normal and lowest neutron $2p$-$2h$ intruder 0^+ states, resulting from diagonalizing in a separate subspace. Adapted from Warburton, Becker, and Brown, 1990, and Caurier *et al.*, 1998.

A. Measuring the key indicators of shell evolution in the island of inversion

Since short-lived "exotic" nuclei cannot be made into targets, measurements of their properties have to start from an ion beam which is subjected to an in-beam measurement in inverse kinematics, implanted into an active or passive stopper to observe its decay, or manipulated for ion trapping or laser spectroscopic approaches, for example.

The first challenge of any experiment with short-lived, exotic nuclei is their production. Today, a broad range of rare isotopes is available for experiments in the form of ion beams. Two main production and separation mechanisms have emerged as the workhorse techniques in rare-isotope beam production and are employed in nuclear physics laboratories around the world.

- Beams of short-lived nuclei are produced and separated *in flight* and are directly used for experiments (in-flight separation).
- Exotic nuclei are produced and thermalized in a thick target, extracted, ionized, transported, or reaccelerated (isotope separation on-line).

The production strategies for rare-isotope beams and the different types of rare-isotope facilities around the world were recently reviewed by Blumenfeld, Nilsson, and Duppen (2013).

Here we use the example of the "island of inversion" (IoI) centered around ^{32}Na (see Fig. 45) in order to describe how typical observables are measured and interpreted as indicators of structure changes.

1. Sketch of the island of inversion

We first sketch the IoI mainly from the shell-evolution viewpoint, briefly because dedicated reviews exist (Caurier *et al.*, 2005). The IoI was named by Warburton, Becker, and Brown (1990) after earlier experimental studies had reported various anomalous features, for example, Thibault *et al.* (1975), followed by Huber *et al.* (1978), Détraz *et al.*, 1979, and Guillemaud-Mueller *et al.* (1984). It is characterized by deformation-related neutron particle-hole excitations from the sd shell into the pf shell across the $N = 20$ shell gap. Such particle-hole excitations across a shell gap are often referred to as *intruder configurations*, which can be energetically favored over the normal configurations and dominate the ground states of the nuclei in the IoI, as shown in the right panel of Fig. 45. States composed mainly of intruder configurations are called *intruder states* or *intruders*. Most of the binding-energy gains are due to the deformation from a sphere to an ellipsoid. Thus, an intruder at zero or low excitation energy implies shape coexistence with states based on spherical normal-order configurations, which is seen in many exotic nuclei.

Early theoretical studies also indicated that the ground states can be deformed for nuclei in the IoI, such as the deformed Hartree-Fock solution for ^{31}Na by Campi *et al.* (1975), and intruder shell-model ground states despite the rather constant $N = 20$ gap by Poves and Retamosa (1987). Regarding the shell evolution, so-called modified single-particle energy was introduced by Storm, Watt, and Whitehead (1983), corresponding to the present ESPE in the special case of a (sub)shell closure ± one particle; see the text around Eq. (37). Although the monopole interaction was not mentioned, this may be the first appearance of the ESPE. The changes of the neutron shell structure were then discussed by Storm, Watt, and Whitehead (1983), with some differences from the current picture.

The left panel of Fig. 46 displays the $N = 20$ shell gap of $N = 20$ isotones obtained from Warburton, Becker, and Brown (1990), with values > 5 MeV. The right panel of Fig. 46 presents ESPEs calculated from the SDPF-M interaction (Utsuno *et al.*, 1999), and the resulting $N = 20$ gap is included in the left panel of Fig. 46. The gaps now varies more, and they become as low as 2 MeV for $Z = 8$. A similar evolution of the ESPEs of the $d_{3/2}$ and $f_{7/2}$ orbits was obtained by Fukunishi, Otsuka, and Sebe (1992), where large-scale shell-model calculations were made for successful predictions. The $d_{3/2}$ ESPE changes more steeply with the SDPF-M interaction, however. This is because Fukunishi, Otsuka, and Sebe (1992) used the USD interaction, where a change was made from the G matrix (Kuo, 1967). This change appeared to be rather inappropriate (Otsuka *et al.*, 2001) and was removed for the SDPF-M interaction, resulting in a better description. This is an example of the importance of nuclear

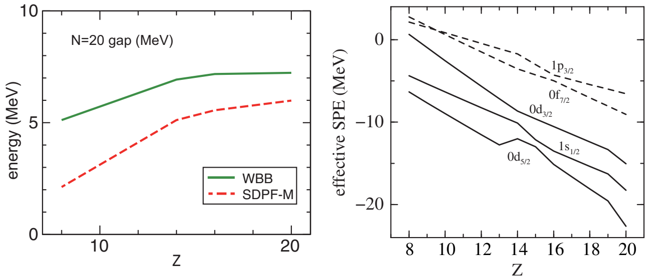

FIG. 46. (Left panel) $N = 20$ shell gap (green solid line) and from the SDPF-M interaction (red dashed line). Adapted from Warburton, Becker, and Brown, 1990, and Utsuno *et al.*, 1999, respectively. (Right panel) ESPEs of $N = 20$ isotones for neutrons obtained in the normal filling scheme from SDPF-M interaction. From Utsuno *et al.*, 1999.

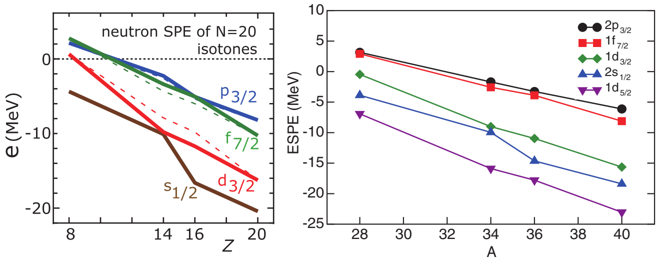

FIG. 47. ESPEs of $N = 20$ isotones for neutrons obtained in the normal filling scheme (left panel) from the V_{MU} interaction and (right panel) from the SDPF-NR interaction. From Otsuka, Suzuki, Honma *et al.*, 2010, and Caurier *et al.*, 2005, respectively.

forces to the shell evolution. This $N = 20$ gap reduction was schematically shown earlier by Heyde and Wood (1991) in terms of the proton-neutron monopole interaction of a δ-function interaction, while the obtained pattern is too monotonic partly due to the missing tensor force. The intruder states stayed higher toward $Z = 8$ in Caurier *et al.* (1998), as exhibited in the right panel of Fig. 45. Thus, although the breakdown of the $N = 20$ magicity in the IoI was commonly accepted, in the 1990s, the vanishing of the $N = 20$ gap toward $Z = 8$ was suggested in a quantitative way rather uniquely by Fukunishi, Otsuka, and Sebe (1992) and Utsuno *et al.* (1999). The situation has changed now, and other calculations also suggest a similar reduction (see Figs. 47 and 44), as part of a trend with more realistic interactions, particularly with the tensor force. Note that such a reduction of the gap facilitates more particle-hole excitations, which can enhance quadrupole deformation and pairing correlations. Thus, anomalous features around $N = 20$ have been intensely studied, providing a strong motivation to clarify, both experimentally and theoretically, how the gap evolution occurs and what consequences arise. We here refer to other related works from mean-field or clustering viewpoints (Campi *et al.*, 1975; Ren *et al.*, 1996; Terasaki *et al.*, 1997; Reinhard *et al.*, 1999; Péru, Girod, and Berger, 2000; Rodríguez-Guzmán, Egido, and Robledo, 2000; Stoitsov *et al.*, 2000; Stevenson, Stone, and Strayer, 2002; Kimura, 2007; Hinohara *et al.*, 2011; Yao *et al.*, 2011; Péru and Martini, 2014), some of which have been or will be discussed concretely. Those anomalous features are still contemporary subjects, as we see later.

2. Masses and separation energies

The mass of a nucleus is among the most basic properties directly accessible to measurements. Masses and derived quantities, e.g., one- and two-nucleon separation energies, frequently provide the first hints for the evolution of shell structure and signal the onset of deformation.

Experimental methods for the determination of atomic masses basically fall into two broad categories. Approaches that measure the Q values in decays or reactions make use of Einstein's mass-energy equivalence; mass measurements that are based on the deflection of ions in electromagnetic fields determine the mass-to-charge ratio. The most precise mass spectrometry is accomplished through frequency measurements (Myers, 2013). The cyclotron or revolution frequencies of ions in a magnetic field are measured to determine the mass-to-charge ratio in a Penning trap (Blaum, 2006) or a storage ring (Franzke, Geissel, and Münzenberg, 2008). A recent example for a mass measurement at the northern boundary of the IoI is taken out to $A = 34$ (Kwiatkowski *et al.*, 2015) from Penning-trap mass spectrometry at the TITAN facility (Dilling *et al.*, 2006).

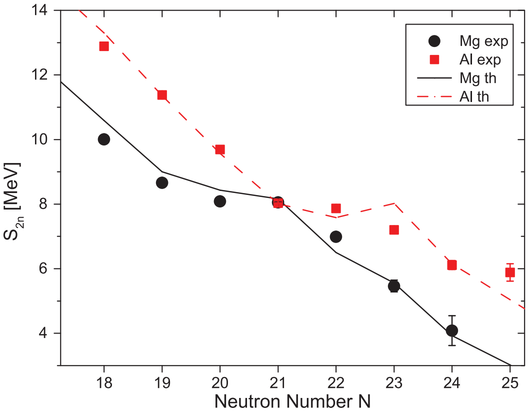

FIG. 48. Symbols indicate two-neutron separation energies for the Mg and Al isotopic chains from the 2015 TITAN experiment and the mass compilation by Audi *et al.* (2012). Shell-model calculations in the *sd-pf* shell (Caurier, Nowacki, and Poves, 2014) are shown also by the solid and dashed lines. From Kwiatkowski *et al.*, 2015.

The two-neutron separation energies (S_{2n} values) for the Al and Mg isotopic chains are shown in Fig. 48 with overlaid shell-model calculations in the *sd-pf* model space using the SDPF-U-MIX interaction introduced in Caurier, Nowacki, and Poves (2014). Typically, along an isotopic chain, the two-neutron separation energy S_{2n} decreases steadily toward the neutron dripline. We remind the interested reader that, in the presence of a large spherical shell gap at $N = 20$, the S_{2n} values would drop at $N = 21$ when the shells above the gap start to be filled. The flattening in the trend for $N = 19$–21 in the Mg chain contradicts this, and indicates the increased correlation energy of these deformed nuclei relative to their neighbors with two neutrons fewer. In Al, a hint of this effect appears only beyond $N = 21$, putting $^{31-34}$Al outside and $^{35-37}$Al at the very boundary, if not inside the IoI. Of interest is the unique crossing of S_{2n} in the Mg and Al isotopic chains at ^{34}Al, which, in comparison to the shell model, is attributed to Mg significantly gaining correlation energy upon entrance into the IoI between $N = 20$ and 21, while the S_{2n} in the Al chain is still on its almost linear downward trend up to $N = 22$.

3. Magnetic dipole and electric quadrupole moments

The deviation from sphericity of nucleus that has nonzero spin can be quantified through its electric quadrupole moment. The electric quadrupole moment was measured for the ground state of Al isotopes at the LISE spectrometer at GANIL (DeRydt *et al.*, 2009), with spectroscopic quadrupole moment $|Q_s|$ extracted for ^{31,33}Al relative to ^{27}Al (Heylen *et al.*, 2016).

The implications for the structure of ^{33}Al are shown in Fig. 49. The improved uncertainty of $|Q_s(^{33}\mathrm{Al})|$ compared to that of the previous measurement (Shimada *et al.*, 2012) led to argue the presence of neutron intruder configurations in

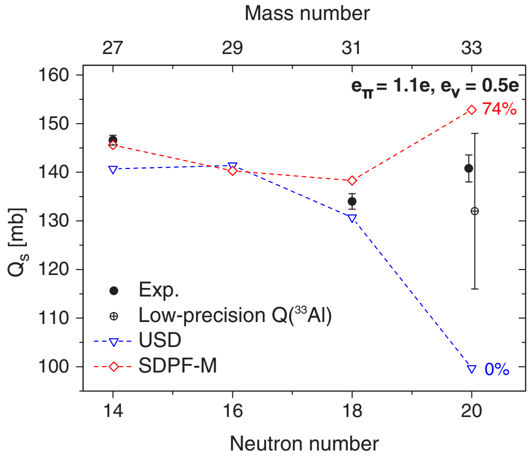

FIG. 49. Measured spectroscopic quadrupole moments of Al isotopes compared to shell-model calculations limited to the neutron *sd* shell (USD) and allowing for particle-hole excitations across $N = 20$ (SDPF-M). The given percentage signifies the amount of ground-state intruder configurations in the respective shell-model approaches. From Heylen *et al.*, 2016.

comparison to shell-model calculations that are restricted to the *sd* shell only (USD) and that allow for neutron intruder configurations across the $N = 20$ shell gap (SDPF-M) (Utsuno *et al.*, 1999, 2004). It is noted that these conclusions contradict the ones from the mass measurements reviewed previously, where ^{33}Al was placed outside of the IoI and they are at odds with shell-model calculations using the SDPF-U-MIX effective interaction (Caurier, Nowacki, and Poves, 2014) that also allows for neutrons in the *pf* shell. This may highlight the different levels of detail probed, with the moment measurement more sensitive to the very details of the configurations, or point to a puzzle in our understanding of ^{33}Al at the northern border of the IoI. Spectroscopic data on ^{33}Al, obtained, for example, using direct reactions, may identify the energies of intruder states, assessing in a complementary way the degree of intruder admixtures to the low-lying level structure of this nucleus.

Measuring hyperfine structure using laser spectroscopy is a powerful method to unambiguously determine the spin and magnetic moment of the ground state. A good example applied to the IoI is ^{31}Mg, whose ground state was assigned to be $1/2^+$ by Neyens *et al.* (2005). This measurement clearly shows that the $N = 19$ nucleus ^{31}Mg belongs to the IoI because the normal state, dominated by neutron $1d_{3/2}^{-1}$, must have $J^\pi = 3/2^+$. The spectroscopy of ^{31,33}Mg and their particle-hole structure were reviewed by Neyens (2011), indicating that a variety of intruders coexist at low excitation energies. The properties of low-lying states of odd-*A* nuclei, including their spin parities, can thus be related to the shell evolution sometimes, up to the gap between two major shells, as exemplified in Fig. 50 for positive- and negative-parity states of the ^{31}Mg nucleus.

4. Excitation energy

Energies of excited nuclear states are often among the first quantities accessible in experiments (Gade, 2015). They can be measured directly and without any model dependence and are thus some of the key observables that can be tracked to unravel changes in the nuclear structure. For instance, the systematics of the lowest 2^+ energies was discussed in Sec. I as one of the indicators of the magic structure; see Fig. 4. For excited states below the nucleon separation energies, prompt or delayed γ-ray spectroscopy is frequently used to extract excitation energies of rare isotopes with great precision, measured from the spectroscopy of the γ-ray transitions that connect different states. Electric monopole transitions between 0^+ states (Wood *et al.*, 1999) of $E0$ character proceed to a large extent through conversion electron emission and electron spectroscopy or other charged-particle spectroscopy techniques, e.g., in transfer reactions, are required (Gade and Liddick, 2016). Excited states can be populated in nuclear reactions (Gade and Glasmacher, 2008) or β decay (Rubio and Gelletly, 2009), exploiting the selectivities inherent in the different population mechanisms. For instance, the coexistence of normal and intruder states in ^{29}Na was found through β-delayed γ-ray spectroscopy (Tripathi *et al.*, 2005). The energies of long-lived isomeric states can be accessed, for example, with Penning-trap (Block *et al.*, 2008) or storage-ring (Reed *et al.*, 2010) mass spectrometry. For states that are unbound with respect to neutron or proton emission, excited-state energies can be deduced from invariant mass or missing mass spectroscopy. The spectroscopies of bound (Gade, 2015) and unbound (Baumann, Spyrou, and Thoennessen, 2012) excited states were reviewed recently.

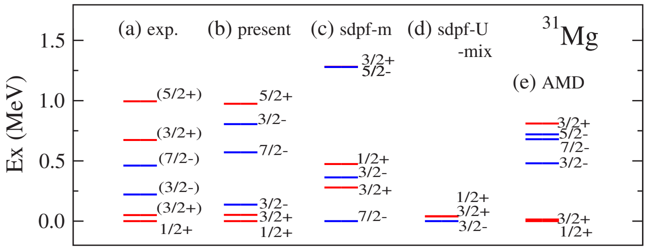

FIG. 50. Energy levels of ^{31}Mg. (a) Experimental values, (b) EEdf1 (Tsunoda *et al.*, 2017), (c) SDPF-M (Utsuno *et al.*, 1999), (d) SDPF-U-MIX (Caurier, Nowacki, and Poves, 2014), and (e) antisymmetrized molecular dynamics + generator coordinate method calculations (Kimura, 2007), respectively. From Tsunoda *et al.*, 2017.

The most recent spectroscopy inside the $N = 20$ IoI addressed one of the hallmark nuclei in this region of shell evolution, ^{32}Mg, which has been subject to experimental study since its low-lying 2_1^+ energy contradicted the presence of the $N = 20$ magic number in this isotopic chain (Détraz *et al.*, 1979). Using the advanced γ-ray tracking array GRETINA (Paschalis *et al.*, 2013), excited states in ^{32}Mg (Crawford *et al.*, 2016) were populated in the secondary fragmentation of an ^{46}Ar rare-isotope beam at NSCL. The γ rays spectrum is displayed in Fig. 51. Aside from the previously known γ-ray transitions at 885 and 1438 keV that are attributed to the $2_1^+ \to 0_1^+$ and $4_1^+ \to 2_1^+$ transitions, respectively, a new transition at 1773 keV was observed that is proposed to connect the 6_1^+ and 4_1^+ states (Crawford *et al.*, 2016). With ^{32}Mg suspected to be well deformed, this would establish the lowest part of the yrast

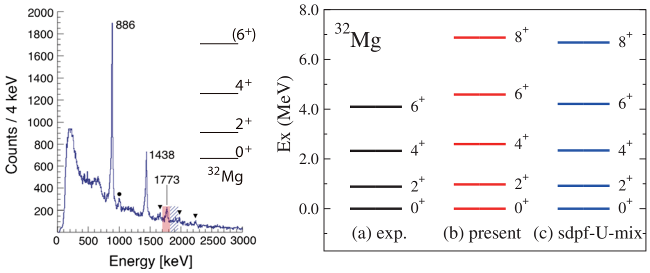

FIG. 51. (Left panel) Prompt γ-ray spectrum detected with GRETINA in coincidence with the ^{32}Mg projectilelike fragmentation residues identified in the S800 spectrograph. From Crawford *et al.*, 2016. (Right panel) Comparison to theoretical calculations with EEdf1 and SDPF-U-MIX interactions. From Tsunoda *et al.*, 2017.

rotational band. Figure 51 shows good agreement with shell-model calculation with the SDPF-U-MIX interaction, as well as that with the EEdf1 interaction which is of the *ab initio* type.

5. Electromagnetic transition strength

Nuclear structure can be probed experimentally in quantitative ways by a variety of nuclear reactions that are selective to specific degrees of freedom. Inelastic scattering, in particular, Coulomb excitation, of nuclei has long been used to investigate collective degrees of freedom that involve the coherent motion of many nucleons. $B(\sigma\lambda)$ reduced electromagnetic transition matrix elements are extracted from measured cross sections to quantify the degree of collectivity (Alder *et al.*, 1956; Cline, 1986; Glasmacher, 1998). Reduced electromagnetic transition strength can alternatively be deduced from excited-state lifetime measurement, extracted from Doppler energy shifts or line shapes in γ-ray spectroscopy (Dewald, Möller, and Petkov, 2012).

At collision energies beneath the Coulomb barrier, the excitation probabilities and interaction times are large enough to allow for multistep excitations and the determination of quadrupole moments and their signs, giving a glimpse at the degree and the character of deformation (Cline, 1986). In the regime of intermediate-energy or relativistic projectile energies, multistep processes are suppressed by several orders of magnitude. This greatly simplifies the analysis of the resulting excitation spectra, and the $B(E2; 0_1^+ \to 2_1^+)$ value has been measured for ^{32}Mg (Motobayashi *et al.*, 1995), establishing the strong deformation of this nucleus, for instance, a prediction by Fukunishi, Otsuka, and Sebe (1992) shown in the left panel of Fig. 52. The higher-lying states of collective bands, on the other hand, remain out of reach with this technique in typical experiments lasting a few days with beam rates of a few per second (Glasmacher, 1998; Gade and Glasmacher, 2008). Excited-state lifetime measurements, on the other hand, do not require nuclear models to extract transition strengths but can suffer from observed and unobserved feeding from higher-lying states, depending on the population mechanism of the excited states.

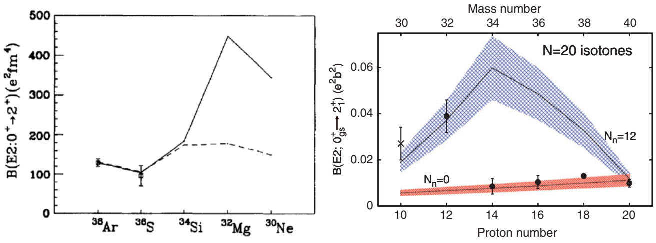

FIG. 52. $B(E2)$ value of the $N = 20$ isotones plotted as a function of Z. (Left panel) Shell-model calculation, where the solid line includes neutron excitations across the $N = 20$ gap but the dashed line does not. From Fukunishi, Otsuka, and Sebe, 1992. (Right panel) The measured values are confronted with the N_pN_n scheme calculation (Casten and Zamfir, 1993) for $N_n = 0$ ($N = 20$ closed) and $N_n = 12$ (*sd* and lower *pf* shells combined). See the text for details. Adapted from Doornenbal *et al.*, 2016.

In a recent inelastic scattering experiment at RIBF in RIKEN (Nakamura, Sakurai, and Watanabe, 2017), the quadrupole collectivity or deformation of ^{36}Mg and ^{30}Ne was determined from measured $0_1^+ \to 2_1^+$ excitation cross sections. The beams of ^{30}Ne and ^{36}Mg impinged upon the Pb and C targets. Inelastic scattering off C and relativistic Coulomb excitation on a Pb target revealed a $B(E2)$ value and deformation length, respectively, which indicates a quadrupole deformation parameter of $\beta_2 \approx 0.5$ for both, showing that the quadrupole deformation in the Mg chain persists toward the neutron dripline, and that neutron excitations across $N = 20$ are critical for reproducing the collectivity of $N = 20$ ^{30}Ne (Doornenbal *et al.*, 2016). The telltale nature of the reduced $B(E2; 0_1^+ \to 2_1^+)$ value as nuclear-structure observable is illustrated in the right panel of Fig. 52, where the $B(E2)$ strength of the $N = 20$ isotones is plotted as a function of Z. The measured values show good agreement with the earlier shell-model prediction by Fukunishi, Otsuka, and Sebe (1992). Note that the order is inverted between the left and right panels. In addition, the measured values are confronted with the phenomenology of the N_pN_n scheme (Casten and Zamfir, 1993) for $N_n = 0$ ($N = 20$ shell closure intact and no valence neutrons) and $N_n = 12$ (*sd* shell $+ f_{7/2} + p_{3/2}$ combined as the neutron shell). The sharp onset of collectivity for $Z \leq 12$ is consistent with the picture of dominant neutron particle-hole excitations across the $N = 20$ shell gap for the Mg and Ne $N = 20$ isotones, a hallmark of the IoI, at least for its northern boundary. When moving from $Z = 12$ to 14, the proton quadrupole collectivity is likely reduced due to the closure of the $1d_{5/2}$ orbit, and the $N = 20$ shell gap becomes wider; see Figs. 44, 46, and 47.

6. Shape coexistence in the island of inversion and at its boundaries: Additional evidence from β decay and $E0$ transition

Outside the IoI, excited intruder states can coexist with the still spherical ground states (Gade and Liddick, 2016). To date, shape-coexisting 0^+ states have been identified in ^{34}Si (Rotaru *et al.*, 2012) and ^{30}Mg (Schwerdtfeger *et al.*, 2009). Along the lines of the $N = 20$ isotones, ^{34}Si is situated at the northern boundary of the IoI. In a pioneering measurement at GANIL, the β decay of the 1^+ isomer of ^{34}Al was used to selectively feed 0^+ states in ^{34}Si, including the previously unobserved excited 0_2^+ state at 2719(3) keV

(Rotaru et al., 2012). This state is located below the 2_1^+ one, presenting an experimental challenge. Since γ-ray decays between 0^+ states are angular-momentum forbidden, this low-lying 0^+ state can deexcite only via electron conversion or internal pair formation, where an electron-positron e^+e^- pair is released with a total energy of $E_{e^-} + E_{e^+} = E(0_2^+) - 2 \times 511$ keV. From the difference timing between the β-decay events and the e^+e^- pair signals, a half-life of 19.4(7) ns was determined for the 0_2^+ state (Rotaru et al., 2012). The resulting low $E0$ transition strength indicates only weak mixing between the 0_1^+ ground state and the 0_2^+ excited state. Combining all spectroscopic information, including $B(E2; 2_1^+ \to 0_2^+) = 61(40)e^2$ fm^4, as extracted from a small γ-ray branch and the 2_1^+ lifetime, results in a quadrupole deformation parameter for the 0_2^+ state of $\beta = 0.29(4)$, in agreement with SDPF-U-MIX shell-model calculations (Rotaru et al., 2012). All of these properties are consistent with the argument presented at the end of Sec. VI.A.5 . Once the ground state becomes closed-shell-like, the shape coexistence often arises (Heyde and Wood, 2011).

For ^{32}Mg, at the heart of the IoI, a (t, p) neutron-pair transfer reaction was used in reverse kinematics to, for the first time, identify the 0_2^+ state in ^{32}Mg at 1058(2) keV at the REX-ISOLDE facility (CERN) (Wimmer et al., 2010; Bildstein et al., 2012). The proton angular distributions of both states were shown to display the shape of an angular-momentum transfer of $\Delta L = 0$ onto the ground state of ^{30}Mg. It was thus concluded that both states in ^{32}Mg populated in the (t, p) transfer have spin 0.

Coincident γ-ray transitions detected, as a new transition with an energy of 172 keV and the well-known $2_1^+ \to 0_1^+$ transition at 886 keV, allowed experimenters to put the newly discovered excited 0^+ state at the more precise energy of 1058 (2) keV. Based on distorted wave Born approximation (DWBA) calculations, it was concluded that the ground state comprises $(f_{7/2})^2$ and $(p_{3/2})^2$ intruder configurations, and the excited 0^+ state could be largely described with the assumption of sd-shell normal-order configurations, such as $(d_{5/2})^2$, however, with a small $(p_{3/2})^2$ intruder contribution necessary (Wimmer et al., 2010). These findings support the picture of a deformed fp-shell intruder ground state and an sd-shell dominated (spherical) first excited 0^+ state. The approximately equal cross sections for the formation of the two 0^+ states in (t, p) were used to infer significant mixing between the two states. A measurement of the electric monopole strength connecting the two states remains a challenge for future experiments. The 0_2^+ excitation energy of about 1 MeV was found to be significantly below available model predictions at the time (Wimmer et al., 2010). These properties of the 0_2^+ state of ^{32}Mg pose a formidable challenge for theory, including beyond-mean-field models (Rodríguez-Guzmán, Egido, and Robledo, 2000; Péru and Martini, 2014).

Recently, shell-model calculations that allow for the mixing of configurations that have two, four, and six neutrons promoted across the $N = 20$ shell gap (SDPF-U-MIX) reproduce the reported low 0_2^+ energy and suggest a rather unique character of this 0^+ state (Caurier, Nowacki, and Poves, 2014). A ground-state neutron configuration of 9% $0p$-$0h$, 54% $2p$-$2h$, 35% $4p$-$4h$, and 1% $6p$-$6h$ emerges and suggests a mixture of deformed and superdeformed configurations. The excited 0^+ state is calculated to be composed of 33% $0p$-$0h$, 12% $2p$-$2h$, 54% $4p$-$4h$, and 1% $6p$-$6h$ neutron particle-hole configurations, painting a rather complex picture of ^{32}Mg where the second 0^+ state carries significant spherical as well as superdeformed configurations, rendering the simple concept of a deformed ground state and a spherical excited 0^+ as too simplistic. The confirmation and further characterization of the 0_2^+ state of ^{32}Mg appears to be warranted to clarify the important phenomenon of shape coexistence inside the $N = 20$ IoI.

Seemingly contradictory conclusions to what was inferred by Wimmer et al. (2010), termed the ^{32}Mg puzzle, were drawn from a simple two-level mixing model (Fortune, 2011, 2012) and resolved recently using a three-level mixing approach (Macchiavelli et al., 2016), in line with a more complicated structure that has been suggested by the shell-model calculations mentioned previously.

7. Direct reactions as a probe of nuclear wave function

Direct nuclear reactions have proven to be a vital tool for the spectroscopy of the single-particle components in the nuclear wave function, showing direct relevance to the probing of the shell evolution. In a glancing collision of a projectile and a target nucleus, one or a few nucleons are transferred directly without formation of an intermediate compound system.

The classic low-energy transfer reactions that, for stable target nuclei, use a variety of light projectiles to probe occupied single-particle levels and valence states (Macfarlane and French, 1960), e.g., the (d, p) neutron-adding and $(d, {}^3\mathrm{He})$ proton-removing transfers, are now employed at low-energy rare-isotope facilities in inverse kinematics when low-emittance, high-intensity rare-isotope beams are available; see Gaudefroy et al. (2006), Catford et al. (2010), Kanungo et al. (2010), Wimmer et al. (2010), Fernández-Domínguez et al. (2011), and Burgunder et al. (2014) for examples from different facilities. At intermediate beam energies (~100 MeV/nucleon), thick-target γ-ray tagged one- and two-nucleon knockout reactions on ^{9}Be or ^{12}C targets have been developed into spectroscopic tools to study single-nucleon-hole states and correlations of two like nucleons in exotic nuclei (Bazin et al., 2003; Hansen and Tostevin, 2003; Tostevin et al., 2004; Yoneda et al., 2006; Gade et al., 2008; Simpson et al., 2009; Simpson and Tostevin, 2010).

By comparing cross sections with C and Pb targets, it is also possible to extract Coulomb reaction cross sections, which are used to look into the neutron shell structure through the halo formation in ^{31}Ne and ^{37}Mg (Nakamura et al., 2009, 2014; Kobayashi et al., 2014).

At high beam energies, typically exceeding 70 MeV/nucleon, a theoretical description (Tostevin, 1999) in the framework of eikonal trajectories and sudden approximation is applicable. Therefore, the model dependence is limited compared to the classical low-energy transfer reactions, whose description involves the DWBA or higher-order formalisms, which depend strongly on entrance-channel and exit-channel optical model potentials (Kramer et al., 1988),

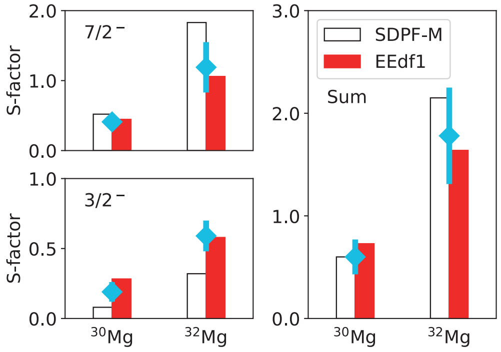

FIG. 53. Spectroscopic factors from ^{9}Be(^{32,30}Mg, ^{31,29}Mg)X knockout reactions to two negative-parity states of ^{32,30}Mg. Deduced spectroscopic factors are indicated by blue point with error bar (Terry *et al.*, 2008). Single-particle occupancies obtained using the SDPF-M shell model (Utsuno *et al.*, 1999) are represented by empty histograms. Spectroscopic factors calculated with the EEdf1 interaction are shown as red histograms (Tsunoda, 2018).

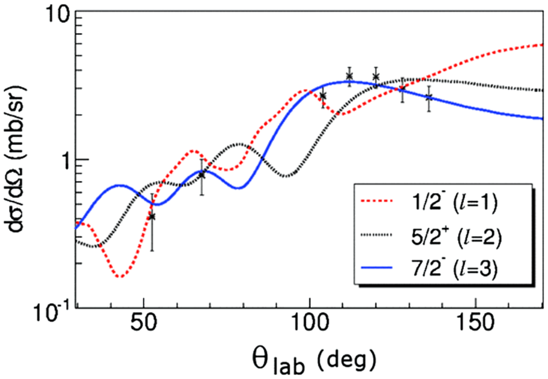

FIG. 54. Proton angular distribution for the new neutron-unbound state discovered at 1.74 MeV in ^{27}Ne. In comparison to reaction theory, an $\ell = 3$ orbital angular momentum was assigned. From Brown *et al.*, 2012.

which have not yet been established for nuclei with extreme neutron-to-proton ratios. It was shown recently that low-energy transfer reactions and nucleon removal reactions can be analyzed to give consistent results (Mutschler *et al.*, 2016b). Both knockout and transfer reactions have been used to track the descent of intruder states along isotopic chains approaching the IoI. Two complementary examples are reviewed in the following.

The onset of pf shell intruder configurations was quantified along the Mg chain with γ-ray tagged one-neutron removal measurements ^{9}Be(^{30}Mg, ^{29}Mg $+ \gamma$)X and ^{9}Be(^{32}Mg, ^{31}Mg $+ \gamma$)X, performed at NSCL (Terry *et al.*, 2008). From the shapes of the ^{29,31}Mg parallel momentum distributions gated on the individual γ-ray transitions, the 1.095 and 1.431 MeV states in ^{29}Mg, and the 0.221 and 0.461 MeV levels in ^{31}Mg were shown to be of $\ell = 1$ and 3 orbital angular momentum, respectively, identifying $p_{3/2}$ and $f_{7/2}$ single-neutron configurations in the ground states of both ^{30}Mg and ^{32}Mg. From the partial cross sections for the population of the negative-parity states in the knockout residues, $f_{7/2}$ and $p_{3/2}$ spectroscopic factors were deduced. The resulting quantification of the onset of f and p intruder configurations in the ground states of ^{30}Mg and ^{32}Mg is seen in Fig. 53: the neutron pf-shell strengths increase significantly at $N = 20$, signaling a dramatic shift in the nuclear structure of ^{32}Mg compared to ^{30}Mg. The spectroscopic factors calculated with EEdf1 interaction (Tsunoda *et al.*, 2017, 2018) show good agreement with experiment when this calculation includes the reduction factor of 0.75 that is inherent to knockout reactions (Tostevin and Gade, 2014). The occupation numbers obtained with the SDPF-M interaction (Utsuno *et al.*, 1999) were used in the analysis of Terry *et al.* (2008), as shown in Fig. 53, depicting a similar trend. Compared to the SDPF-M interaction, the EEdf1 interaction gives a better description for the energy levels for ^{32,31}Mg in Figs. 51 and 50, respectively, as well as for the spectroscopic factors in Fig. 53. The last figure illustrates the amount of the excitations across the $N = 20$ magic gap. We stress that the shell evolution through this EEdf1 interaction (see Fig. 44) exhibits similarities to earlier results shown in Figs. 46 and 47.

In the Ne isotopic chain, a γ-ray tagged neutron-adding transfer reaction d(^{26}Ne, ^{27}Ne $+ \gamma$)p, performed at GANIL, identified for the first time the neutron-unbound $7/2_1^-$ state at 1.74(9) MeV in ^{27}Ne (Brown *et al.*, 2012). The $\ell = 3$ orbital angular momentum of the state was concluded from the proton angular distribution in comparison to adiabatic distorted wave approximation transfer reaction calculations; see Fig. 54.

The $3/2^-$ state could be identified at 0.765 MeV, confirming earlier work that could restrict the orbital angular momentum of this state only to $\ell = 0$ and 1 (Terry *et al.*, 2006). The fact that the $7/2^-$ state is higher in energy than the $3/2^-$ level presents a remarkable inversion from the ordering closer to stability and disagrees with the sequence predicted by the SDPF-M Hamiltonian (Brown *et al.*, 2012). This result will serve as an important benchmark for new effective shell-model Hamiltonians in the region in their quest to describe the shell evolution in and around the IoI.

8. More on direct reactions: Tracking single-particle strengths to learn about the spin-orbit force

The spin-orbit splitting is a corner stone of the nuclear shell model. Recent work using inverse-kinematics transfer reactions (Burgunder *et al.*, 2014) and one-proton knockout reactions (Mutschler *et al.*, 2016a) on the key nucleus ^{34}Si, located at the boundary of the island of inversion, explored the signatures and evolution of the spin-orbit splitting in neutron-rich nuclei.

At GANIL, the single-particle nature of states in ^{37}S and ^{35}Si and the associated spectroscopic strengths were obtained for the first time by inverse-kinematics (d, p) reactions (Burgunder *et al.*, 2014). In comparison to reaction theory, the proton angular distributions were measured (i) to assign ℓ values for the transferred neutrons from their shape, and (ii) to extract spectroscopic factors from their absolute scale. By tracking the location of the dominant $2p_{1/2}$ and $2p_{3/2}$ fragments, it was reported that the spin-orbit splitting between the $2p_{3/2}$ and $2p_{1/2}$ neutron orbits decreases by 25% in ^{35}Si

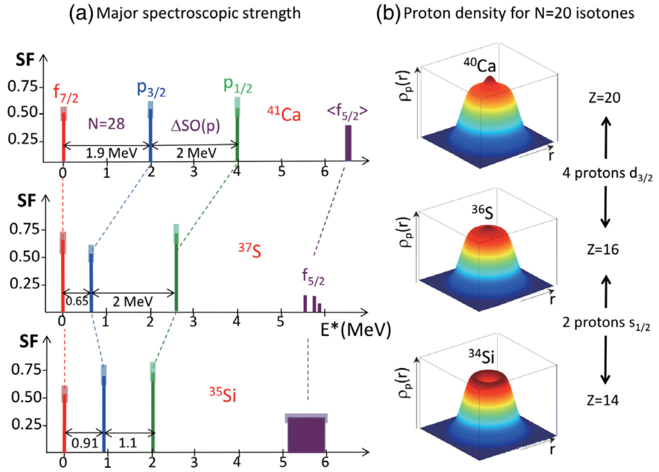

FIG. 55. (a) Evidence for a reduction of the $2p_{3/2}$-$2p_{1/2}$ spin-orbit splitting in the $N = 21$ isotonic chain at ^{35}Si. For comparison, the spin-orbit splitting remains unchanged between ^{41}Ca and ^{37}S. From Burgunder *et al.*, 2014. (b) Change of the proton density along the $N = 20$ isotone line from density functional theory [relativistic mean field with the DDME2 interaction (Lalazissis *et al.*, 2005)]. The vanishing proton occupation of the $s_{1/2}$ orbital leads to a central depletion in the density that has been likened to a bubble. From O. Sorlin and J. P. Ebran.

relative to the less exotic isotone ^{37}S, while almost no change was found for the neutron $1f_{7/2}$-$1f_{5/2}$ spin-orbit splitting [Fig. 55(a)] (Burgunder *et al.*, 2014). We can understand this feature as explained later. The major difference from ^{35}Si to ^{37}S is the occupancy of the proton $2s_{1/2}$ orbit, which has a large effect on the $2p_{3/2}$-$2p_{1/2}$ splitting due to the 2b-*LS* force; see Sec. IV.F. On the other hand, the $2s_{1/2}$ occupancy has a vanished effect on the $1f_{7/2}$-$1f_{5/2}$ splitting due to the tensor force; see the third item of the remarks in Sec. IV.B.4.

Further studies on the neutron $2p_{3/2}$-$2p_{1/2}$ splitting of the same nuclei have been made recently (Kay, Hoffman, and Macchiavelli, 2017) where the change of this splitting was interpreted in terms of loose binding effects. It, however, can be described in terms of the monopole effect of the 2b-*LS* force, as described in Sec. S6 of the Supplemental Material (364). Further studies are of great interest.

Electron scattering off stable nuclei demonstrated that their central densities are saturated, as for a liquid drop, for example. In rare isotopes at the extreme of isospin, the possibility of a depleted central density, or a "bubble" structure, has been discussed for more than 40 years. If observed, it will be of much interest. In general, central depletions will arise from the reduced occupation of low-ℓ single-particle orbits, as exemplified in Fig. 55(b) for the $N = 20$ isotones ^{40}Ca, ^{36}S, and ^{34}Si with calculated proton density distributions from a relativistic mean-field functional (DDME2) (Lalazissis *et al.*, 2005). The central depletion in the proton density for ^{34}Si is attributed to a vanishing occupancy of the proton $2s_{1/2}$ orbital. A one-proton knockout measurement from a ^{34}Si projectile beam at NSCL, combined with in-beam γ-ray spectroscopy using GRETINA, revealed indeed that the proton $2s_{1/2}$ orbital in this nucleus is depleted, possibly leading to a depleted central proton density or bubble inside of neutron-rich ^{34}Si, making this the best candidate for this phenomenon to date (Mutschler *et al.*, 2016a). In knockout reactions, the shape of the parallel momentum distributions of the knockout residues is sensitive to the ℓ value of the removed nucleon, and the partial cross sections for the population of individual final states can be used to extract spectroscopic factors in comparison to reaction theory (Hansen and Tostevin, 2003). With this approach, the cross section for the removal of an $\ell = 0$ proton from ^{34}Si was found to be only 10% of that for the proton removal from ^{36}S (Mutschler *et al.*, 2016a, 2016b). Since the cross section for the removal of protons from an orbit is proportional to the orbit's proton occupancy, this difference in cross section was interpreted as evidence for a depleted $2s_{1/2}$ proton orbital in ^{34}Si, in striking contrast to the same orbital being fully occupied in the ^{36}S isotone (Khan *et al.*, 1985; Mutschler *et al.*, 2016b).

9. At the southern border: Continuum and shell-evolution cases with multinucleon transfer reaction

On the nuclear chart, two protons south of the island-of-inversion nucleus ^{30}Ne lies ^{28}O. The $N = 20$ nucleus ^{28}O has been suspected to be unbound with respect to neutron decay based on cross section or yield systematics established in its attempted production in the fragmentation of intermediate-energy ^{36}S and ^{40}Ar beams at GANIL and RIKEN, respectively (Tarasov *et al.*, 1997; Sakurai *et al.*, 1999). The neutron-rich oxygen isotopes at the southern border of the island of inversion have been a formidable testing ground for nuclear theory, where the particularly visible feature is that ^{24}O is the last bound oxygen isotope, while the fluorine isotopes with just one more proton exist out to at least mass number $A = 31$, sometimes called the *oxygen anomaly* by Otsuka, Suzuki, Holt *et al.* (2010). Shell-model approaches (Volya and Zelevinsky, 2005; Otsuka, Suzuki, Holt *et al.*, 2010; Tsukiyama, Otsuka, and Fujimoto, 2015), mean-field theory (Co' *et al.*, 2012; Erler *et al.*, 2012), and *ab initio*–type calculations (Hagen *et al.*, 2009, 2010; Duguet and Hagen, 2012; Cipollone, Barbieri, and Navrátil, 2013; Bogner *et al.*, 2014; Simonis *et al.*, 2016) have been made in the quest for new physics in nuclei near driplines. The incorporation of the continuum is an ongoing effort in the development of many-body approaches.

The nucleus ^{26}O is a unique three-body system since it was found to be barely unbound, able to decay by two-neutron emission only with an energy of less than 20 keV (Kondo *et al.*, 2016). Two early measurements at NSCL and GSI provided the first evidence for the ground-state resonance of ^{26}O at 150^{+50}_{-150} keV (Lunderberg *et al.*, 2012) and 25 ± 25 keV (Caesar *et al.*, 2013), respectively. In all measurements, the experimental scheme was very similar. In kinematically complete measurements, the energy of decaying resonances was reconstructed in invariant mass spectroscopy from the momentum vectors of the two emitted neutrons and the residue in $^{24}\mathrm{O} + n + n$. The highest-statistics measurement yet was performed at RIBF/RIKEN with the SAMURAI spectrometer (Kobayashi *et al.*, 2013; Kondo *et al.*, 2016; Nakamura, Sakurai, and Watanabe, 2017). From reconstruction of the invariant mass, the ground state of ^{26}O was found at only $18 \pm 3(\mathrm{stat}) \pm 4(\mathrm{syst})$ keV above the two-neutron

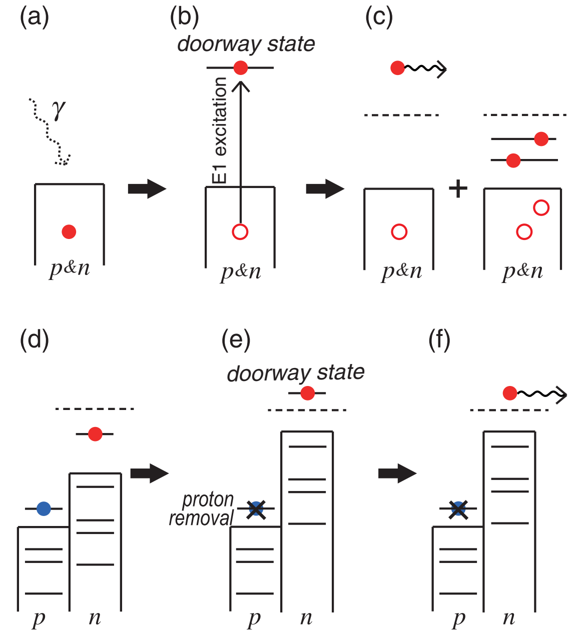

FIG. 56. Schematic pictures of the doorway state for (a)–(c) $E1$ excitation and (d)–(f) a reaction induced by the removal of a proton. Dashed lines indicate the neutron threshold. Red filled circles indicate the neutron being discussed, while red open circles are neutron holes. Blue circles are protons, and crossed blue circles are absent after the initial impact of the reaction. From Tsukiyama, Otsuka, and Fujimoto, 2015.

decay threshold (Kondo *et al.*, 2016). In addition, a candidate for the excited 2_1^+ state at $1.28_{-0.08}^{+0.11}$ MeV was identified for the first time.

Regarding the shell evolution, Kondo *et al.* (2016) write, “The structure of ^{26}O may be influenced by shell evolution, *nn* correlations, and continuum effects.” It is, however, not trivial how and what type of “resonance” states can be created in various transfer reactions, including those involving heavy ions. Using Fig. 56, we explain schematically the relation between the shell evolution and the neutron emission after such reactions. Figures 56(a)–56(c) exhibit the doorway state in a (γ, n) process, while Figs. 56(d)–56(f) depict a similar doorway state due to a sudden removal of a proton by a transfer reaction. The removal of the proton lifts up neutron ESPEs by the amount of its monopole effect; see Fig. 56(d). If this single-particle state is in the continuum, it becomes a doorway state, as shown in Fig. 56(e). Its wave function is the same as the corresponding state before the reaction. The neutron in the doorway state goes away through one of the continuum states, with the probability given basically by the squared overlap between the doorway state and such continuum states. The shape of the energy spectrum is determined by this probability, with the peak shifted by continuum couplings. Thus, the neutron spectrum indicates the combined effect of the shell evolution and the continuum; see Tsukiyama, Otsuka, and Fujimoto (2015) for details. Although actual situations may contain different details, the basic picture is expected to remain.

A possible long lifetime of the ground-state resonance that would allow for “two-neutron radioactivity” is discussed by Caesar *et al.* (2013), Grigorenko, Mukha, and Zhukov (2013), Kohley *et al.* (2013), and Kondo *et al.* (2016) and remains an interesting possibility for a new phenomenon beyond the neutron dripline.

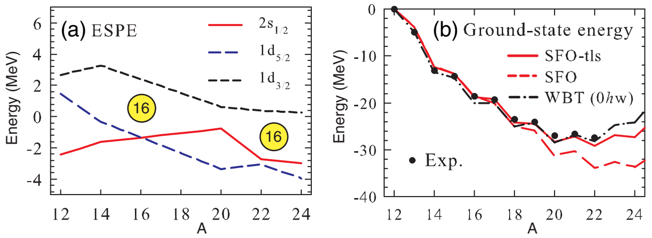

FIG. 57. (a) ESPEs for neutron orbits in C isotopes obtained with the SFO-tls interaction. (b) Ground-state energies of C isotopes obtained with SFO-tls, SFO, and WBP (Warburton and Brown, 1992) as well as experimental data. In (a), the filling scheme is taken in the order of $1p_{1/2}$, $1d_{5/2}$, $2s_{1/2}$, and $1d_{3/2}$, as this order represents rather well the configurations of actual eigenstates. The ESPEs at their closures are connected. The $N = 16$ (sub)magic gap is highlighted by the yellow circle.

B. Neutron halo observed in exotic C isotopes and $N = 16$ magic number

Halo nuclei have been identified through their greatly enhanced interaction cross section measured in the bombardment with a variety of targets. With the example of the C isotopes, we discuss in the following the relationship between halo formation and shell evolution. The SFO-tls (Suzuki and Otsuka, 2008) Hamiltonian is used, while the Cohen-Kurath (called CK usually) (Cohen and Kurath, 1965) and Millener-Kurath (called MK usually) (Millener and Kurath, 1975) Hamiltonians were employed earlier. The SFO-tls Hamiltonian is designed for *p*-*sd* shell nuclei with the cross-shell tensor and 2b-*LS* parts taken from the V_{MU} interaction (see Sec. IV.C) and the M3Y 2b-*LS* interaction [see Sec. IV.F and Sec. S5 of the Supplemental Material (364)], respectively, so as to include shell-evolution effects in a manner quantitatively similar to the results presented so far. The *sd*-shell part is also improved by taking into account the effects of three-body forces; see Secs. V.C and V.D. Calculations with this Hamiltonian reproduce well the shell evolution in the ^{15}C-^{16}N-^{17}O isotones including the $5/2^+$-$1/2^+$ inversion; see Sec. IV.F.

Figure 57(a) depicts neutron ESPEs of C isotopes obtained from the SFO-tls Hamiltonian in the filling scheme. While the $2s_{1/2}$ orbit is below the $1d_{5/2}$ orbit in ^{12}C, the $2s_{1/2}$ ESPE is raised through $A = 20$, crossing the $1d_{5/2}$ orbit. This is because the neutron-neutron $1p_{1/2}$-$2s_{1/2}$ and $1d_{5/2}$-$2s_{1/2}$ monopole interactions are both repulsive, and they push up the $2s_{1/2}$ orbit as neutrons occupy the $1p_{1/2}$ and $1d_{5/2}$ orbits. This disappearance of the gap at $N = 14$ in C isotopes around $A = 16$ was reported by Stanoiu *et al.* (2008). This shell evolution produces the $1/2^+$ ground state in ^{15}C, and the $3/2^+$ ground state in ^{17}C, which is natural with a dominant neutron $1d_{5/2}^3$ configuration. The present irregular variation of the ground-state spin can thus be understood. Figure 57(a) indicates that the $N = 16$ magic gap appears around $A = 16$. It then disappears around $A = 20$ because of the raise of the $2s_{1/2}$ orbit. The $2s_{1/2}$ orbit becomes loosely bound. Because this is an s orbit, a neutron halo occurs in the $1/2^+$ ground state of ^{19}C with the $s^1_{1/2}\, d^4_{5/2}$ neutron configuration, which is consistent with experiments (Nakamura *et al.*, 1999; Kanungo *et al.*, 2016). This shows how the shell evolution is related to the neutron halo formation. We note that the $2s_{1/2}$ orbit is raised by a repulsive effect simulating the three-body-force effect, as mentioned previously. As the ^{20}C ground state consists, to a large extent, of the subshell closure of the $d_{5/2}$ orbit in the shell-model calculation (Suzuki *et al.*, 2016), no neutron halo is expected there.

Figure 57(a) indicates that the $N = 16$ magic number appears again around $A = 22$, which brings about more interplay between the shell evolution and the neutron halo. Figure 57(b) shows the ground-state energies of C isotopes relative to that of ^{12}C for SFO-tls, SFO, and WBT (Warburton and Brown, 1992) Hamiltonians in comparison to experiment. A repulsive neutron-neutron monopole interaction contained in the SFO-tls interaction pushes up the energy in the neutron-rich region, reproducing the experimental data, similar to the O isotopes discussed in Secs. V.C and V.D. Figure 57(a) shows that the $2s_{1/2}$ orbit is rather well bound with an ESPE below -2 MeV at $A = 22$ in the filling scheme, indicative of a situation opposing a two-neutron halo. On the other hand, Fig. 57(b) displays that ^{22}C is barely bound with respect to ^{20}C as far as the total binding energy is concerned. The many-body correlations in ^{22}C bring about the formation of a two-neutron halo, which is unlikely from the viewpoint of the mean potential. The neutron halo of ^{22}C was reported experimentally by Tanaka *et al.* (2010), Kobayashi *et al.* (2012), and Togano *et al.* (2016), while theoretical studies were performed with three-body models (Horiuchi *et al.*, 2006; Yamashita *et al.*, 2011; Kucuk and Tostevin, 2014). We report here on a rather different approach: the extended shell-model calculation is performed not only by including usual shell-model correlations but also by taking into account the interaction between the halo neutrons taken from the low-energy limit of neutron-neutron scattering (Suzuki *et al.*, 2016). Figure 58 depicts the radius of the two-neutron halo (∼6–7 fm) as consistent with experiment (Togano *et al.*, 2016); the halo radius deduced from the experimental matter radius (Togano *et al.*, 2016) is $6.79^{+0.70}_{-0.66}$ fm, which is well below the value obtained for such a small separation energy by the usual simple relation (halo radius > 10 fm for $S_{2n} < 0.3$ MeV) (Suzuki *et al.*, 2016). Thus, the combination of shell evolution and dynamical correlations can give a proper description of this unusual formation of a two-neutron halo. It is of interest that the ground-state neutron halo seems to occur in ^{19}C as a single-particle phenomena and in ^{22}C as a result of correlations.

As Z becomes smaller, below $Z = 6$, the neutron $1p_{1/2}$ orbit is raised due to weakened attraction with the proton $1p_{3/2}$ orbit, and it approaches the $2s_{1/2}$ orbit. This shell evolution leads to a vanishing of the shell closure at $N = 8$, and the SO magic number $N = 6$ becomes reinforced; see Fig. 2. The decrease of the gap between the $1p_{1/2}$ and $2s_{1/2}$ orbits enhances the large admixture of sd-shell components in the ground states of nuclei such as ^{12}Be, as well as in the dripline nucleus ^{11}Li.

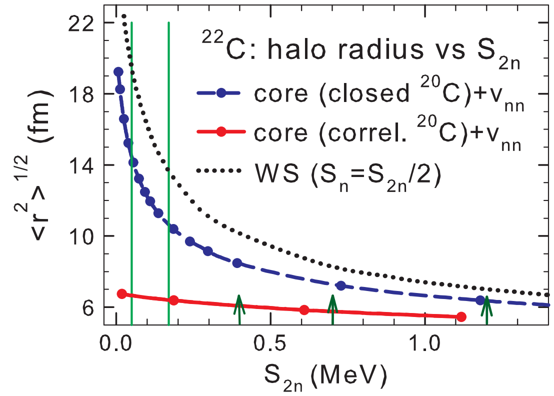

FIG. 58. The rms radius of the halo neutron as a function of two-neutron separation energy S_{2n}. The blue dashed line and filled circle indicate the result obtained with the core of the closed-shell ^{20}C, while the red solid line and filled circle indicate the result with the core of the correlated ^{20}C. The result obtained from the Woods-Saxon potential ($S_n = S_{2n}/2$) without v_{nn} is shown as the black dotted line. The range of S_{2n} obtained from ENSDF (2017) is shown by green thin vertical lines. Green arrows denote the values discussed by Kobayashi *et al.* (2012). The halo radius, $6.79^{+0.70}_{-0.66}$ fm, can be deduced from the experimental matter radius (Togano *et al.*, 2016) (see the text). From Suzuki *et al.*, 2016.

C. Shell evolution examined by $(e,e'p)$ experiment

The electron scattering enables us to carry out a model-independent analysis of obtained data, and it therefore provides us with an excellent and unique tool to see the nuclear structure, apart from the limitation due to low cross sections and the limited applicability only to stable nuclei at present. Among various types of experiments, the $(e,e'p)$

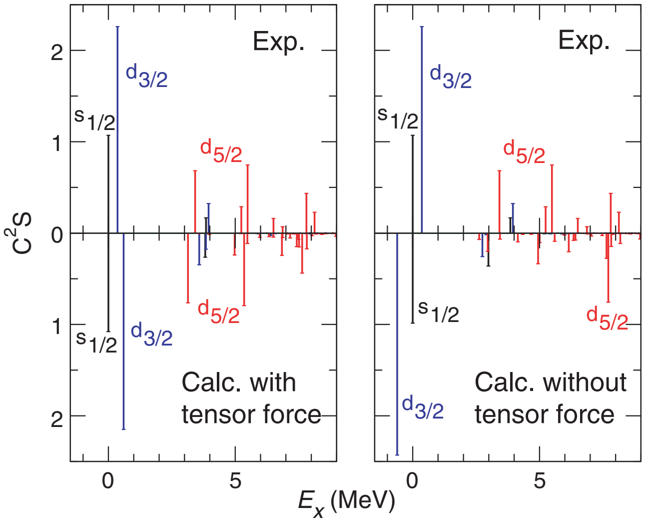

FIG. 59. Distribution of proton-hole strengths in ^{48}Ca compared between the $(e,e'p)$ data (Kramer, Blok, and Lapikás, 2001) and shell-model calculations with the SDPF-MU interaction. The left and right panels show the calculations with and without the cross-shell tensor force, respectively. The calculated overall spectroscopic factors are quenched by 0.7. From Utsuno *et al.*, 2012a.

experiment is a superb method to investigate proton single-particle properties including the shell structure. Figure 59 shows in the upper panels the distribution of the proton-hole strengths with respect to the ^{48}Ca nucleus measured with the $^{48}\mathrm{Ca}(e,e'p)^{47}\mathrm{K}$ reaction (Kramer, Blok, and Lapikás, 2001). In Fig. 59, the measured distribution is compared to shell-model calculations using the SDPF-MU interaction introduced in Utsuno *et al.* (2012a), with (lower left panel) and without (lower right panel) the tensor force. The sd-pf cross-shell part of the SDPF-MU interaction is the V_{MU} interaction with which many theoretical analyses have been carried out, as mentioned earlier in this review, and it contains the same tensor force used throughout the article. Figure 59 exhibits that calculations by the SDPF-MU interaction with the tensor force reproduce quite well the measurement for both energies and strengths. The proton $1d_{5/2}$-$1d_{3/2}$ splitting is calculated to be 5.1 MeV with the SDPF-MU interaction. Once the tensor part of the interaction is switched off, the $1d_{5/2}$ strengths are shifted to higher energies by the absence of the mechanism shown in Fig. 17. Note that the hole energy goes up when the corresponding orbit is lowered.

The proton spin-orbit splitting in ^{40}Ca is estimated to be $\sim$6.7 MeV on the basis of the centroid energy using the $(d,{}^{3}\mathrm{He})$ reaction data (Doll *et al.*, 1976), where the $1d_{5/2}$ strengths are highly fragmented in the $E_x > 5$ MeV region. A precise measurement for ^{40}Ca similar to the one for ^{48}Ca is of much interest. See Sorlin and Porquet (2008) for details of deducing proton-hole energies in the K isotopes from the $(d,{}^{3}\mathrm{He})$ data.

D. Other cases in heavy nuclei

Some of other relevant studies on heavier nuclei are worked out in Sec. S7 of the Supplemental Material (364) (Federman and Pittel, 1977; Goodman, 1977; Ogawa *et al.*, 1978; Federman, Pittel, and Campos, 1979; Zeldes, Dumitrescu, and Köhler, 1983; Federman, Pittel, and Etchegoyen, 1984; Pittel *et al.*, 1993; Kay *et al.*, 2008, 2011; Schiffer *et al.*, 2013; Santamaria *et al.*, 2015).

VII. SUMMARY

This article presents a review of the structure of exotic nuclei mainly from the viewpoint of the shell evolution driven by nuclear forces. While shell evolution implies changes of the shell-magic structure, such changes, in particular, substantial and/or systematic ones, were not expected several decades ago. In fact, the shell-magic structure proposed by Mayer and Jensen was shown to be extremely successful in the description of the structure of nuclei. A few exceptional cases of notable changes were known, with their examples mentioned in Secs. II and III.G. Certain changes of the shell structure have gradually been noticed, and some empirical analyses were made as reviewed, for instance, by Grawe (2004) and Sorlin and Porquet (2008, 2013). However, over the past two decades, many cases of substantial and systematic changes of the shell-magic structure have been clarified with underlying theoretical mechanisms and/or with experimental data thanks mostly to rare-isotope beam experiments. Among the various outcomes and phenomena, particularly visible ones are the identification of new magic numbers $(16, 32, 34, \ldots)$ and the recognition of diminished traditional magic numbers $(8, 20, 28, \ldots)$, occurring in certain regions of the Segré nuclear chart. Thus, the shell evolution turned out to be a distinctive phenomenon, visible particularly in exotic nuclei.

The shell evolution is driven by the monopole interaction, which is a component of the nuclear force in nuclei. The monopole interaction has been discussed in various ways since 1964 (Sec. III.E), and we review, throughout this article, its underlying mechanism and its appearance in a variety of physics phenomena.

After a brief survey of earlier works in Secs. I and II, we start with a possible definition of the monopole interaction in Sec. III, which is applicable for closed-shell and open-shell nuclei. In the case of atomic nuclei, rotational invariance is imposed as a symmetry constraint, and this symmetry produces degeneracy with respect to the magnetic substates of each single-particle orbit. The monopole interaction then arises for a given two-body interaction from this degeneracy: the motion of two interacting particles in given single-particle orbits j and j' can take various two-body quantum states. The monopole matrix element is an average with respect to them (Sec. III). The ESPE is obtained by combining this monopole interaction and a given configuration (an occupation pattern over all single-particle orbits) (Sec. III.D). The ESPEs are operators, but they can be c numbers if the configuration is fixed. The ESPEs calculated for a typical configuration provide us with a clear and simple perspective of nuclear structure, for example, as neutrons are added to a specific orbit in an isotopic chain. While the definition or meaning of the ESPE might look different among different formulations, they are shown to be consistent (Secs. III.E and III.F).

The monopole interactions of the central, tensor, two-body spin-orbit and three-nucleon forces produce different characteristic features in the variations of the ESPEs (i.e., shell evolution), as illustrated in Secs. IV and V. The tensor and two-body spin-orbit forces provide unique and notable effects because of their spin dependences (Sec. IV). Many of the underlying properties of these many-body effects were clarified rather recently both theoretically and experimentally, although these forces have been known for several decades. Because of the renormalization persistency, the monopole effect of the tensor force can be evaluated in a simple way (Sec. V.A).

The central force basically senses similarities of radial single-particle wave functions (Sec. IV.A) and produces important contributions; in many of the cases of shell evolution, the central and tensor forces work coherently with similar magnitudes. For instance, this coherence is directly related to the appearance of the $N = 34$ magic number (Sec. IV.D.4), as well as the shell structure on top of the ^{100}Sn closed shell (Sec. IV.D.2), for which extensive experimental studies are ongoing. Some aspects of central-force effects have been discussed since its early days (Secs. IV.A and IV.D). A wide variety of mean-field approaches, nonrelativistic and relativistic, have been proposed for the description of the shell structure, including various functionals for the tensor-force effects (Sec. IV.E).

Modern *ab initio* approaches are expected to derive effective NN interactions from the QCD level (Sec. V), including three-nucleon-force effects. The monopole effect from the three-nucleon forces has been shown to be crucial for nuclear binding, including the dripline of the oxygen isotopes (Sec. V).

The shell evolution was evaluated in many analyses presented in this review in terms of the V_{MU} interaction and the two-body spin-orbit force in the M3Y interaction. These are given in simple analytic forms and provide us with a consistent assessment in a unified way. Although these interactions can be improved for fine details, we focus on overall trends.

Further studies on the effective NN interactions, including those of the origin in the three-nucleon forces, are ongoing with various approaches, but more studies are needed to develop and deepen the physics of exotic nuclei up to driplines. The shell evolution is expected to play a major role, as it reflects an average property.

The effects of the shell evolution in actual nuclei have been examined and explored experimentally, as discussed in Sec. VI and elsewhere. The use of a variety of experimental probes, from γ-ray spectroscopy to transfer reactions to electron scattering, is demonstrated in Sec. VI, with a focus on the island of inversion.

The lowering of intruder states containing particle-hole excitations across a magic gap is a dominant phenomenon in the island of inversion or in the shape coexistence in general (Secs. I and II), and it has naturally strong connections to the shell evolution. Various experimental probes clarify different aspects of it.

The interplay of the shell evolution with the continuum physics and weakly bound states, etc., is mentioned in Sec. VI.A.9. This subject is being developed and is of interest both theoretically and experimentally. It will be a subject of forthcoming studies. In those states, substantial changes may appear in the effective interaction, single-particle wave function, etc., and the field continues to devise innovative experimental approaches to investigate them. After all, it is of much interest how the shell evolution changes or persists at the dripline, as well as for loosely bound states.

As the shell evolution will keep unveiling static and dynamic features of exotic nuclei not expected within the conventional view, there will be intriguing, diverse, and glorious frontiers emerging in many ways in nuclear-structure physics. Such frontiers do include heavy nuclei eventually up to the nuclei of superheavy elements, where improvements to predictive power will also contribute. Furthermore, such changes in the understanding and properties of exotic nuclei may also impact other disciplines of science, for instance, astrophysics, astronomy, and nuclear engineering, as neutron-rich exotic nuclei are intermediate products in explosive stellar processes and nuclear reactors.

ACKNOWLEDGMENTS

Useful discussions with Dr. J. P. Schiffer, Dr. B. Kay, Dr. A. Poves, Dr. F. Nowacki, Dr. H. Grawe, Dr. M. Gorska, and Dr. P. Ring are acknowledged. T. O. thanks Dr. Y. Tsunoda and Dr. J. Menendez for the valuable discussions on the monopole interaction, and Dr. T. Miyagi for his great contributions to the overview of *ab initio* approaches. T. O. is also grateful to Dr. M. Honma, Dr. R. Fujimoto, Dr. T. Matsuo, Dr. D. Abe, Dr. K. Tsukiyama, and Professors Y. Akaishi and A. Schwenk for the many relevant productive collaborations. T. O acknowledges Dr. N. Tsunoda for private communications and a related figure in addition to the fruitful collaborations. This work was supported in part by the HPCI Strategic Program "The origin of matter and the Universe" and Priority Issue on Post-K Computer "Elucidation of the fundamental laws and evolution of the Universe" from MEXT and JICFuS (Projects No. hp140210, No. hp150224, No. hp160211, and No. hp170230) and is part of the RIKEN-CNS joint research project on large-scale nuclear-structure calculations. T. O. acknowledges support in part by Grant-in-Aid for Scientific Research No. (A) 20244022 of the JSPS. A. G. acknowledges support from the U.S. National Science Foundation under Grants No. PHY-1102511 and No. PHY-1565546 (NSCL). T. S. acknowledges support in part by the Grant-in-Aid for Scientific Research under Grant No. JP15K05090 of the JSPS. Y. U. acknowledges support in part by the Grant-in-Aid for Scientific Research under Grant No. JP15K05094 of the JSPS.

REFERENCES

Alder, K., A. Bohr, T. Huus, B. Mottelson, and A. Winther, 1956, Rev. Mod. Phys. **28**, 432.

Anguiano, M., G. Co', V. De Donno, and A. M. Lallena, 2011, Phys. Rev. C **83**, 064306.

Anguiano, M., M. Grasso, G. Co', V. De Donno, and A. M. Lallena, 2012, Phys. Rev. C **86**, 054302.

Audi, G., M. Wang, A. Wapstra, F. Kondev, M. MacCormick, X. Xu, and B. Pfeiffer, 2012, Chin. Phys. C **36**, 1287.

Bansal, R. K., and J. B. French, 1964, Phys. Lett. **11**, 145.

Baranger, M., 1970, Nucl. Phys. **A149**, 225.

Barrett, B. R., P. Navrátil, and J. P. Vary, 2013, Prog. Part. Nucl. Phys. **69**, 131.

Bartel, J., K. Bencheikh, and J. Meyer, 2008, Phys. Rev. C **77**, 024311..

Baumann, T., A. Spyrou, and M. Thoennessen, 2012, Rep. Prog. Phys. **75**, 036301.

Bazin, D., *et al.*, 2003, Phys. Rev. Lett. **91**, 012501.

Bender, M., K. Bennaceur, T. Duguet, P. H. Heenen, T. Lesinski, and J. Meyer, 2009, Phys. Rev. C **80**, 064302.

Bender, M., P.-H. Heenen, and P.-G. Reinhard, 2003, Rev. Mod. Phys. **75**, 121.

Bes, D. R., and R. A. Sorensen, 1969, in *Advances in Nuclear Physics*, edited by M. Baranger and E. Vogt (Springer, New York/Berlin), Chap. 3.

Bethe, H. A., 1940a, Phys. Rev. **57**, 260.

Bethe, H. A., 1940b, Phys. Rev. **57**, 390.

Bethe, H. A., and R. F. Bacher, 1936, Rev. Mod. Phys. **8**, 82.

Bildstein, V., R. Gernhäuser, T. Kröll, R. Krücken, K. Wimmer, P. Van Duppen, M. Huyse, N. Patronis, R. Raabe, and T-REX Collaboration, 2012, Eur. Phys. J. A **48**, 85.

Binder, S., J. Langhammer, A. Calci, P. Navrátil, and R. Roth, 2013, Phys. Rev. C **87**, 021303.

Binder, S., J. Langhammer, A. Calci, and R. Roth, 2014, Phys. Lett. B **736**, 119.

Blanchard, C. H., and R. Avery, 1951, Phys. Rev. **81**, 35.

Blaum, K., 2006, Phys. Rep. **425**, 1.

Block, M., *et al.*, 2008, Phys. Rev. Lett. **100**, 132501.

Blumenfeld, Y., T. Nilsson, and P. V. Duppen, 2013, Phys. Scr. **T152**, 014023.

Bogner, S., *et al.*, 2009, arXiv:0903.3366.

Bogner, S. K., R. J. Furnstahl, and R. J. Perry, 2007, Phys. Rev. C **75**, 061001.

Bogner, S. K., H. Hergert, J. D. Holt, A. Schwenk, S. Binder, A. Calci, J. Langhammer, and R. Roth, 2014, Phys. Rev. Lett. **113**, 142501.

Bogner, S. K., T. T. S. Kuo, and A. Schwenk, 2003, Phys. Rep. **386**, 1.

Bohr, A., 1952, Mat. Fys. Medd. K. Dan. Vidensk. Selsk. **26**, 14.

Bohr, A., and B. R. Mottelson, 1953, Mat. Fys. Medd. K. Dan. Vidensk. Selsk. **27**, 16.

Bohr, A., and B. R. Mottelson, 1969, *Nuclear Structure*, Vol. 1 (W. A. Benjamin, Inc., New York).

Bohr, A., and B. R. Mottelson, 1975, *Nuclear Structure*, Vol. 2 (W. A. Benjamin, Inc., New York).

Bouyssy, A., J.-F. Mathiot, N. Van Giai, and S. Marcos, 1987, Phys. Rev. C **36**, 380.

Brink, D. M., and F. Stancu, 2007, Phys. Rev. C **75**, 064311.

Brown, B. A., 1993, Rev. Mex. Fis. **39**, Suppl. 2, 21.

Brown, B. A., 2013, Phys. Rev. Lett. **111**, 162502.

Brown, B. A., T. Duguet, T. Otsuka, D. Abe, and T. Suzuki, 2006, Phys. Rev. C **74**, 061303(R).

Brown, B. A., and A. F. Lisetskiy, 2009 (private communication).

Brown, B. A., and W. A. Richter, 2006, Phys. Rev. C **74**, 034315.

Brown, B. A., W. A. Richter, R. E. Julies, and B. H. Wildenthal, 1988, Ann. Phys. (N.Y.) **182**, 191.

Brown, B. A., and B. Wildenthal, 1988, Annu. Rev. Nucl. Part. Sci. **38**, 29.

Brown, G. E., and T. T. S. Kuo, 1967, Nucl. Phys. **A92**, 481.

Brown, S. M., *et al.*, 2012, Phys. Rev. C **85**, 011302.

Bürger, A., *et al.*, 2005, Phys. Lett. B **622**, 29.

Burgunder, G., *et al.*, 2014, Phys. Rev. Lett. **112**, 042502.

Caesar, C., *et al.* (R3B Collaboration), 2013, Phys. Rev. C **88**, 034313.

Campi, X., H. Flocard, A. Kerman, and S. Koonin, 1975, Nucl. Phys. **A251**, 193.

Carlson, J., S. Gandolfi, F. Pederiva, S. Pieper, R. Schiavilla, S. K. E., and R. Wiringa, 2015, Rev. Mod. Phys. **87**, 1067.

Casten, R. F., and N. V. Zamfir, 1993, Phys. Rev. Lett. **70**, 402.

Catford, W. N., *et al.*, 2010, Phys. Rev. Lett. **104**, 192501.

Caurier, E., G. Martínez-Pinedo, F. Nowacki, A. Poves, and A. P. Zuker, 2005, Rev. Mod. Phys. **77**, 427.

Caurier, E., F. Nowacki, and A. Poves, 2014, Phys. Rev. C **90**, 014302.

Caurier, E., F. Nowacki, A. Poves, and J. Retamosa, 1998, Phys. Rev. C **58**, 2033.

Cipollone, A., C. Barbieri, and P. Navrátil, 2013, Phys. Rev. Lett. **111**, 062501.

Cipollone, A., C. Barbieri, and P. Navrátil, 2015, Phys. Rev. C **92**, 014306.

Clemenger, K., 1985, Phys. Rev. B **32**, 1359.

Cline, D., 1986, Annu. Rev. Nucl. Part. Sci. **36**, 683.

Co', G., V. De Donno, P. Finelli, M. Grasso, M. Anguiano, A. M. Lallena, C. Giusti, A. Meucci, and F. D. Pacati, 2012, Phys. Rev. C **85**, 024322.

Cohen, S., and D. Kurath, 1965, Nucl. Phys. **73**, 1.

Colò, G., H. Sagawa, S. Fracasso, and P. Bortignon, 2007, Phys. Lett. B **646**, 227.

Coraggio, L., A. Covello, A. Gargano, and N. Itaco, 2009, Phys. Rev. C **80**, 044311.

Crawford, H. L., *et al.*, 2010, Phys. Rev. C **82**, 014311.

Crawford, H. L., *et al.*, 2016, Phys. Rev. C **93**, 031303.

Darby, I. G., *et al.*, 2010, Phys. Rev. Lett. **105**, 162502.

Daugas, J., *et al.*, 2010, Phys. Rev. C **81**, 034304.

DeRydt, M., R. Lozeva, N. Vermeulen, F. de Oliveira Santos, S. Grevy, P. Himpe, C. Stodel, J. Thomas, P. Vingerhoets, and G. Neyens, 2009, Nucl. Instrum. Methods Phys. Res., Sect. A **612**, 112.

de-Shalit, A., and M. Goldhaber, 1953, Phys. Rev. **92**, 1211.

de-Shalit, A., and I. Talmi, 1963, *Nuclear Shell Theory* (Academic Press, New York).

Détraz, C., D. Guillemaud, G. Huber, R. Klapisch, M. Langevin, F. Naulin, C. Thibault, L. C. Carraz, and F. Touchard, 1979, Phys. Rev. C **19**, 164.

Dewald, A., O. Möller, and P. Petkov, 2012, Prog. Part. Nucl. Phys. **67**, 786.

Dilling, J., *et al.*, 2006, Int. J. Mass Spectrom. **251**, 198.

Dinca, D. C., *et al.*, 2005, Phys. Rev. C **71**, 041302(R).

Dobaczewski, J., 2006, in *Proceedings of the Third ANL/MSU/JINA/INT RIA Workshop, Lemont, IL, 2006*, edited by T. Duguet, H. Esbensen, K. M. Nollett, and C. D. Roberts (World Scientific, Singapore), p. 152.

Dobaczewski, J., I. Hamamoto, W. Nazarewicz, and J. Sheikh, 1994, Phys. Rev. Lett. **72**, 981.

Doll, P., G. Wagner, K. Knöpfle, and G. Mairle, 1976, Nucl. Phys. **A263**, 210.

Dong, J. M., W. Zuo, J. Z. Gu, Y. Z. Wang, L. G. Cao, and X. Z. Zhang, 2011, Phys. Rev. C **84**, 014303.

Doornenbal, P., *et al.*, 2016, Phys. Rev. C **93**, 044306.

Duflo, J., and A. Zuker, 1995, Phys. Rev. C **52**, R23.

Duflo, J., and A. P. Zuker, 1999, Phys. Rev. C **59**, R2347.

Dufour, M., and A. P. Zuker, 1996, Phys. Rev. C **54**, 1641.

Duguet, T., and G. Hagen, 2012, Phys. Rev. C **85**, 034330.

Duguet, T., H. Hergert, J. Holt, and V. Soma, 2015, Phys. Rev. C **92**, 034313.

Ekström, A., *et al.*, 2015, Phys. Rev. C **91**, 051301.

Elliott, J. P., 1958, Proc. R. Soc. A **245**, 128.

Elliott, J. P., A. D. Jackson, H. A. Mavromatis, E. A. Sanderson, and B. Singh, 1968, Nucl. Phys. **A121**, 241.

Elliott, J. P., and A. M. Lane, 1954, Phys. Rev. **96**, 1160.

ENSDF, 2017, "Evaluated nuclear structure data file," http://www.nndc.bnl.gov/ensdf/.

Entem, D. R., and R. Machleidt, 2003, Phys. Rev. C **68**, 041001.

Epelbaum, E., 2006, Prog. Part. Nucl. Phys. **57**, 654.

Epelbaum, E., H.-W. Hammer, and U.-G. Meißner, 2009, Rev. Mod. Phys. **81**, 1773.

Epelbaum, E., *et al.*, 2002, Phys. Rev. C **66**, 064001.

Erler, J., N. Birge, M. Kortelainen, W. Nazarewicz, E. Olsen, A. M. Perhac, and M. Stoitsov, 2012, Nature (London) **486**, 509.

Fayache, M., L. Zamick, and B. Castel, 1997, Phys. Rep. **290**, 201.

Federman, P., and S. Pittel, 1977, Phys. Lett. **69B**, 385.

Federman, P., and S. Pittel, 1979, Phys. Rev. C **20**, 820.

Federman, P., S. Pittel, and R. Campos, 1979, Phys. Lett. **82B**, 9.

Federman, P., S. Pittel, and A. Etchegoyen, 1984, Phys. Lett. **140B**, 269.

Fernández-Domínguez, B., *et al.*, 2011, Phys. Rev. C **84**, 011301.

Flanagan, K. T., *et al.*, 2009, Phys. Rev. Lett. **103**, 142501.

Fornal, B., *et al.*, 2004, Phys. Rev. C **70**, 064304.

Fornal, B., *et al.*, 2005, Phys. Rev. C **72**, 044315.

Fortune, H. T., 2011, Phys. Rev. C **84**, 024327.

Fortune, H. T., 2012, Phys. Rev. C **85**, 014315.

Franchoo, S., *et al.*, 1998, Phys. Rev. Lett. **81**, 3100.

Franchoo, S., *et al.*, 2001, Phys. Rev. C **64**, 054308.

Franzke, B., H. Geissel, and G. Münzenberg, 2008, Mass Spectrom. Rev. **27**, 428.

French, J. B., 1966, in *Many-body Description of Nuclear Structure and Reactions: Proceedings of the International School of Physics*

"Enrico Fermi," Course 36, edited by C. Bloch (Academic Press, New York), p. 289.

French, J. B., 1969, in *Isospin in Nuclear Physics*, edited by D. H. Wilkinson (North-Holland, Amsterdam), p. 259.

Fujita, J., and H. Miyazawa, 1957, Prog. Theor. Phys. **17**, 360.

Fukunishi, N., T. Otsuka, and T. Sebe, 1992, Phys. Lett. B **296**, 279.

Gade, A., 2015, Eur. Phys. J. A **51**, 118.

Gade, A., and T. Glasmacher, 2008, Prog. Part. Nucl. Phys. **60**, 161.

Gade, A., and S. N. Liddick, 2016, J. Phys. G **43**, 024001.

Gade, A., *et al.*, 2006, Phys. Rev. C **74**, 021302(R).

Gade, A., *et al.*, 2008, Phys. Rev. C **77**, 044306.

Gaudefroy, L., *et al.*, 2006, Phys. Rev. Lett. **97**, 092501.

Glasmacher, T., 1998, Annu. Rev. Nucl. Part. Sci. **48**, 1.

Goodman, A. L., 1977, Nucl. Phys. **A287**, 1.

Grawe, H., 2004, "Shell model from a practitioner's point of view," in *The Euroschool Lectures on Physics with Exotic Beams, Vol. I*, edited by J. Al-Khalili and E. Roeckl (Springer, Berlin/Heidelberg), pp. 33–75.

Grawe, H., *et al.*, 2005, Eur. Phys. J. A **25**, 357.

Grigorenko, L. V., I. G. Mukha, and M. V. Zhukov, 2013, Phys. Rev. Lett. **111**, 042501.

Guillemaud-Mueller, D., C. Detraz, M. Langevin, F. Naulin, M. de Saint-Simon, C. Thibault, F. Touchard, and M. Epherre, 1984, Nucl. Phys. **A426**, 37.

Hagen, G., M. Hjorth-Jensen, G. R. Jansen, R. Machleidt, and T. Papenbrock, 2012a, Phys. Rev. Lett. **108**, 242501.

Hagen, G., M. Hjorth-Jensen, G. R. Jansen, R. Machleidt, and T. Papenbrock, 2012b, Phys. Rev. Lett. **109**, 032502.

Hagen, G., G. R. Jansen, and T. Papenbrock, 2016, Phys. Rev. Lett. **117**, 172501.

Hagen, G., T. Papenbrock, D. J. Dean, and M. Hjorth-Jensen, 2008, Phys. Rev. Lett. **101**, 092502.

Hagen, G., T. Papenbrock, D. J. Dean, and M. Hjorth-Jensen, 2010, Phys. Rev. C **82**, 034330.

Hagen, G., T. Papenbrock, D. J. Dean, M. Hjorth-Jensen, and B. V. Asokan, 2009, Phys. Rev. C **80**, 021306.

Hagen, G., *et al.*, 2016, Nat. Phys. **12**, 186.

Hammer, H.-W., A. Nogga, and A. Schwenk, 2013, Rev. Mod. Phys. **85**, 197.

Hansen, P. G., and B. Jonson, 1987, Europhys. Lett. **4**, 409.

Hansen, P. G., and J. A. Tostevin, 2003, Annu. Rev. Nucl. Part. Sci. **53**, 219.

Haxel, O., J. H. D. Jensen, and H. E. Suess, 1949, Phys. Rev. **75**, 1766.

Hebeler, K., S. K. Bogner, R. J. Furnstahl, A. Nogga, and A. Schwenk, 2011, Phys. Rev. C **83**, 031301.

Hergert, H., S. Binder, A. Calci, J. Langhammer, and R. Roth, 2013, Phys. Rev. Lett. **110**, 242501.

Hergert, H., S. Bogner, S. Binder, A. Calci, J. Langhammer, R. Roth, and A. Schwenk, 2013, Phys. Rev. C **87**, 034307.

Hergert, H., S. Bogner, T. D. Morris, A. Schwenk, and K. Tsukiyama, 2016, Phys. Rep. **621**, 165.

Hergert, H., S. K. Bogner, T. D. Morris, S. Binder, A. Calci, J. Langhammer, and R. Roth, 2014, Phys. Rev. C **90**, 041302.

Heyde, K., P. Van Isacker, R. F. Casten, and J. L. Wood, 1985, Phys. Lett. **155B**, 303.

Heyde, K., and J. Wood, 1991, J. Phys. G **17**, 135.

Heyde, K., and J. L. Wood, 2011, Rev. Mod. Phys. **83**, 1467.

Heylen, H., *et al.*, 2016, Phys. Rev. C **94**, 034312.

Hinohara, N., K. Sato, K. Yoshida, T. Nakatsukasa, M. Matsuo, and K. Matsuyanagi, 2011, Phys. Rev. C **84**, 061302.

Hjorth-Jensen, M., T. T. S. Kuo, and E. Osnes, 1995, Phys. Rep. **261**, 125.

Hoffman, C. R., *et al.*, 2008, Phys. Rev. Lett. **100**, 152502.

Holt, J. D., T. Otsuka, A. Schwenk, and T. Suzuki, 2012, J. Phys. G **39**, 085111.

Honma, M., T. Otsuka, and T. Mizusaki, 2008, RIKEN Accel. Prog. Rep. **41**, 32.

Honma, M., T. Otsuka, B. A. Brown, and T. Mizusaki, 2005, Eur. Phys. J. A **25**, 499.

Horiuchi, W., and Y. Suzuki, 2006, Phys. Rev. C **74**, 034311.

Huber, G., *et al.*, 1978, Phys. Rev. C **18**, 2342.

Huck, A., G. Klotz, A. Knipper, C. Miehé, C. Richard-Serre, G. Walter, A. Poves, H. L. Ravn, and G. Marguier, 1985, Phys. Rev. C **31**, 2226.

Janssens, R. V. F., 2005, Nature (London) **435**, 897.

Janssens, R. V. F., *et al.*, 2002, Phys. Lett. B **546**, 55.

Ji, X., and B. Wildenthal, 1989, Phys. Rev. C **40**, 389.

Kaneko, K., Y. Sun, M. Mizusaki, and T. Hasegawa, 2011, Phys. Rev. C **83**, 014320.

Kanungo, R., *et al.*, 2009, Phys. Rev. Lett. **102**, 152501.

Kanungo, R., *et al.*, 2010, Phys. Lett. B **682**, 391.

Kanungo, R., *et al.*, 2016, Phys. Rev. Lett. **117**, 102501.

Kay, B. P., C. R. Hoffman, and A. O. Macchiavelli, 2017, Phys. Rev. Lett. **119**, 182502.

Kay, B. P., S. Freeman, J. Schiffer, J. Clark, C. Deibel, A. Heinz, A. Parikh, and C. Wrede, 2008, Phys. Lett. B **658**, 216.

Kay, B. P., *et al.*, 2011, Phys. Rev. C **84**, 024325.

Khan, S., T. Kihm, K. Knopfle, G. Mairle, V. Bechtold, and L. Freidrich, 1985, Phys. Lett. **156B**, 155.

Kimura, M., 2007, Phys. Rev. C **75**, 041302.

Kirson, M. W., 1973, Phys. Lett. B **47**, 110.

Klingenbeck, K., W. Knüpfer, M. G. Huber, and P. W. M. Glaudemans, 1977, Phys. Rev. C **15**, 1483.

Knight, W. D., K. Clemenger, W. A. de Heer, W. A. Saunders, M. Y. Chou, and M. L. Cohen, 1984, Phys. Rev. Lett. **52**, 2141.

Kobayashi, N., *et al.*, 2012, Phys. Rev. C **86**, 054604.

Kobayashi, N., *et al.*, 2014, Phys. Rev. Lett. **112**, 242501.

Kobayashi, T., *et al.*, 2013, Nucl. Instrum. Methods Phys. Res., Sect. B **317**, 294.

Kohley, Z., *et al.*, 2013, Phys. Rev. Lett. **110**, 152501.

Kondo, Y., *et al.*, 2016, Phys. Rev. Lett. **116**, 102503.

Köster, U., *et al.*, 2011, Phys. Rev. C **84**, 034320.

Koura, H., 2005, Prog. Theor. Phys. **113**, 305.

Kramer, G., H. Blok, J. V. Hienen, S. Brandenburg, M. Harakeh, S. V. D. Werf, P. Glaudemans, and A. Wolters, 1988, Nucl. Phys. **A477**, 55.

Kramer, G., H. Blok, and L. Lapikás, 2001, Nucl. Phys. **A679**, 267.

Kucuk, Y., and J. Tostevin, 2014, Phys. Rev. C **89**, 034607.

Kuo, T. T. S., 1967, Nucl. Phys. **A103**, 71.

Kuo, T. T. S., and G. E. Brown, 1966, Nucl. Phys. **85**, 40.

Kwiatkowski, A. A., *et al.*, 2015, Phys. Rev. C **92**, 061301.

Lalazissis, G. A., S. Karatzikos, M. Serra, T. Otsuka, and P. Ring, 2009, Phys. Rev. C **80**, 041301(R).

Lalazissis, G. A., T. Nikšić, D. Vretenar, and P. Ring, 2005, Phys. Rev. C **71**, 024312.

Leidemann, W., and G. Orlandini, 2013, Prog. Part. Nucl. Phys. **68**, 158.

Lesinski, T., M. Bender, K. Bennaceur, T. Duguet, and J. Meyer, 2007, Phys. Rev. C **76**, 014312.

Liang, H., N. Van Giai, and J. Meng, 2008, Phys. Rev. Lett. **101**, 122502.

Liddick, S. N., *et al.*, 2004, Phys. Rev. Lett. **92**, 072502.

Lisetskiy, A., B. Barrett, M. Kruse, P. Navrátil, I. Stetcu, and J. Vary, 2008, Phys. Rev. C **78**, 044302.

Lisetskiy, A., B. A. Brown, M. Horoi, and H. Grawe, 2004, Phys. Rev. C **70**, 044314.

Lisetskiy, A., B. A. Brown, and M. Horoi, 2005, Eur. Phys. J. A **25**, 95.
Litvinova, E., 2016, Phys. Lett. B **755**, 138.
Litvinova, E., and P. Ring, 2006, Phys. Rev. C **73**, 044328.
Long, W., H. Sagawa, N. V. Giai, and J. Meng, 2007, Phys. Rev. C **76**, 034314.
Long, W.-H., N. V. Giai, and J. Meng, 2006, Phys. Lett. B **640**, 150.
Lunderberg, E., *et al.*, 2012, Phys. Rev. Lett. **108**, 142503.
Macchiavelli, A. O., *et al.*, 2016, Phys. Rev. C **94**, 051303.
Macfarlane, M. H., and J. B. French, 1960, Rev. Mod. Phys. **32**, 567.
Machleidt, R., and D. R. Entem, 2011, Phys. Rep. **503**, 1.
Mairle, G., 1993, Phys. Lett. B **304**, 39.
Mayer, M. G., 1949, Phys. Rev. **75**, 1969.
Millener, D., and D. Kurath, 1975, Nucl. Phys. **A255**, 315.
Moreno-Torres, M., M. Grasso, H. Liang, V. De Donno, M. Anguiano, and N. Van Giai, 2010, Phys. Rev. C **81**, 064327.
Morfouace, P., *et al.*, 2015, Phys. Lett. B **751**, 306.
Motobayashi, T., *et al.*, 1995, Phys. Lett. B **346**, 9.
Mutschler, A., *et al.*, 2016a, Nat. Phys. (to be published).
Mutschler, A., *et al.*, 2016b, Phys. Rev. C **93**, 034333.
Myers, E. G., 2013, Int. J. Mass Spectrom. **349-350**, 107.
Nakada, H., 2008, Phys. Rev. C **78**, 054301.
Nakamura, T., H. Sakurai, and H. Watanabe, 2017, Prog. Part. Nucl. Phys. **97**, 53.
Nakamura, T., *et al.*, 1999, Phys. Rev. Lett. **83**, 1112.
Nakamura, T., *et al.*, 2009, Phys. Rev. Lett. **103**, 262501.
Nakamura, T., *et al.*, 2014, Phys. Rev. Lett. **112**, 142501.
Navrátil, P., J. P. Vary, and B. R. Barrett, 2000a, Phys. Rev. C **62**, 054311.
Navrátil, P., J. P. Vary, and B. R. Barrett, 2000b, Phys. Rev. Lett. **84**, 5728.
Navrátil, P., V. G. Gueorguiev, J. P. Vary, W. E. Ormand, and A. Nogga, 2007, Phys. Rev. Lett. **99**, 042501.
Neyens, G., 2011, Phys. Rev. C **84**, 064310.
Neyens, G., *et al.*, 2005, Phys. Rev. Lett. **94**, 022501.
Nilsson, S. G., 1955, Dan. Mat. Fys. Medd. **29**, 16.
Nowacki, F., and A. Poves, 2009, Phys. Rev. C **79**, 014310.
Ogawa, M., R. Broda, K. Zell, P. J. Daly, and P. Kleinheinz, 1978, Phys. Rev. Lett. **41**, 289.
Olivier, L., *et al.*, 2017, Phys. Rev. Lett. **119**, 192501.
Osnes, E., and D. Strottman, 1992, Phys. Rev. C **45**, 662.
Osterfeld, F., 1992, Rev. Mod. Phys. **64**, 491.
Otsuka, T., 2002, Prog. Theor. Phys. Suppl. **146**, 6.
Otsuka, T., 2013, Phys. Scr. **T152**, 014007.
Otsuka, T., 2014, Genshikaku Kenkyu **59**, 86.
Otsuka, T., R. Fujimoto, Y. Utsuno, B. A. Brown, M. Honma, and T. Mizusaki, 2001, Phys. Rev. Lett. **87**, 082502.
Otsuka, T., T. Matsuo, and D. Abe, 2006, Phys. Rev. Lett. **97**, 162501.
Otsuka, T., and A. Schwenk, 2012, Nucl. Phys. News Int. **22**, No. 4, 12.
Otsuka, T., and T. Suzuki, 2013, Few-Body Syst. **54**, 891.
Otsuka, T., T. Suzuki, R. Fujimoto, H. Grawe, and Y. Akaishi, 2005, Phys. Rev. Lett. **95**, 232502.
Otsuka, T., T. Suzuki, J. D. Holt, A. Schwenk, and Y. Akaishi, 2010, Phys. Rev. Lett. **105**, 032501.
Otsuka, T., T. Suzuki, M. Honma, Y. Utsuno, N. Tsunoda, K. Tsukiyama, and M. Hjorth-Jensen, 2010, Phys. Rev. Lett. **104**, 012501.
Otsuka, T., and Y. Tsunoda, 2016, J. Phys. G **43**, 024009.
Ozawa, A., T. Kobayashi, T. Suzuki, K. Yoshida, and I. Tanihata, 2000, Phys. Rev. Lett. **84**, 5493.
Paschalis, S., *et al.*, 2013, Nucl. Instrum. Methods Phys. Res., Sect. A **709**, 44.
Perrot, X., *et al.*, 2006, Phys. Rev. C **74**, 014313.
Péru, S., M. Girod, and J. F. Berger, 2000, Eur. Phys. J. A **9**, 35.
Péru, S., and M. Martini, 2014, Eur. Phys. J. A **50**, 88.
Pieper, S. C., 2005, Nucl. Phys. **A751**, 516.
Pieper, S. C., and R. B. Wiringa, 2001, Annu. Rev. Nucl. Part. Sci. **51**, 53.
Pittel, S., P. Federman, G. E. Arenas Peris, R. F. Casten, and W. T. Chou, 1993, Phys. Rev. C **48**, 1050.
Poves, A., and J. Retamosa, 1987, Phys. Lett. B **184**, 311.
Poves, A., and A. Zuker, 1981, Phys. Rep. **70**, 235.
Prisciandaro, J. I., *et al.*, 2001, Phys. Lett. B **510**, 17.
Pritychenko, B., M. Birch, B. Singh, and M. Horoi, 2016, At. Data Nucl. Data Tables **107**, 1.
Pudliner, B. S., V. R. Pandharipande, J. Carlson, S. C. Pieper, and R. B. Wiringa, 1997, Phys. Rev. C **56**, 1720.
Ragnarsson, I., and S. Nilsson, 1995, *Shapes and Shells in Nuclear Structure* (Cambridge University Press, Cambridge, England).
Rainwater, J., 1950, Phys. Rev. **79**, 432.
Reed, M. W., *et al.*, 2010, Phys. Rev. Lett. **105**, 172501.
Reinhard, P.-G., D. J. Dean, W. Nazarewicz, J. Dobaczewski, J. A. Maruhn, and M. R. Strayer, 1999, Phys. Rev. C **60**, 014316.
Rejmund, M., S. Bhattacharyya, A. Navin, W. Mittig, L. Gaudefroy, M. Gelin, G. Mukherjee, F. Rejmund, P. Roussel-Chomaz, and Ch. Theisen, 2007, Phys. Rev. C **76**, 021304(R).
Ren, Z., Z. Zhu, Y. Cai, and G. Xu, 1996, Phys. Lett. B **380**, 241.
Ring, P., and P. Schuck, 1980, *The Nuclear Many-Body Problem* (Springer-Verlag, Berlin).
Rodríguez, T. R., and J. L. Egido, 2007, Phys. Rev. Lett. **99**, 062501.
Rodríguez-Guzmán, R. R., J. L. Egido, and L. M. Robledo, 2000, Phys. Rev. C **62**, 054319.
Rotaru, F., *et al.*, 2012, Phys. Rev. Lett. **109**, 092503.
Roth, R., S. Binder, K. Vobig, A. Calci, J. Langhammer, and P. Navrátil, 2012, Phys. Rev. Lett. **109**, 052501.
Rubio, B., and W. Gelletly, 2009, in *The Euroschool Lectures on Physics with Exotic Beams, Vol. III*, Lecture Notes in Physics Vol. 764, edited by J. Al-Khalili and E. Roeckl (Springer, Berlin/Heidelberg), pp. 99–151.
Ruiz, Garcia, R. F., *et al.*, 2016, Nat. Phys. **12**, 594.
Rutherford, H., 1911, Philos. Mag. **21**, 669.
Sagawa, H., and G. Colò, 2014, Prog. Part. Nucl. Phys. **76**, 76.
Sahin, E., *et al.*, 2017, Phys. Rev. Lett. **118**, 242502.
Sakurai, H., *et al.*, 1999, Phys. Lett. B **448**, 180.
Santamaria, C., *et al.*, 2015, Phys. Rev. Lett. **115**, 192501.
Schiffer, J. P., and W. W. True, 1976, Rev. Mod. Phys. **48**, 191.
Schiffer, J. P., *et al.*, 2004, Phys. Rev. Lett. **92**, 162501.
Schiffer, J. P., *et al.*, 2013, Phys. Rev. C **87**, 034306.
Schwerdtfeger, W., *et al.*, 2009, Phys. Rev. Lett. **103**, 012501.
Seweryniak, D., *et al.*, 2007, Phys. Rev. Lett. **99**, 022504.
Shi, Y., 2017, Phys. Rev. C **95**, 034307.
Shimada, K., *et al.*, 2012, Phys. Lett. B **714**, 246.
Shimizu, K., M. Ichimura, and A. Arima, 1974, Nucl. Phys. **A226**, 282.
Sieja, K., F. Nowacki, K. Langanke, and G. Martínez-Pinedo, 2009, Phys. Rev. C **79**, 064310.
Simonis, J., K. Hebeler, J. D. Holt, J. Menéndez, and A. Schwenk, 2016, Phys. Rev. C **93**, 011302.
Simonis, J., S. R. Stroberg, K. Hebeler, J. D. Holt, and A. Schwenk, 2017, Phys. Rev. C **96**, 014303.
Simpson, E. C., and J. A. Tostevin, 2010, Phys. Rev. C **82**, 044616.
Simpson, E. C., J. A. Tostevin, D. Bazin, B. A. Brown, and A. Gade, 2009, Phys. Rev. Lett. **102**, 132502.
Sinatkas, J., L. Skouras, D. Strottman, and J. Vergados, 1992, J. Phys. G **18**, 1377.

Skyrme, T., 1958, Nucl. Phys. **9**, 615.

Smirnova, N. A., B. Bally, K. Heyde, F. Nowacki, and K. Sieja, 2010, Phys. Lett. B **686**, 109.

Smirnova, N. A., A. De Maesschalck, A. Van Dyck, and K. Heyde, 2004, Phys. Rev. C **69**, 044306.

Smirnova, N. A., K. Heyde, B. Bally, F. Nowacki, and K. Sieja, 2012, Phys. Rev. C **86**, 034314.

Soma, V., A. Cippolone, C. Barbieri, P. Navrátil, and T. Duguet, 2014, Phys. Rev. C **89**, 061301.

Soma, V., T. Duguet, and C. Barbieri, 2011, Phys. Rev. C **84**, 064317.

Sorlin, O., 2014, EPJ Web Conf. **66**, 01016.

Sorlin, O., and M.-G. Porquet, 2008, Prog. Part. Nucl. Phys. **61**, 602.

Sorlin, O., and M.-G. Porquet, 2013, Phys. Scr. **T152**, 014003.

Stancu, F., D. M. Brink, and H. Flocard, 1977, Phys. Lett. **68B**, 108.

Stanoiu, M., *et al.*, 2004, Phys. Rev. C **69**, 034312.

Stanoiu, M., *et al.*, 2008, Phys. Rev. C **78**, 034315.

Stefanescu, X., *et al.*, 2008, Phys. Rev. Lett. **100**, 112502.

Steppenbeck, D., *et al.*, 2013, Nature (London) **502**, 207.

Steppenbeck, D., *et al.*, 2015, Phys. Rev. Lett. **114**, 252501.

Steppenbeck, D., *et al.*, 2017, Phys. Rev. C **96**, 064310.

Stevenson, P., J. R. Stone, and M. Strayer, 2002, Phys. Lett. B **545**, 291.

Stoitsov, M. V., J. Dobaczewski, P. Ring, and S. Pittel, 2000, Phys. Rev. C **61**, 034311.

Storm, M., A. Watt, and R. Whitehead, 1983, J. Phys. G **9**, L165.

Stroberg, S., A. Calci, H. Hergert, J. Holt, S. Bogner, R. Roth, and A. Schwenk, 2017, Phys. Rev. Lett. **118**, 032502.

Stroberg, S., H. Hergert, J. Holt, S. Bogner, and A. Schwenk, 2016, Phys. Rev. C **93**, 051301.

Sugano, S., 1991, *Microcluster Physics*, Springer Series in Materials Science Vol. 20, edited by J. Toennies (Springer-Verlag, Berlin/Heidelberg).

Suzuki, T., and T. Otsuka, 2008, Phys. Rev. C **78**, 061301.

Suzuki, T., T. Otsuka, C. Yuan, and N. Alahari, 2016, Phys. Lett. B **753**, 199.

Takayanagi, K., 2011a, Nucl. Phys. **A852**, 61.

Takayanagi, K., 2011b, Nucl. Phys. **A864**, 91.

Talmi, I., and I. Unna, 1960, Phys. Rev. Lett. **4**, 469.

Tanaka, K., *et al.*, 2010, Phys. Rev. Lett. **104**, 062701.

Tanihata, I., H. Hamagaki, O. Hashimoto, Y. Shida, N. Yoshikawa, K. Sugimoto, O. Yamakawa, T. Kobayashi, and N. Takahashi, 1985, Phys. Rev. Lett. **55**, 2676.

Tarasov, O., *et al.*, 1997, Phys. Lett. B **409**, 64.

Tarpanov, D., H. Liang, N. V. Giai, and C. Stoyanov, 2008, Phys. Rev. C **77**, 054316.

Terasaki, J., H. Flocard, P.-H. Heenen, and P. Bonche, 1997, Nucl. Phys. **A621**, 706.

Terry, J. R., *et al.*, 2006, Phys. Lett. B **640**, 86.

Terry, J. R., *et al.*, 2008, Phys. Rev. C **77**, 014316.

Thibault, C., R. Klapisch, C. Rigaud, A. M. Poskanzer, R. Prieels, L. Lessard, and W. Reisdorf, 1975, Phys. Rev. C **12**, 644.

Tichal, A., J. Langhammer, S. Binder, and R. Roth, 2014, Phys. Lett. B **736**, 119.

Togano, Y., *et al.*, 2016, Phys. Lett. B **761**, 412.

Tostevin, J. A., 1999, J. Phys. G **25**, 735.

Tostevin, J. A., and A. Gade, 2014, Phys. Rev. C **90**, 057602.

Tostevin, J. A., G. Podolyák, B. A. Brown, and P. G. Hansen, 2004, Phys. Rev. C **70**, 064602.

Towner, I. S., 1987, Phys. Rep. **155**, 263.

Tripathi, V., *et al.*, 2005, Phys. Rev. Lett. **94**, 162501.

Tsukiyama, K., S. K. Bogner, and A. Schwenk, 2011, Phys. Rev. Lett. **106**, 222502.

Tsukiyama, K., S. K. Bogner, and A. Schwenk, 2012, Phys. Rev. C **85**, 061304.

Tsukiyama, K., T. Otsuka, and R. Fujimoto, 2015, Prog. Theor. Exp. Phys. **2015**, 093D01.

Tsunoda, N., 2018 (private communication).

Tsunoda, N., T. Otsuka, N. Shimizu, M. Hjorth-Jensen, K. Takayanagi, and T. Suzuki, 2017, Phys. Rev. C **95**, 021304.

Tsunoda, N., T. Otsuka, K. Tsukiyama, and M. Hjorth-Jensen, 2011, Phys. Rev. C **84**, 044322.

Tsunoda, N., K. Takayanagi, M. Hjorth-Jensen, and T. Otsuka, 2014, Phys. Rev. C **89**, 024309.

Tsunoda, Y., T. Otsuka, N. Shimizu, M. Honma, and Y. Utsuno, 2014, Phys. Rev. C **89**, 031301(R).

Umeya, A., and K. Muto, 2004, Phys. Rev. C **69**, 024306.

Umeya, A., and K. Muto, 2006, Phys. Rev. C **74**, 034330.

Utsuno, Y., T. Otsuka, B. A. Brown, M. Honma, T. Mizusaki, and N. Shimizu, 2012a, Phys. Rev. C **86**, 051301.

Utsuno, Y., T. Otsuka, B. A. Brown, M. Honma, T. Mizusaki, and N. Shimizu, 2012b, Prog. Theor. Phys. Suppl. **196**, 304.

Utsuno, Y., T. Otsuka, T. Mizusaki, and M. Honma, 1999, Phys. Rev. C **60**, 054315.

Utsuno, Y., T. Otsuka, T. Mizusaki, and M. Honma, 2004, Phys. Rev. C **70**, 044307.

van Kolck, U., 1994, Phys. Rev. C **49**, 2932.

Vautherin, D., and D. Brink, 1970, Phys. Lett. **32B**, 149.

Volya, A., and V. Zelevinsky, 2005, Phys. Rev. Lett. **94**, 052501.

von Weizsäcker, C. F., 1935, Z. Phys. **96**, 431.

Wang, L. J., J. M. Dong, and W. H. Long, 2013, Phys. Rev. C **87**, 047301.

Warburton, E. K., J. A. Becker, and B. A. Brown, 1990, Phys. Rev. C **41**, 1147.

Warburton, E. K., and B. A. Brown, 1992, Phys. Rev. C **46**, 923.

Wienholtz, F., *et al.*, 2013, Nature (London) **498**, 346.

Wilkinson, D. H., and D. E. Alburger, 1959, Phys. Rev. **113**, 563.

Wimmer, K., *et al.*, 2010, Phys. Rev. Lett. **105**, 252501.

Wood, J. L., and K. Heyde, 2016, J. Phys. G **43**, 020402.

Wood, J. L., K. Heyde, W. Nazarewicz, M. Huyse, and P. Van Duppen, 1992, Phys. Rep. **215**, 101.

Wood, J. L., E. Zganjar, C. D. Coster, and K. Heyde, 1999, Nucl. Phys. **A651**, 323.

Yamashita, M., R. S. Marques de Carvalho, T. Frederico, and L. Tomio, 2011, Phys. Lett. B **697**, 90.

Yao, J. M., H. Mei, H. Chen, J. Meng, P. Ring, and D. Vretenar, 2011, Phys. Rev. C **83**, 014308.

Yazaki, K., 1977, Nucl. Phys. **A277**, 189.

Yoneda, K., *et al.*, 2006, Phys. Rev. C **74**, 021303.

Yoro, K., 1980, Nucl. Phys. **A333**, 67.

Yoshida, S., 2017, master's thesis (University of Tokyo).

Yuan, C., T. Suzuki, T. Otsuka, F. Xu, and N. Tsunoda, 2012, Phys. Rev. C **85**, 064324.

Yukawa, H., 1935, Proc. Phys. Math. Soc. Jpn. **17**, 48.

Zalewski, M., J. Dobaczewski, W. Satuła, and T. R. Werner, 2008, Phys. Rev. C **77**, 024316.

Zalewski, M., P. Olbratowski, M. Rafalski, W. Satuła, T. R. Werner, and R. A. Wyss, 2009, Phys. Rev. C **80**, 064307.

Zalewski, M., W. Satuła, J. Dobaczewski, P. Olbratowski, M. Rafalski, T. R. Werner, and R. A. Wyss, 2009, Eur. Phys. J. A **42**, 577.

Zamick, L., 1965, Phys. Lett. **19**, 580.

Zeldes, N., T. S. Dumitrescu, and H. S. Köhler, 1983, Nucl. Phys. **A399**, 11.

Zou, W., G. Colò, Z. Ma, H. Sagawa, and P. F. Bortignon, 2008, Phys. Rev. C **77**, 014314.

Zuker, A. P., 1994, Nucl. Phys. **A576**, 65.

Zuker, A. P., 2003, Phys. Rev. Lett. **90**, 042502.

Zuker, A. P., 2005, in *Key Topics in Nuclear Structure: Proceedings of the 8th International Spring Seminar on Nuclear Physics*, edited by A. Covello (World Scientific, Singapore), p. 135.

Zuker, A. P., A. Poves, F. Nowacki, and S. M. Lenzi, 2015, Phys. Rev. C **92**, 024320.

See Supplemental Material at http://link.aps.org/supplemental/10.1103/RevModPhys.92.015002, which includes (S1)–(S3) additional explanations and mathematical derivations on the general monopole properties discussed in Sec. III, (S4) another example for Sec. III.G, (S5) additional explanations on the two-body LS force discussed in Sec. IV.F, (S6) an additional example to Sec. VI.A.8 with $1i_{13/2}$-$1h_{9/2}$ splitting, and (S7) an additional example to Sec. VI.D with the $1i_{13/2}$-$1h_{9/2}$ coupling in heavy nuclei.